TOPOLOGICAL ASPECTS OF CHARGE TRANSPORT IN QUANTUM MANY-BODY SYSTEMS

A DISSERTATION SUBMITTED TO

THE GRADUATE SCHOOL OF ENGINEERING AND SCIENCE

OF BILKENT UNIVERSITY

IN PARTIAL FULFILLMENT OF THE REQUIREMENTS FOR

THE DEGREE OF

DOCTOR OF PHILOSOPHY

IN

PHYSICS

By

Mohammad Yahyavi

January 2019

Topological Aspects of Charge Transport in Quantum Many-Body Systems
By Mohammad Yahyavi
January 2019

We certify that we have read this dissertation and that in our opinion it is fully adequate, in scope and in quality, as a dissertation for the degree of Doctor of Philosophy.

Balázs Hetényi(Advisor)

Mehmet Özgür Oktel

Bekir Sıtkı Kandemir

Bilal Tanatar

Ali Ulvi Yılmazer

Approved for the Graduate School of Engineering and Science:

Ezhan Karaşan
Director of the Graduate School

ABSTRACT

TOPOLOGICAL ASPECTS OF CHARGE TRANSPORT IN QUANTUM MANY-BODY SYSTEMS

Mohammad Yahyavi
Ph.D. in Physics
Advisor: Balázs Hetényi
January 2019

Motivated by the recent proposals and developments of topological insulators and topological superconductors for their potential applications in electronic devices and quantum computing, we have theoretically studied topological properties of quantum many-body systems. First, we calculate the gauge-invariant cumulants (and moments) associated with the Zak phase. The first cumulant corresponds to the Berry phase itself, the others turn out to be the associated spread, skew, kurtosis, etc. The cumulants are shown to be gauge invariant. We reconstruct the underlying probability distribution of the polarization by maximizing the information entropy and applying the moments as constraints in the Rice-Mele model and in the interacting, spinless Su-Schrieffer-Heeger model. When the Wannier functions are localized within one-unit cell, the probability distribution so obtained corresponds to that of the Wannier function. We follow the probability distribution of the polarization in cycles around the topologically nontrivial point of these models. Secondly, we have constructed a topological one-dimensional analog of the Haldane and Kane-Mele models in two dimensions, with hexagonal lattices. Our Haldane one-dimensional analog model belongs to the C and CI symmetry classes, depending on the parameters, but, due to reflection, it exhibits topological insulation. The model consists of two superimposed Creutz models with onsite potentials. The topological invariants of each Creutz model sum to give the mirror winding number, with winding numbers which are nonzero individually but equal and opposite in the topological phase, and both zero in the trivial phase. We also construct a topological one-dimensional ladder model following the steps which lead to the Kane-Mele model in two dimensions. We couple two Haldane-type ladder models, one for each spin channel, in such a way that time-reversal invariance is restored. We also add a Rashba spin-orbit coupling term. The model falls in the CII symmetry class. We demonstrate the presence of edge states and quantized Hall response in the topological region.

Our model exhibits two distinct topological regions, distinguished by the different types of reflection symmetries. Thirdly, we consider the edge at the interface of a simple tight-binding model and a band insulator. We find that crossings in the band structure (one dimensional Dirac points) appear when an interface is present in the system. We calculate the hopping energy resolved along lines of bonds parallel to the interface as a function of distance from the interface. Similarly, we introduce a transport coefficient (Drude weight) for charge currents running parallel to the interface. We find that charge mobility (both the kinetic energy and the Drude weight) is significantly enhanced in the surface of the tight-binding part of the model near the interface.

Finally, we study a variant of the generalized Aubry-André-Harper model with the effect of introducing next nearest-neighbor p-wave superconducting pairing with incommensurate and commensurate cosine modulations. We extend generalized Aubry-André-Harper model with p-wave superconducting to topologically equivalent and nontrivial an "ancestor" two-dimensional p-wave superconducting model. It is found that in incommensurate (commensurate) modulation, by varying next nearest-neighbor p-wave pairing order parameter, the system can switch between extended states and localized states (fully gapped phase and a gapless phase).

Keywords: Geometric Phases, Gauge-Invariant Cumulants, Polarization Distribution, Topological Matter, One Dimensional Systems, Quantum Phase Transitions.

ÖZET

KUANTUM ÇOK PARÇACIKLI SİSTEMLERİNDEKİ YÜK TAŞINIMININ TOPOLOJİK YÖNLERİ

Mohammad Yahyavi
Fizik, Doktora
Tez Danışmanı: Balázs Hetényi
Ocak 2019

Topolojik yalıtkanlar ve topolojik süperiletkenler üzerine elektronik cihazlar ve kuantum programlama alanlarındaki uygulamaları için yapılan önerme ve gelişmelerden ilhamla kuantum çok parçacıklı sistemlerin topolojik özelliklerini teorik olarak çalıştık. İlk olarak, Zak fazı ile bağlantılı ölçümden bağımsız kümülantları (ve momentleri) hesapladık. İlk kümülant Berry fazının kendisine karşılık gelmektedir, diğerleri yayılma, eğiklik ve basıklık vb. ile alakalıdır. Kümülantların ölçümden bağımsız olduğu gösterilmiştir. Temelindeki polarizasyon olasılık dağılımını bilgi entropisini maksimize ederek ve momentlerini Rice-Mele modeli ile etkileşimli, spinsiz Su-Schrieffer-Heeger modeline kısıtlama olarak koyarak yeniden düzenledik. Wannier fonksiyonları birim hücrede lokalize hale getirildiğinde, elde edilen olasılık dağılımı Wannier fonksiyonuna karşılık gelmektedir. Bu modeller için, önemli bir topolojik nokta etrafında çember çizen polarizasyonun olasılık dağılımına baktık. İkinci olarak, altıgen örgülerdeki iki boyutlu Haldane ve Kane-Mele modellerinin bir boyutlu topolojik analojisini oluşturduk. Haldane bir boyutlu analoji modelimiz parameterelere bağlı olarak C ve CI simetri sınıflarına aittir, fakat yansımaya göre topolojik yalıktan gibi davranmaktadır. Model iki süperimpoze Cruetz modelinin potansiyellerine dayanmaktadır. Creutz modelin topolojik değişmezler toplandığında sarmal sayısını verir, sarmal sayıları sıfır olmayan fakat eşit ya da zıt olan sayılardır ya da ikisi de ihmal edilebilir durumda sıfırdır. Ayrıca, geliştirdiğimiz iki boyultu Kane-Mele modeline ulaşan bir boyutlu topolojik merdiven modeli için aşağıdaki stepler uygulanmıştır. Her biri bir spin kanalı için olmak üzere, iki Haldane tipi merdiven modelini zaman dönüşümlü değişmezi eski haline dönecek şekilde eşledik. Rashba spin-yörünge eşleşme terimini de ekledik. Bu model CII simetri sınıfına denk gelmektedir. Topolojik bölgede kuantize Hall tepkisinin ve kenar durumlarının varlığını gösterdik. Modelimiz değişik tipteki yansıma simetrilerinin yardımıyla

ayrılan iki farklı topolojik bölge göstermektedir. Üçüncü olarak basit bir sıkı-bağlayıcı model ve bant yalıtkanın arayüzeyindeki kenarı dikkate aldık. Sistemde bir arayüzey mevcutken bant yapısında (bir boyutlu Dirac noktaları için) geçit mevcut olduğunu bulduk. Atlama enerjisinin arayüzeyden uzaklığa bağlı bir fonksiyon olarak, arayüzeye paralel bağların hatları boyunca olduğunu hesapladık. Benzer bir şekilde, arayüzeye paralel akan yük akımları için bir taşıma katsayısı (Drude ağırlığı) tanımladık.Yük hareketliliğinin (hem kinetik enerji hem de Drude ağırlığı için) sıkı-bağlayıcı kısmın yüzeyinin arayüzeye yakın olduğu kısımlarda oldukça gelişmiş olduğunu bulduk.

Son olarak, Aubry-Andre-Harper modelinin bir varyantını, oransız ve oranlı kosinüs modülasyonlarıyla eşleşen bir sonraki yakın komşu p-dalgası süperiletkeni etkisini tanımlayarak genelledik. Genel p-dalgası süperilekten Aubry-Andre-Harper modelini topolojik eşdeğeri ve önemli bir ata iki boyutlu p-dalga süperiletken modele genişlettik. Sistemin geniş durumları ve lokalize durumları (tam açık faz ve aralıksız faz) arasında, oransız (oranlı) modülasyon ile, bir sonraki yakın-komşu p-dalga eşleşme düzenlilik parametresinin değiştirilmesiyle geçiş yapabileceği bulunmuştur.

Anahtar sözcükler: Geometrik Fazlar, Ölçüm-Değişmez Kümülantlar, Polarizasyon Dağılımı, Topolojik Madde, Tek Boyutlu Sistemler, Kuantum Faz Geçişleri.

Acknowledgement

I would like to express my gratitude to my supervisor Prof. Balázs Hetényi for his continuous support of my Ph.D study and related research, for his friendship, patience, motivation, and immense knowledge. His guidance helped me in all the time of research and writing of this thesis.

Besides my advisor, I would like to thank the rest of my thesis committee: Prof. Mehmet Özgür Oktel, and Prof. Ahmet Levent Subaşi, for their insightful comments and encouragement, but also for the hard question which incented me to widen my research from various perspectives. I want to also thank Prof. Bilal Tanatar, Prof. Bekir Sıtkı Kandemir and Prof. Ali Ulvi Yilmazer for their time, reading and reviewing this thesis. My deep gratitude also to Prof. Ceyhun Bulutay for all the advice and guidance. Also, I thank my team members and friends, Sina Gholizadeh and Luqman Saleem.

I would like to thank my family: my parents and my wife parents for supporting me spiritually throughout writing this thesis and my life in general.

Last but not the least, I would especially like to thank my wife **Elmira**. She has been extremely supportive of me throughout this entire process and has made countless sacrifices to help me get to this point. My daughter **Elisa**, has continually provided the requisite breaks from philosophy and the motivation to finish my degree with expediency.

Mohammad Yahyavi.

Abbreviations

QHE ..... Quantum Hall Effect

QSH ..... Quantum Spin Hall

2D ..... Two Dimentional

TKNN ..... Thouless, Kohmoto, Nightingale, and den Nijs

SSH ..... Su-Schrieffer-Heeger

KMH ..... Kane-Mele-Hubbard

RM ..... Rice-Mele

BWF ..... Baeriswyl wavefunction

GIC ..... Gauge Invariant Cumulant

GIM ..... Gauge Invariant Moment

GAA ..... Generalized Aubry-André

NN ..... Nearest Neighbor

CDW ..... Charge Density Wave

BZ ..... Brillouin Zone

HM ..... Haldane Model

PHS ..... Particle Hole Symmetry

TRS ..... Time Reversal Symmetry

CS ..... Chiral Symmetry

SC ..... Superconductivity

BdG ..... Bogoliubov-de Gennes

MIPR ..... Mean Inverse Participation Ratio

FSS ..... Finite Size Scaling

TB ..... Tight-Binding

CI ..... Crystalline Insulator

Contents

1 Introduction **1**

2 Polarization and gauge invariant cumulants **11**

2.1 Gauge invariant cumulants associated with the Zak phase 12

2.1.1 Cumulants connection vs. gauge-invariant quantity. 15

2.1.2 Cumulants connection vs. perturbation theory 16

2.2 Polarization, current and their spreads 16

2.3 Measurement of C_ns 19

2.4 Connection to the distribution of Wannier centers 19

2.5 Relation to response functions 20

2.6 Examples 21

2.6.1 A spin-$\frac{1}{2}$ particle in a precessing magnetic field 21

2.6.2 Generalized Aubry–André model 23

2.6.3 Results and analysis 29

3 Reconstruction of the probability distribution **32**

3.1 Reconstruction of the probability distribution by maximizing information entropy 35

3.2 Su-Schrieffer-Heeger and Rice-Mele models 36

3.2.1 Fully dimerized limit 41

3.2.2 Results and analysis 43

3.3 Interacting Su-Schrieffer-Heeger model 51

3.3.1 The Baeriswyl variational wave function 52

3.3.2 Parent Hamiltonian of the Baeriswyl wave function 58

3.3.3 Polarization and gauge invariant cumulants 59

3.3.4 Results and analysis 59

4 Topological physics in one-dimensional systems 64

4.1 A one-dimensional analog of the Haldane model 64

4.1.1 Winding number of Haldane-like model 69

4.1.2 Hall response of the Haldane-like model 73

4.2 A one-dimensional analog of the Kane-Mele model 76

4.2.1 Symmetry analysis and topological indices 78

4.2.2 Středa-Widom formula for quantum spin Hall systems . . . 82

4.2.3 Results of Kane-Mele-like model 84

5 Enhanced charge transport at the ideal-conductor/insulator interface 85

5.1 The Drude weight as a topological invariant 87

5.2 Model: The ideal-conductor/insulator interface 89

5.3 Results 90

6 Topological phase transition in a generalized Aubry-André-Harper system with p-wave superconductivity 95

6.1 Generalized Aubry-André-Harper model 96

6.2 The corresponding 2D of GAAH model with p-wave SC 100

6.3 Incommensurate modulation case 101

6.3.1 Off-diagonal GAAH model with p-wave pairing 105

6.3.2 Generic GAAH model with p-wave pairing 109

6.4 Commensurate modulation 110

6.4.1 Chern numbers 111

7 Conclusion 114

A Numerical minimization of χ^2 131

B Publications in SCI journals 134

List of Figures

1.1 This is the integer quantum Hall effect. R_H is the Hall resistance and R_{xx} is the longitudinal resistance. 2

1.2 (a) 1D ring Aubry-André model with modulated potential where the filled black circles represent the atomic sites, (b) This is the 2D model of the diagonal Aubry-André model which the hopping is to nearest neighbors. 3

1.3 Phase diagram of the Haldane model as a function of ϕ and M/t_2. 4

2.1 Discrete representation of a closed curve in parameter space. . . . 13

2.2 Cumulants of a spin$-\frac{1}{2}$ particle in a precessing field. 22

2.3 Schematic representation of the pure commensurate modulations of GAA model (blue box denotes the unit cell). c_A and c_B represents the different sublattices, and V refer to the on-site potential. J and J' are the alternating hoppings. 25

2.4 Moments and cumulants of GAA model for $\delta = 0.5$, $\phi_V = 0$, and $V = 0$ as a function of ϕ_δ. 26

2.5 Moments and cumulants of GAA model for $\delta = 0.5$, $\phi_V = 0$, and $V = 0.5$ as a function of ϕ_δ. 27

2.6 Moments and cumulants of GAA model for $\delta = 0.5$, $\phi_V = 0$, and $V = 1$ as a function of ϕ_δ. 28

2.7 Polarization as a function of ϕ_δ and ϕ_V in the pure commensurate modulations of GAA Hamiltonian.At $\phi_\delta = 0$ and $\phi_V = 0$, if the radius of closed path encloses it is larger than $\pi/2$, there are foure singularities (from the first cumulant in a 3D plot we can appreciate the singularities) and the change in polarization is equal to $e/2$ (dash line circle of right inset). Also, if the radius of close path is smaller than $\pi/2$, the change in polarization is equal to zero (solid line circle of right inset). 30

3.1 Schematic representation of the Rice-Mele model. Δ represents the on-site potential, A and B refer to the different sublattices. J and J' are the alternating hoppings. The unit cell is indicated in yellow. The x label corresponds to localization within the unit cell ($-1 < x < 1$). The variable x is continuous, below, in our subsequent calculations, the probability distribution will be shown as a function of x. The unit of x is the lattice constant. 38

3.2 Moments for $J'/J = 0$ (upper panel) and 0.3 (lower panel) as a function of Δ/J. In these calculations $J = 1$. For $J'/J = 0$ the curves are identical. The insets show the corresponding cumulants. 39

3.3 Moments for $J'/J = 0.5$ (upper panel) and 0.7 (lower panel) as a function of Δ/J. In these calculations $J = 1$. The insets show the corresponding cumulants. 40

3.4 Moments for $J'/J = 1$ as a function of Δ/J. In these calculations $J = 1$. The inset shows the corresponding cumulants. In the limit $\Delta/J \to 0$ (the topological point of the model) the even cumulants diverge, while the odd cumulants are always zero for this case. . 42

3.5 First two moments and cumulants (right inset) for $J = 1, J' = J \pm 0.006$. Left inset shows the first moment on the $\Delta - \delta$ plane, indicating the singular behavior along the line $\Delta < 0, \delta = 0$. . . . 43

3.6 Normalized probability distribution of the polarization for different parameters of the Rice-Mele Hamiltonian. In these calculations $J = 1$. The unit of length in these figures is the lattice constant. Different values of Δ/J are shown for $J'/J = 0.0$. In the topmost panel ($J'/J = 0$) the inset shows the distribution for the cases $\Delta/J = 0.0, -0.1, -0.2, -0.3, -0.4, -0.5$) 44

3.7 Normalized probability distribution of the polarization for different parameters of the Rice-Mele Hamiltonian. In these calculations $J = 1$. The unit of length in these figures is the lattice constant. Different values of Δ/J are shown for $J'/J = 0.3$. In the topmost panel ($J'/J = 0$) the inset shows the distribution for the cases $\Delta/J = 0.0, -0.1, -0.2, -0.3, -0.4, -0.5$) 45

3.8 Normalized probability distribution of the polarization for different parameters of the Rice-Mele Hamiltonian. In these calculations $J = 1$. The unit of length in these figures is the lattice constant. Different values of Δ/J are shown for $J'/J = 0.5$. In the topmost panel ($J'/J = 0$) the inset shows the distribution for the cases $\Delta/J = 0.0, -0.1, -0.2, -0.3, -0.4, -0.5$) 46

3.9 Normalized probability distribution of the polarization for different parameters of the Rice-Mele Hamiltonian. In these calculations $J = 1$. The unit of length in these figures is the lattice constant. Different values of Δ/J are shown for $J'/J = 0.7$. In the topmost panel ($J'/J = 0$) the inset shows the distribution for the cases $\Delta/J = 0.0, -0.1, -0.2, -0.3, -0.4, -0.5$) 47

3.10 Normalized probability distribution of the polarization for cases $J' = J$ and $J' = J \pm \epsilon$ ($\epsilon = 0.006$). In these calculations $J = 1$. The unit of length is the lattice constant. Different values of Δ/J are shown. Upper panel(lower panel): $\Delta/J < 0$ ($\Delta/J > 0$). 48

3.11 Moments, cumulants, and probability distribution along a circle of radius 1 in the Δ/t vs. δ/t plane. In these calculations $t = 1$. The path encircles the topological point $\Delta/t = 0, \delta/t = 0$. The top panels shows the gauge invariant moments and cumulants along the circle as a function of angle. The lower panel follows the evolution of the probability distribution. The point A^* is at an angle $\phi = -\pi/2 + 2\pi/1000$, not $\phi = -\pi/2$. In the lower panel the unit of x is the lattice constant. The points $\phi = -\pi/2, 3\pi/2$ are excluded from the curves shown in the upper panels. 49

3.12 Moments, cumulants, and probability distribution along a circle of radius 0.2 in the Δ/t vs. δ/t plane. In these calculations $t = 1$. The path encircles the topological point $\Delta/t = 0, \delta/t = 0$. The upper panel shows the gauge invariant moments and cumulants along the circle as a function of angle. The top panels shows the gauge invariant moments and cumulants along the circle as a function of angle. The lower panel follows the evolution of the probability distribution. The point A^* is at an angle $\phi = -\pi/2 + 2\pi/1000$, not $\phi = -\pi/2$. In the lower panel the unit of x is the lattice constant. The points $\phi = -\pi/2, 3\pi/2$ are excluded from the curves shown in the upper panels. 50

3.13 Graphical representation of our model Hamiltonian (part a)) and the charge density wave (CDW) state (part b)). Filled(Empty) circles indicate lattice sites occupied(not occupied) by particles. In part a) V indicates the interaction, t indicates the average hopping, δ denotes the amount by which the hopping alternates between even and odd bonds. 52

3.14 Upper panel: The variational ground state energy per particle for (a) $\delta = 0$, and (b) $\delta = 0.7$ based on the Baeriswyl wave function compared to exact diagonalization for 12 lattice sites . Lower panel: the variational parameter as a function of interaction strength for $\delta = 0, \pm 0.3$ and ± 0.7. Solid lines indicate the global minimum in the CDW type insulating phase. Dashed lines indicate metastable insulating phases on the metallic side of the phase diagram. 53

3.15 Phase diagram. I and II are SSH states (Hartree-Fock approximation). III is a CDW type phase, with finite skew when δ differs from zero. The dashed line indicates a Fermi sea (ideal conductor). 54

3.16 Curves traced out by the Hamiltonian in the Brillouin zone. Left panel shows the correlated system, $\delta = \cos(\phi), V = 1 + 4\sin(\phi)$. On the right panel $\delta = \cos(\phi), V = 1$. For both panels, the values of the variable ϕ are indicated in the legend on the right. 56

3.17 (a) First cumulant, (C_1) or polarization, of the interacing Su-Schrieffer-Heeger model as a function of δ and V. (b) Lines in the $\delta - V$ plane for which we calculate the cumulants and reconstruct the polarization. Two paths are shown between the points $-1, 1$ and $1, 1$: path $\mathcal{A}$ is a straight line, path $\mathcal{B}$ is a semi-ellipse. (c) Moments and cumulants along the semi-elliptic $(\mathcal{B})$ path. (d) Moments and cumulants along the straight line $(\mathcal{A})$ path. 57

3.18 Reconstructed polarization distributions along the two paths shown indicated in Fig. 3.17. The upper panel(lower panel) shows reconstructed polarizations along the ellipse(straight line) between the points $-1, 1$ to $1, 1$ on the $\delta - V$ plane. 60

3.19 Reconstructed polarization for the Rice-Mele model along the paths indicated in the inset of each plot. The paths are represented on the $\delta - \Delta$ plane. 61

4.1 Ladder model. The hopping parameters are defined as follows: t_x denotes hopping along the legs of the ladder, t_y denote the hoppings perpendicular to legs, t_{xy} denotes hoppings occurring diagonally between legs, connecting second nearest neighbors. The sites in red(blue) indicate where the site depedendent potential is positive(negative). A Peierls phase of Φ is introduced along the diagonal hoppings. These can be thought of as arising from magnetic impurities residing halfway through the perpendicular (t_y) hoppings and arranged antiferromagnetically. 65

4.2 Band structure within the reduced Brillouin zone (RBZ). The red dashed lines indicate the band structure for a system with $t_x = 1, t_y = 1, t_{xy} = 0, \Delta = 0.5$. At half-filling this system is gapped. For $t_y = 0$ the gaps would be at the edge of the RBZ ($k = \pm\frac{\pi}{2}$). Finite t_y causes the gaps to move towards the origin (the gap is at $k^{\pm} = \pm\text{acos}(\frac{t_y}{2t_x})$). The blue solid lines indicate gap closure when t_{xy} is made finite ($t_{xy}\sin(k^{\pm})\sin(\Phi) = \Delta$, ($\Phi = \frac{\pi}{2}$)). The inset shows the phase diagram (where gap closure occurs) for $t_x = 1, t_y = 1$. The lines separate two insulating phases. The red(black) lines indicates gap closure occurring at $k^{+}(k^{-})$. 67

4.3 Lower panel: band structure of a system of size 100 sites with open boundary conditions. In this calculation $t_x = 1$, $t_y = 1$, and $t_{xy} = 0.3$. Inside the lobes (see inset of Fig. 4.2) edge states arise. Upper two panel: squared modulus of the wavefunction for the two edge states averaged over the two legs of the ladder, for $\Phi = \pi/2$ for a system of 200 sites. 71

4.4 Examples of phase diagrams in three dimensions. The upper(lower) panel shows the phase diagram Δ, Φ, Φ_B for $t_x = t_y = t_{xy} = 1$ ($t_x = t_y = 1, t_{xy} = 0.75$). The phase diagram was determined by searching for the gap closure. 72

4.5 Band structure of system with finite $\Gamma = 0.5$ and edge states (upper four panels). The other parameters are $t_x = t_y = t_{xy} = 1$, $\Phi = \pi/2$, and $\Phi_B = 0$. The variable Δ is scanned. Localized edge states are found at quarter, half, and three-quarter fillings. 75

4.6 Graphic representation of our model. $t_x(t_y)$ denotes hoppings along horizontal(vertical) bonds. t_{xy} denotes diagonal bonds. We apply Peierls phases along the diagonal bonds along the directions indicated. 77
4.7 Phase diagram of the system where gap closure occurs. The numbers in the figures denote the topological winding number. 79
4.8 Energy spectrum of the shifted Creutz model with 200 sites, open boundary conditions as a function of t_{xy}. The parameters are $t_x = 1$ and $t_y = 1$. The blue lines indicate states which are not present when periodic boundary conditions are applied. The square magnitude of these states are shown in the upper panels. They are localized near the edges of the chain. 81
4.9 Main figure: phase diagram for systems with $t_x = 1, t_{xy} = 0.06, 0.12, 0.18$ in the t_y vs. λ_R plane. The inset indicates the k vector at which gap closure occurs as a function of t_y/t_{xy}. The black filled circles and red filled diamonds on the left side of the phase diagram indicate systems for which we have tested our Středa-Widom formula. For the black filled circles we found a quantized quantum spin Hall response, while we found no response for the red diamonds. 83

5.1 Schematic view of the lattice model studied in this thesis. The upper half is a simple tight-binding model (ideal conductor) the lower half is a band-insulator. The dashed line indicates an interface. . 86
5.2 Band structure of the model with $U = 1$ as a function of k_x. The lattice is bipartite in the x-direction, the Brillouin zone in this direction is halved (restricted Brillouin zone). The left side is the raw data, the center plot is the data in the restricted Brillouin zone, the right shows the band structure zoomed to near the Fermi level at half-filling. 87
5.3 Density of states for crystalline insulator, tight-binding, and model with an interface between the two ($U = 1$). The crystalline insulator is gapped, the system with interface is not gapped, but the density is smaller near $E = 0$ than in the tight-binding system. . 89

5.4 Kinetic energy resolved to bonds parallel to the interface for different values of U. The variable y indicates the y-coordinate of the bonds according to Figure 5.1. Clearly, the kinetic energy is peaked (in the negative direction) at the interface.The inset shows the value of the kinetic energy for bonds running along the interface for different values of U. The size of the systems studies is 50×200. 91

5.5 The Drude weight (resolved to bonds along the y direction) as a function of y coordinate for different values of the strength of the external potential U. The Drude weight is peaked at the interface. The left inset shows the resolved Drude weight for a tight-binding model with periodic and open boundary conditions. The right inset shows the value of the Drude weight for the interface. The Drude weight is peaked at the interface. The value at the peak increases as a function of U. The size of the systems is 48×200. . 92

5.6 Spread in the total momentum resolved as a function of y coordinate for different values of the strength of the external potential. The spread in the total momentum is minimized at the interface. The size of the systems studied was 50×200. 93

6.1 Graphical presentations of extended 1d GAAH with nearest and next-nearest hopping (SC pairing) and on-site potential to a 2D Hamiltonian. In the presence of a perpendicular magnetic field with β flux quantum per unit cell, the electrons hop on a rectangular lattice. (a) This is the 2D "ancestor" of the diagonal GAAH model which the hopping is to nearest neighbors, (b) This is the 2D "ancestor" of the off-diagonal GAAH model which the hopping is to next-nearest neighbors, and (c) This is the 2D "ancestor" of the SC pairing of GAAH model which the hopping is to nearest and next nearest neighbors. Each rectangular plaquettes which demonstrated by different color are pierced by β flux quantum. . 97

6.2 Phase diagram of the off-diagonal GAAH model with the p-wave incommensurate modulation amplitude δ and the p-wave pairing strength Δ. The hopping incommensurate modulation amplitude is set to $\tau = 0$ and the phase in the incommensurate modulation is set to $k_y = \pi/2$ and $\varphi = \beta\pi$. The phases are (I and II) extended phases, (III) the mobility-edge phase, and (IV) critical phase. . . 98

6.3 The energy spectrum of the off-diagonal GAAH model with p-wave pairing plotted as a function of δ under OBCs in the lattice dimension with 100 lattice sites. The model parameters are fixed at $\tau = 0$, $V = 0$, and $\Delta = 0.5$. Inside the regions I and II (see figure 6.2) edge states arise. 99

6.4 MIPR as a function of p-wave superfluid pairing Δ for the indicated values of modulation amplitude δ. The dashed lines, dot-dashed lines, and solid lines demonstrate the abrupt changes of the MIPR at phase boundaries. 102

6.5 Phase diagram of the off-diagonal GAAH model with the p-wave incommensurate modulation amplitude $0 < \delta \leq 2$ and the p-wave pairing strength $0 \leq \Delta \leq 4$. The hopping incommensurate modulation amplitude is set to $\tau = 1$ and the phase in the incommensurate modulation is set to $k_y = \pi/2$ and $\varphi = \beta\pi$. The phases are (I) localized phase($|\delta - \tau|$), (II) critical localized phase, and (III) extended phases. 103

6.6 Uupper panel: MIPR (log-scale) as a function of p-wave superfluid pairing Δ/t for different chain lengths L for $\tau = 1$ and $\delta/t = 0.5$. Bottom panel: MIPR with the inverse system size $1/L$. For the extended phase, MIPR tends to zero as L increases. 106

6.7 Phase diagram of the generic GAAH model with the p-wave incommensurate modulation amplitude $0 < \delta \leq 2$ and the p-wave pairing strength $0 \leq \Delta \leq 4$. The hopping incommensurate modulation amplitude is set to $\tau = 1$, the on-site potential incommensurate modulation amplitude is set to $V/t = 1$, and the phase in the incommensurate modulation is set to $k_y = \pi/2$ and $\varphi = \beta\pi$. The phases are (I) localized phase, (II) critical localized phase, (III) critical extended phases, (IV) extended phases. 107

6.8 Hofstadter butterfly: energy spectrum as a function of magnetic flux per plaquette β in Aubry-André lattice with $V = 0$, $\tau = 0.3$, $\Delta = 0.4$, and (a) $\delta = 1$, (b) $\delta = 0.2$, (c) $\delta = 0.4$, (d) $\delta = 0.6$, (e) $\delta = 0.8$, (f) $\delta = 1$. 108

6.9 The evolution of the energy bands for $\beta = 0.25$, $V = 0$, $\tau = 0.3$, and $\Delta = 0.4$ as function of δ shown in Fig. (6.8). Gaps are labeled with their Chern numbers. 109

6.10 Hofstadter butterfly: energy spectrum as a function of magnetic flux per plaquette β in Aubry-André lattice with $V = 1$, $\tau = 0.3$, $\Delta = 0.4$, and (a) $\delta = 1$, (b) $\delta = 0.2$, (c) $\delta = 0.4$, (d) $\delta = 0.6$, (e) $\delta = 0.8$, (f) $\delta = 1$. 110

6.11 The evolution of the energy bands for $\beta = 0.25$, $V = 1$, $\tau = 0.3$, and $\Delta = 0.4$ as function of δ shown in Fig. (6.10). Gaps are labeled with their Chern numbers. 111

List of Tables

A.1 $-\log_{10}\chi^2$ rounded to the first digit shown for the reconstructed probabilities in Figs. 3.6 and 3.10. 132

A.2 Values of the parameters according to the parametrization used in Figs. 3.2-3.10 are shown. Also shown are values of $-\log_{10}\chi^2$ rounded to the first digit for probability distributions corresponding to the points in Figs. 3.11 and 3.12. 133

Chapter 1

Introduction

Quantum many-body systems with unusual transport properties arising from the topology of the band structure are of great current interest. Recent developments, such as optical lattices, topological insulators [1], topological superconductors and Majorana quasi-particle bound states [2, 3, 4], allow for the investigation of a number of challenging questions. The first well-studied example of a topological quantum system was the quantum Hall effect [5, 6, 7, 8] (QHE). In a two dimensional (2D) electronic system, when a magnetic field is applied perpendicular to the plane of the system, the transverse and longitudinal resistance exhibits sharp peaks and plateaus (see Fig. 1.1), respectively, indicating integer or fractional quantization of resistance. In an influential paper, Thouless *et al.* [8] showed that the Hall conductance corresponds to a topological invariant: an integral over the curvature of the band structure. The Hall conductivity of the system is given by

$$\sigma_{xy} = \frac{e^2}{\hbar} C \tag{1.1}$$

where

$$C = \frac{i}{2\pi} \sum_{E_m(\mathbf{k}) < E_F} \int_{\mathbf{k} \in BZ} d^2\mathbf{k} \left[\langle \partial_x u_{m\mathbf{k}} | \partial_y u_{m\mathbf{k}} \rangle - \langle \partial_y u_{m\mathbf{k}} | \partial_x u_{m\mathbf{k}} \rangle \right] \tag{1.2}$$

is the Thouless, Kohmoto, Nightingale, and den Nijs (TKNN) integer, also called the Chern number. Here, the integration is over the entire Brillouin and $|u_{m\mathbf{k}}\rangle$ is the Bloch state.

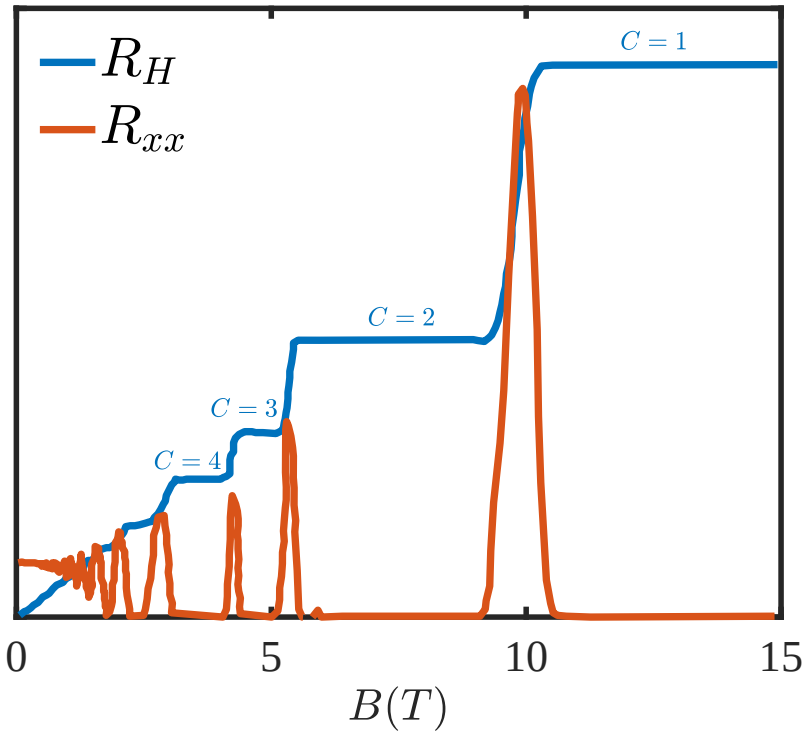

Figure 1.1: This is the integer quantum Hall effect. R_H is the Hall resistance and R_{xx} is the longitudinal resistance.

A tight binding model with quasi-periodic potential that has been explored from the viewpoint of topological states of matter, is the Aubry-André model [9, 10, 11, 12], also known as the Harper [13] model. In the one dimensional (1D) Aubry-André model, periodic phase parameters can be introduced as artificial dimensions giving an opportunity to investigate topological phenomena in higher dimensions, which is described by the following Hamiltonian

$$\hat{\mathcal{H}} = -\sum_{j=1}^{N} \left[t c_{j+1}^{\dagger} c_j + \text{H.c.}) \right] + \sum_{j}^{N} V_j \hat{n}_j \tag{1.3}$$

where

$$V_j = V \cos(2\pi\beta j + k_y). \tag{1.4}$$

are commensurate (incommensurate) potential modulations with periodicity $1/\beta$ and phase factor k_y. $\hat{n}_j = c_j^{\dagger} c_j$ are number operators, $c_j^{\dagger}(c_j)$ is the creation (annihilation operators) at position j on the lattice, t is the hopping (or tunneling)

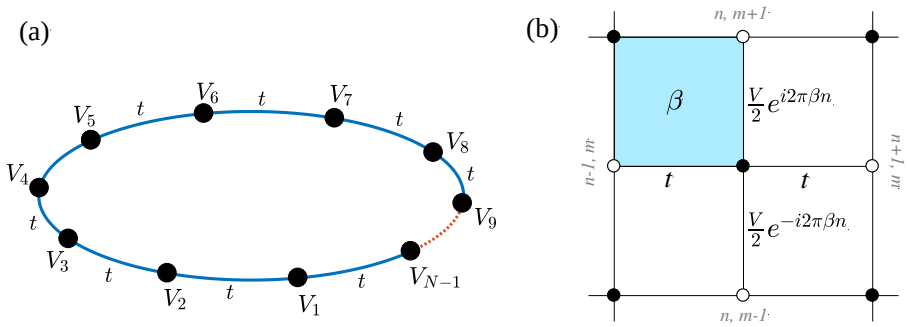

Figure 1.2: (a) 1D ring Aubry-André model with modulated potential where the filled black circles represent the atomic sites, (b) This is the 2D model of the diagonal Aubry-André model which the hopping is to nearest neighbors.

amplitudes to the nearest neighbors, and V is the on-site potential strength. This model can be mapped exactly to the 2D Harper-Hofstadter model [10, 14, 15] which is a model for describing lattice systems in the presence of a gauge field. For any given k_y, the Aubry-André model of Eq. (1.3) can be viewed as the k_yth Fourier component of general 2D Hamiltonian. On the other hand, k_y is the second degree of freedom, hence, we define the operator c_{n,k_y} that satisfies the following commutation relation

$$\{c_{n,k_y}, c^{\dagger}_{\acute{n},\acute{k_y}}\} = \delta_{n,\acute{n}}\delta_{k_y,\acute{k_y}} \tag{1.5}$$

Therefore the 2D Hamiltonian can be expressed in terms of $\hat{H}$ as

$$\hat{\mathcal{H}} = \frac{1}{2\pi}\int_0^{2\pi} \hat{H}(k_y)\, dk_y \tag{1.6}$$

where in Hamiltonian of Eq. (1.3), we replaced the operators c_n with c_{n,k_y}. The corresponding Hamiltonian can be written as

$$\hat{H}(k_y) = -\sum_n \left[t c^{\dagger}_{n,k_y} c_{n+1,k_y} + \text{H.c.}\right] + \sum_n V_n c^{\dagger}_{n,k_y} c_{n,k_y} \tag{1.7}$$

Define the Fourier transform such that

$$c_{n,k_y} = \sum_m e^{-ik_y m} c_{n,m} \tag{1.8}$$

allows us to easily calculate 2D Hamiltonian as

$$\hat{\mathcal{H}} = \sum_{n,m} - \left[t c^{\dagger}_{n,m} c_{n+1,m} + \text{H.c.} \right] + \sum_{n,m} \frac{V}{2} \left[e^{i(2\pi\beta n)} c^{\dagger}_{n,m} c_{n,m+1} + \text{H.c.} \right] \tag{1.9}$$

This link between the 2D Harper-Hofstadter and 1D Aubry-André models implies that the Aubry-André model must have topologically protected modes similar to a 2D quantum Hall system on a lattice (Hosftadter model). Recent experiments in ultracold atoms [11] realized this topological edge state. Additionally, by considering two periodic phase parameters, this model can be induced from a 3D system [16]. Recently [17], the connection between the generalized Aubry-André model with p-wave superconducting pairing, the Su-Schrieffer-Heeger-like (SSH-like) [18] topological phase, and a Kitaev-like [19, 20] topological phase which supports Majorana fermions at edges were investigated. When the superconductor is in the topological phase, Majorana bound states exist at the ends of the wires [21, 22]. Majorana fermions are unusual in that they are their own antiparticle. In Majorana devices [23, 24], one will need to manipulate these properties in real time, and so understanding how they respond is a pressing problem to solve.

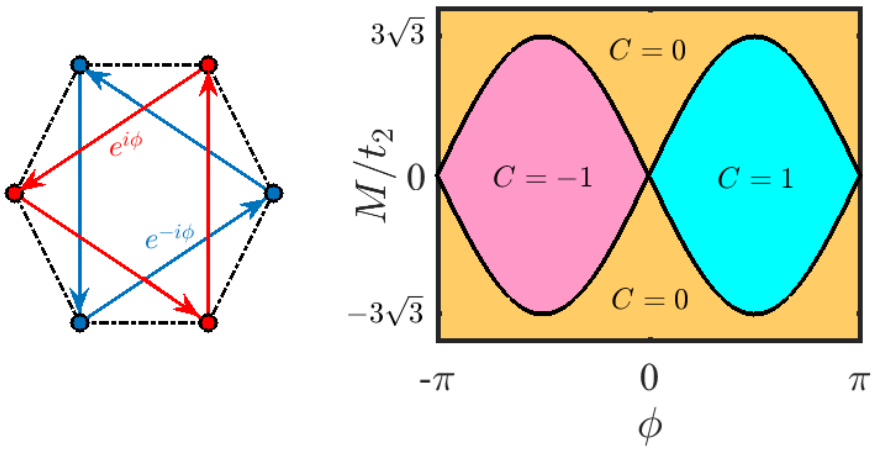

Figure 1.3: Phase diagram of the Haldane model as a function of ϕ and M/t_2.

In 1988, Haldane suggested a model which also exhibited a quantized Hall conductance, but in the absence of a magnetic field [25] which is described by the

following Hamiltonian

$$\hat{\mathcal{H}} = t_1 \sum_{<i,j>} c_i^\dagger c_j + t_2 \sum_{<<i,j>>} e^{-i\nu_{ij}\phi} c_i^\dagger c_j + \sum_i \xi_i c_i^\dagger c_i \tag{1.10}$$

The first term introduces the nearest-neighbor hopping with amplitude t_1, and the second term describes the next-nearest neighbor hopping which applied for breaking time-reversal symmetry. Here, $\nu_{ij} = -\nu_{ji} = \pm 1$ which constitute alternating next-nearest neighbor hopping with a vanishing total flux through each hexagon. A generalization of this model led to the theoretical prediction [26, 27, 28, 29] and experimental discovery [30] of the quantum spin Hall effect. The band structures of the models which exhibit this effect (for example the Kane-Mele model [27, 28]) can be characterized by topological invariants, and the effect arises when these invariants take non-trivial values. One of the trademark characteristics of quantum Hall and quantum spin Hall systems is edge-currents. Edge currents can be expected [31] to arise at interfaces between systems with different values for a particular topological invariant. A simple and intuitive argument for edge currents is that the surfaces over which the topological invariants are evaluated (often the band structure of a two-dimensional system) are connected in a different way on the two sides of the interface. The shapes on each side of the interface cannot be continuously deformed into each other, and the fact that they need to be "cut" at the interface manifests in current carrying edge states. The topological properties of both 2D and 3D interacting models is revealed by calculating corresponding topological invariants. Topological models in one dimension [32, 33] have also actively been studied. A starting point is usually the Berry phase, defined in the 1D lattice dimension.

$$\phi = -\mathrm{Im} \ln \prod_{I=0}^{M-1} \langle \Psi_0(\boldsymbol{\xi}_I) | \Psi_0(\boldsymbol{\xi}_{I+1}) \rangle, \tag{1.11}$$

where $|\Psi_0(\boldsymbol{\xi})\rangle$ is an eigenstate of the Hamiltonian and $\Psi_0(\boldsymbol{\xi}_M) = \Psi_0(\boldsymbol{\xi}_0)$ (cyclic) which is physically well-defined since arbitrary phases cancel. The Berry phase which arises from integrating across the Brillouin zone [34] (the Zak phase) corresponds to the polarization [35, 36, 37] of a crystalline system,

$$\phi = i \oint \mathrm{d}\boldsymbol{\xi} \cdot \langle \Psi_0(\boldsymbol{\xi}) | \nabla_{\boldsymbol{\xi}} | \Psi_0(\boldsymbol{\xi}) \rangle, \tag{1.12}$$

while modified versions of it give topological indices such as the Chern number [8] or time-reversal polarization [38]. In this thesis, we have studied higher order gauge-invariant cumulants in the Rice-Mele (RM) and spinless SSH models to investigate the reconstructed polarization distribution and have studied how they evolve as functions of different parameters of the Hamiltonian [39, 40, 41]. In particular, we calculated the evolution of the polarization distribution around the topologically nontrivial point of the model. It was shown [42] that the third cumulant, also known as the skew, corresponds to the so called shift current, the second-order nonlinear optical response in second harmonic generation experiments (this work addresses such experiments in a Weyl semimetal). It was emphasized that the skew gives a more intuitive picture of the system than the sum rules valid for nonlinear response. Kobayashi *et al.* [43] studied the following quantity in the metallic phase,

$$Z^{(q)} = \langle \Psi | (\exp{(i2\pi \hat{X}/L)})^q | \Psi \rangle \tag{1.13}$$

L denotes the system size, $\hat{X}$ is the total position operator, and q is a real number an integer in systems with periodic boundary conditions. The $q = 1$ case was suggested by Resta and Sorella [37, 44] for the polarization and its variance. A modification to this scheme was suggested by Aligia and Ortiz [45] for lattice systems with fractional fillings. It can be shown that for general q this quantity contains the same information as gauge invariant cumulants. Recent efforts [46] have focused on understanding the effects of electron interactions on such systems. Part of this effort concentrates on extending [47, 48, 49] the symmetry classification valid for non-interacting systems [50, 51], and part of it is to map the phase diagrams of existing topological models with interactions turned on [52, 53]. One model of this type which has received considerable attention is the Kane-Mele-Hubbard (KMH) model [54] both analytically [55, 56] and numerically [57, 58]. For strongly correlated systems two of the most used variational wavefunctions are the Gutzwiller [59] and Baeriswyl [60, 61] wavefunctions. With some modifications, the Gutzwiller approximation can be applied to solve the Baeriswyl wavefunction (BWF). In the Gutzwiller approximation one assumes the absence of the structure of the exchange hole, i.e. that the only effect of the Pauli principle is that at each point in space there can be up to one electron of a particular

spin. To solve the BWF one can start with the same assumption in reciprocal space. The BWF can be viewed as the lattice analog of the so called shadow wavefunction [62], developed to study possible supersolid phases, and the general behavior of solid helium. However, given the important role that the BWF has played in describing strongly correlated models, its 1D exact solution would certainly be of interest. The BWF starts with the wave function at infinite interaction (a charge-density wave) and acts on this wavefunction with a kinetic energy based projector. It was originally developed for the fermionic Hubbard model, but Schiró and Fabrizio recently derived [63, 64] a time-dependent variational formalism and applied it to the Gutzwiller wavefunction within the Gutzwiller approximation. The idea of the formalism is to introduce time dependent projections with complex parameters which act on the wavefunction. The wavefunction and the Hamiltonian can be used to construct an action, which, when optimized gives classical equations of motion for the parameters of the complex projection and the expectation values of the operators which appear in the projection. It has also been applied to the bosonic Hubbard model [65] as well as quenches of interacting spinless fermions [66].

This thesis will be presented in six chapters. In Chapter 2, considering a parametrized curve $\boldsymbol{\xi}(\chi)$ we show that the product $\prod_{I=0}^{M-1}\langle\Psi_0(\chi_I)|\Psi_0(\chi_{I+1})\rangle$ can be equated to a cumulant expansion. The first contributing term of this expansion is the Berry phase itself, the other terms are the associated spread, skew, kurtosis, etc. Here we show that the cumulants are gauge invariant. It is also shown that these quantities can be expressed in terms of an operator. When the Wannier functions are localized within one unit cell, the probability distribution so obtained corresponds to that of the Wannier function.

In Chapter 3, we calculate the gauge-invariant cumulants (and moments) associated with the Zak phase in the RM and spinless SSH models. We reconstruct the underlying probability distribution by maximizing the information entropy and applying the moments as constraints. In RM model, we show that in the fully dimerized limit the magnitudes of the moments are all equal. In this limit, if the on-site interaction is decreased towards zero, the distribution shifts towards the midpoint of the unit cell, but the overall shape of the distribution remains

the same. Away from this limit, if alternate hoppings are finite and the on-site interaction is decreased, the distribution also shifts towards the midpoint of the unit cell, but it does this by changing shape, by becoming asymmetric around the maximum, and by shifting. We also follow the probability distribution of the polarization in cycles around the topologically nontrivial point of the model. The distribution moves across to the next unit cell, its shape distorting considerably in the process. If the radius of the cycle is large, the shift of the distribution is accompanied by large variations in the maximum. In spinless SSH model, we study the phase diagram and the total polarization distribution of the SSH model with nearest neighbor interaction in one dimension at half-filling.

To obtain the ground state wave-function, we extend the Baeriswyl variational wave function to account for alternating hopping parameters. The ground state energies of the variational wave functions compare well to exact diagonalization results. For the case of uniform hopping for all bonds, where it is known that an ideal conductor to insulator transition takes place at finite interaction, we also find a transition at an interaction strength somewhat lower than the known value. The ideal conductor phase is a Fermi sea. The phase diagram in the whole parameter range shows a resemblance to the phase diagram of the KMH model. We also calculate the gauge invariant cumulants corresponding to the polarization (Zak phase) and use these to reconstruct the distribution of the polarization.

We calculate the reconstructed polarization distribution along a path in parameter space which connects two points with opposite polarization in two ways. In one case we cross the metallic phase line, in the other, we go through only insulating states. In the former case, the average polarization changes discontinuously after passing through the metallic phase line, while in the latter the distribution 'walks across' smoothly from one polarization to its opposite. This state of affairs suggests that the correlation acts to break the chiral symmetry of the SSH model, in the same way as it happens when a RM onsite potential is turned on.

In Chapter 4, we study the analogs of Haldane and Kane-Mele models in one-dimension. In first part, we construct a 1D model, which exhibits with particle-hole and reflection symmetries. Gap closure occurs at finite parameter values separating two different quantum phases. The particle-hole symmetry operator for the model squares to minus one, therefore, the model falls in the C and CI classes [67, 68], however, the operator R which inverts the legs of the ladder anticommutes with the particle hole symmetry. Thus, our model has a $2M\mathbb{Z}$ topological index according to the classification of Chiu et al. [69, 70]. We also show that our model can be viewed as two models superimposed, each of which individually exhibits nontrivial topological behavior. The submodels are Creutz models [71, 72] with an external potential. The topological invariant of the complete system is the *mirror winding number*. We find edge states and a quantized Hall conductance in the topological phase. Applying the Peierls phase to another set of bonds results in the same topological behavior, but with reflection about a bond midpoint playing the role of R. We also consider adding a term which mixes the contributions from the two models but is particle-hole symmetry invariant. The winding number displays the same behavior, the edge states become nondegenerate.

In second part of this chapter, we construct a ladder model step-by-step, which can be viewed as the one-dimensional analog of the Kane-Mele model. First, we modify the original Creutz model so that gap closures are shifted in k-space, breaking time-reversal invariance. We, then, couple two such shifted Creutz models, one for each spin channel, so that time-reversal invariance is restored. We also add a Rashba term to allow for the mixing of spins. We then derive a topological winding number for the model, and calculate its phase diagram. We also use the Widom derivation of the quantum spin Hall formula, which gives quantized response in the topological region. The possible experimental signature is spin currents flowing along the legs of the ladder.

In Chapter 5, we consider the edge at the interface of a simple tight-binding model and a band insulator. We find that crossings in the band structure (one dimensional Dirac points) appear when an interface is present in the system. We calculate the hopping energy resolved along lines of bonds parallel to the interface

as a function of distance from the interface. Similarly, we introduce a transport coefficient (Drude weight) for charge currents running parallel to the interface. We find that charge mobility (both the kinetic energy and the Drude weight) is significantly enhanced in the at the surface of the tight-binding part of the model near the interface.

In Chapter 6, we study a variant of the generalized Aubry-André-Harper model with the effect of introducing next nearest-neighbor p-wave superconducting pairing with incommensurate and commensurate cosine modulations. We extend generalized Aubry-André-Harper model with p-wave superconducting to topologically equivalent and nontrivial an "ancestor" two-dimensional p-wave superconducting model. It is found that in incommensurate (commensurate) modulation, by varying next nearest-neighbor p-wave pairing order parameter, the system can switch between extended states and localized states (fully gapped phase and a gapless phase). In the incommensurate case, we numerically investigate the localization properties of the generalized Aubry-André-Harper model combined with the superconducting pairing. We show that localization transition can be induced by varying just the modulated superconducting pairing parameter, keeping all other model parameters constant. We also study the phase diagram of our model as a function of modulation amplitudes and the strength of the superconducting pairing by using the mean inverse participation ratio. Our calculations demonstrate that there exists different topological phase transition in this model such as a transition between delocalization states to Anderson localized states. In the commensurate case, we calculate the Chern numbers of the of the major gaps and discuss the evolution of topological properties for different superconducting pairing parameters.

Chapter 2

Polarization and gauge invariant cumulants

The most general way to obtain the Berry phase is to write it in the discrete representation, and then take the continuous limit. Pancharatnam's [73] original derivation is based on considering discrete phase changes. The discrete Berry phase first appeared in 1964, in a paper by Bargmann [74], as a mathematical tool for proving a theorem. The expression which forms the basis of our derivation here has also been used extensively in the case of path-integral based representation of geometric phases [75, 76].

Given a parameter space $\boldsymbol{\xi}$ and some Hamiltonian $H(\boldsymbol{\xi})$ with

$$H(\boldsymbol{\xi})|\Psi_i(\boldsymbol{\xi})\rangle = E_i(\boldsymbol{\xi})|\Psi_i(\boldsymbol{\xi})\rangle, \tag{2.1}$$

where $|\Psi_i(\boldsymbol{\xi})\rangle(E_i(\boldsymbol{\xi}))$ is an eigenstate(eigenvalue) of the Hamiltonian. Consider a set of M points in this parameter space $\{\boldsymbol{\xi}_I\}$. In this case one can form the quantity

$$\phi = -\mathrm{Im}\ln\prod_{I=0}^{M-1}\langle\Psi_0(\boldsymbol{\xi}_I)|\Psi_0(\boldsymbol{\xi}_{I+1})\rangle, \tag{2.2}$$

where $\Psi_0(\boldsymbol{\xi}_M) = \Psi_0(\boldsymbol{\xi}_0)$ (cyclic) which is physically well-defined since arbitrary phases cancel. In Eq. (2.4) ϕ is formed using the ground state, without loss

of generality. If the points $\{\boldsymbol{\xi}_I\}$ are points on a closed curve, one can take the continuous limit and obtain

$$\phi = i \oint \mathrm{d}\boldsymbol{\xi} \cdot \langle \Psi_0(\boldsymbol{\xi}) | \nabla_{\boldsymbol{\xi}} | \Psi_0(\boldsymbol{\xi}) \rangle. \tag{2.3}$$

The ϕ can be shown to be gauge invariant and is therefore a physically well-defined quantity. If the wavefunction can be taken to be real, then a nontrivial Berry phase corresponds to $\phi = \pi$ and will only occur if the enclosed region of parameter space is not simply connected. If the wavefunctions can not be taken as real then a non-trivial Berry phase can occur even if the parameter space is not simply connected.

In this chapter we consider a curve parametrized by a scalar and show that when the real part of the product in Eq. (2.2) is considered it leads to a physically well-defined quantity. More generally we show that the product in Eq. (2.2) can be expanded using the standard cumulant expression, with the first order term corresponding to the Berry phase, and the higher order terms giving gauge invariant and therefore physically well-defined quantities. It is also shown that the cumulants can be written in terms of an operator. We then consider the spread of polarization, which was given by Resta and Sorella [44], and show that the spread suggested by them coincides with that obtained from the cumulant expansion described here. We also analyze one of the canonical examples for the Berry phase [77] in light of our findings.

2.1 Gauge invariant cumulants associated with the Zak phase

Consider a one-dimensional system whose Hamiltonian which is periodic in L. We take Bloch functions parametrized by the crystal momentum, $\Psi_0(K)$ on a grid of M points $K_I = 2\pi I/(ML) - \pi/L$, with $I = 0, ..., M-1$ (see Fig. 2.1).

The Zak phase can be derived from a product of the form

$$\phi_{Zak} = \mathrm{Im}\ln\prod_{I=0}^{M-1}\langle\Psi_0(K_I)|\Psi_0(K_{I+1})\rangle, \tag{2.4}$$

by taking the continuous limit ($M \to \infty$). The product in Eq. (2.4) is known as the Bargmann invariant [74]. We will derive the Zak phase, as well as the associated gauge invariant cumulants (GIC). We start by equating the product in Eq. (2.4) to a cumulant expansion,

$$\left[\prod_{I=0}^{M-1}\langle\Psi_0(K_I)|\Psi_0(K_{I+1})\rangle\right]^{\Delta K} = \exp\left(\sum_{n=1}^{\infty}\frac{(i\Delta K)^n}{n!}\tilde{C}_n\right), \tag{2.5}$$

with $\Delta K = 2\pi/M$. We now expand both sides and equate like powers of ΔK term-by-term, mindful of the fact that the left-hand side includes a product over I. For example, the first-order term will be

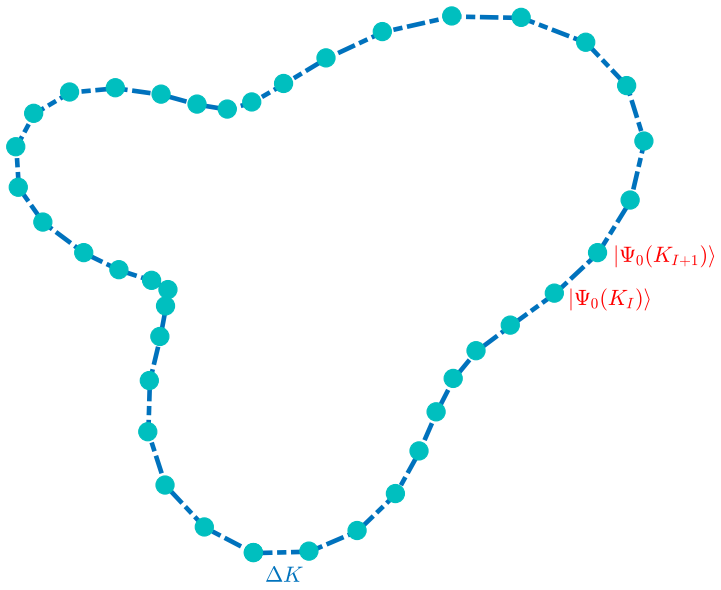

Figure 2.1: Discrete representation of a closed curve in parameter space.

$$\tilde{C}_1 = i\sum_{I=0}^{M-1}\Delta K\gamma_1(K_I) \tag{2.6}$$

the second will be

$$\tilde{C}_2 = -\sum_{I=0}^{M-1} \Delta K[\gamma_2(K_I) - \gamma_1(K_I)^2] \tag{2.7}$$

with $\gamma_n(K) = \langle \Psi_0(K)|\partial_K^n|\Psi_0(K)\rangle$. Straightforward algebra and taking the continuous limit ($\Delta K \to 0$, $M \to \infty$) gives up to the fourth order term,

$$\begin{aligned}
C_1 &= i\frac{L}{2\pi}\int_{-\frac{\pi}{L}}^{\frac{\pi}{L}} dK\gamma_1 \\
C_2 &= -\frac{L}{2\pi}\int_{-\frac{\pi}{L}}^{\frac{\pi}{L}} dK[\gamma_2 - \gamma_1^2] \\
C_3 &= -i\frac{L}{2\pi}\int_{-\frac{\pi}{L}}^{\frac{\pi}{L}} dK[\gamma_3 - 3\gamma_2\gamma_1 + 2\gamma_1^3] \\
C_4 &= \frac{L}{2\pi}\int_{-\frac{\pi}{L}}^{\frac{\pi}{L}} dK[\gamma_4 - 3\gamma_2^2 - 4\gamma_3\gamma_1 + 12\gamma_1^2\gamma_2 - 6\gamma_1^4]
\end{aligned} \tag{2.8}$$

The quantities C_n in Eq. (2.8) are the GICs associated with the Zak phase (the Zak phase itself being equal to C_1). The difference between $\tilde{C}_n$ and C_n is the multiplicative factor $L/2\pi$, which is also how the phase is defined by Zak ($\tilde{C}_n$) [34]. This assures that the first moment corresponds to the average position associated with square modulus of the Wannier function (Eq. (10) in Ref. [34]). When the underlying probability distribution is well defined the associated moments can be defined based on the cumulants. Following this standard procedure we also define a set of moments. For the first four moments the expressions are

$$\begin{aligned}
\mu_C^{(1)} &= C_1 \\
\mu_C^{(2)} &= C_2 + C_1^2 \\
\mu_C^{(3)} &= C_3 + 3C_2C_1 + C_1^3 \\
\mu_C^{(4)} &= C_4 + 4C_3C_1 + 3C_2^2 + 6C_2C_1^2 + C_1^4.
\end{aligned} \tag{2.9}$$

As discussed below, when the Wannier functions of a particular model are localized within the unit cell, these moments correspond to the moments of the polarization, alternatively, to the distribution of the Wannier functions themselves.

2.1.1 Cumulants connection vs. gauge-invariant quantity.

We remark that in general, the Berry phase is a physically well-defined observable, which is thought not to correspond to an operator acting on the Hilbert space. The Zak phase, however, is known to correspond to the total position, and is the basic quantity in expressing the polarization in the modern theory [35, 36, 37]. C_1 corresponds to the Berry phase. The other C_n look very similar to the usual cumulants (compare coefficients), provided that we can interpret $-i\partial_\chi$ as an operator and the integral as an expectation value. C_1 is known to be gauge invariant, therefore it is natural to ask whether the other C_n are also gauge invariant. We consider the proof of gauge invariance for C_1. One first alters the phase of the wavefunction, i.e. define

$$|\tilde{\tilde{\Psi}}_0(\chi)\rangle = \exp[i\beta(\chi)]|\Psi_0(\chi)\rangle. \tag{2.10}$$

Defining

$$\tilde{\tilde{C}}_1 = -i\int_0^\Lambda d\chi \langle\tilde{\tilde{\Psi}}_0(\chi)|\partial_\chi|\tilde{\tilde{\Psi}}_0(\chi)\rangle, \tag{2.11}$$

it is easy to show that

$$\tilde{\tilde{C}}_1 - C_1 = \beta(\Lambda) - \beta(0). \tag{2.12}$$

with $\tilde{\tilde{\gamma}}_n = \langle\tilde{\tilde{\Psi}}_0(\chi)|\partial_\chi^n|\tilde{\tilde{\Psi}}_0(\chi)\rangle$. Hence the Berry phase of the original wavefunction differs from the shifted one by the difference of $\beta(\Lambda)-\beta(0)$ which for an adiabatic cycle is $2\pi m$, with m integer. Applying the same procedure to the other cumulants we obtain the following results:

$$\begin{aligned}
\tilde{\tilde{C}}_2 - C_2 &= \dot{\beta}(\Lambda) - \dot{\beta}(0) = 0, \\
\tilde{\tilde{C}}_3 - C_3 &= \ddot{\beta}(\Lambda) - \ddot{\beta}(0) = 0, \\
\tilde{\tilde{C}}_4 - C_4 &= \dddot{\beta}(\Lambda) - \dddot{\beta}(0) = 0,
\end{aligned} \tag{2.13}$$

hence, if the function $\beta(\chi)$ and its derivatives are continuous at the boundaries gauge invariance holds. We have carried out this proof up to fourth order. There appears to be a pattern in Eq. (2.13).

2.1.2 Cumulants connection vs. perturbation theory

The cumulants derived above can be expressed in terms of expectation values of operators. Consider the expression from perturbation theory

$$\partial_\chi |\Psi_0(\chi)\rangle = \sum_{j\neq 0} |\Psi_j(\chi)\rangle\langle\Psi_j(\chi)| \frac{\partial_\chi H(\chi)}{E_j - E_0} |\Psi_0(\chi)\rangle. \tag{2.14}$$

Defining operator $\hat{O}$ as

$$\partial_\chi H(\chi) = i[H(\chi), \hat{O}] \tag{2.15}$$

it can be shown that the cumulants of this operator correspond to the C_n derived above, except for the case $n = 1$, the Berry phase itself, for which application of Eq. (2.14) leads to zero. For the Berry phase the expression from perturbation theory (Eq. (2.14)) is not valid since it makes a definite choice about the phase of the wavefunction for all values of χ. The most general expression is

$$|\Psi(\chi + \Delta\chi)\rangle = e^{i\alpha} \times \tag{2.16}$$
$$\left[|\Psi(\chi)\rangle + \left(\sum_{j\neq 0} |\Psi_j(\chi)\rangle\langle\Psi_j(\chi)| \frac{\partial_\chi H(\chi)}{E_j - E_0} |\Psi_0(\chi)\rangle \right) \right],$$

but in standard perturbation theory α is assumed to be zero. This phase difference shifts the first cumulant (the Berry phase), however since it is a mere shift, it leaves the other cumulants unaffected. One can conclude that while the Berry phase itself can not be expressed in terms of an operator, its associated cumulants can. This statement will be clarified in an example below.

2.2 Polarization, current and their spreads

We now consider the Berry phase corresponding to the polarization from the modern theory [35, 36, 37, 44]. In this theory an expression for the spread of a Berry phase associated quantity has been suggested, and we now show that it is equivalent to C_2/Λ.

Resta [44] showed that the expectation value of the position over some wavefunction $|\Psi_0\rangle$ of a system with unit cell dimension L can be written as

$$\langle X\rangle = -\frac{1}{\Delta K}\mathrm{Im}\ln\langle\Psi_0|e^{-i\Delta K\hat{X}}|\Psi_0\rangle, \tag{2.17}$$

where $\Delta K = 2\pi/(N_k L)$, N_k denotes an integer, $\hat{X} = \sum_j \hat{x}_j$ is the sum of the positions of all particles. The spread in position ($\sigma_X^2 = \langle X^2\rangle - \langle X\rangle^2$) can be written

$$\sigma_X^2 = -\frac{2}{\Delta K^2}\mathrm{Re}\ln\langle\Psi_0|e^{-i\Delta K\hat{X}}|\Psi_0\rangle, \tag{2.18}$$

The operator $e^{i\Delta K\hat{X}}$ is the total momentum shift operator which, as has been shown elsewhere [78, 79] has the property that for a state $|\Psi_0(K)\rangle$ with particular crystal momentum K defined as

$$\Psi_0(k_1 + K, k_2 + K, ...), \tag{2.19}$$

it holds that

$$e^{-i\Delta K\hat{X}}|\Psi_0(K)\rangle = |\Psi_0(K + \Delta K)\rangle, \tag{2.20}$$

in other words it shifts the crystal momentum by ΔK. To use the shift operator we first write

$$\sigma_X^2 = -\frac{2}{N_k\Delta K^2}\mathrm{Re}\ln\langle\Psi_0|e^{-i\Delta K\hat{X}}|\Psi_0\rangle^{N_k}. \tag{2.21}$$

We associate the state $|\Psi_0\rangle$ with a particular crystal momentum K_0,

$$|\Psi_0\rangle = |\Psi_0(K_0)\rangle. \tag{2.22}$$

Using the total momentum shift the scalar product can be rewritten as

$$\begin{aligned}\langle\Psi_0(K_0)|e^{-i\Delta K\hat{X}}|\Psi_0(K_0)\rangle &= \langle\Psi_0(K_0)|\Psi_0(K_1)\rangle \\ &= \langle\Psi_0(K_I)|\Psi_0(K_{I+1})\rangle,\end{aligned} \tag{2.23}$$

where $K_{I+1} = K_I + \Delta K$. To show the last equation one applies the Hermitian conjugate of the total momentum shift to $\langle\Psi_0(K_0)|$ I times and the total momentum shift operator to $|\Psi_0(K_0)\rangle$ $I + 1$ times and forms the scalar product. Thus we can also write

$$\langle\Psi_0(K_0)|e^{-i\Delta K\hat{X}}|\Psi_0(K_0)\rangle^{N_k} = \prod_{I=0}^{N_k-1}\langle\Psi_0(K_I)|\Psi_0(K_{I+1})\rangle. \tag{2.24}$$

The points K_I form an evenly spaced grid with spacing ΔK in the Brillouin zone. Using this result the spread can be rewritten as

$$\sigma_X^2 = -\frac{2}{N_k \Delta K^2} \sum_{I=0}^{N_k} \mathrm{Re} \ln \langle \Psi_0(K_I) | \Psi_0(K_{I+1}) \rangle, \tag{2.25}$$

We now expand the scalar product up to second order as

$$\langle \Psi_0(K_I) | \Psi_0(K_{I+1}) \rangle = 1 + \Delta K \langle \Psi_0(K_I) | \partial_K | \Psi_0(K_I) \rangle + \frac{\Delta K^2}{2} \langle \Psi_0(K_I) | \partial_K^2 | \Psi_0(K_I) \rangle. \tag{2.26}$$

Subsequent expansion of the logarithm and keeping all terms up to second order in ΔK results in a first order term of the form

$$\frac{N_k L^2}{2\pi^2} \mathrm{Re} \sum_{I=0}^{N_k - 1} \Delta K \langle \Psi_0(K_I) | \partial_K | \Psi_0(K_I) \rangle. \tag{2.27}$$

In the continuum limit ($N_k \to \infty$) the sum turns into the integral which gives the standard Berry phase, but since this integral is purely imaginary it will not contribute to the spread. The final result for the spread is

$$\sigma_X^2 = \frac{L}{2\pi} \sum_{I=0}^{N_k - 1} \Delta K \sigma_X^2(K_I) = \frac{L}{2\pi} \int_{-\pi/L}^{\pi/L} \mathrm{d}K \sigma_X^2(K), \tag{2.28}$$

where

$$\sigma_X^2(K) = -\langle \Psi_0(K) | \partial_K^2 | \Psi_0(K) \rangle + \langle \Psi_0(K) | \partial_K | \Psi_0(K) \rangle^2. \tag{2.29}$$

Eq. (2.28) is actually the average of the spread over the Brillouin zone. One can think of $i\partial_K$ as a "heuristic position operator" [80], and the quantity $\sigma_X^2(K)$ as the spread for a wavefunction with crystal momentum K. This spread of the position operator, derived by different means, has also been obtained by Marzari and Vanderbilt [81]. One can also start from the expression for the spread of the total current [82]

$$\sigma_K^2 = -\frac{2}{\Delta X^2} \mathrm{Re} \ln \langle \Psi_0 | e^{-i \Delta X \hat{K}} | \Psi_0 \rangle, \tag{2.30}$$

and apply exactly the same steps as in the case of the total position. This derivation results in

$$\sigma_K^2 = -\frac{1}{L} \int_0^L \mathrm{d}X [\langle \Psi_0(X) | \partial_X^2 | \Psi_0(X) \rangle - \langle \Psi_0(X) | \partial_X | \Psi_0(X) \rangle^2]. \tag{2.31}$$

2.3 Measurement of C_ns

While it has been shown that C_n are physically well-defined their measurement may not be trivial. The operator may not exist or be easily written down. In this case one can proceed as follows. Define:

$$\begin{aligned} \mathbf{\Pi} &= \prod_{I=0}^{M-1} \langle \Psi_0(\chi_I) | \Psi_0(\chi_{I+1}) \rangle, \\ \mathbf{\Pi}^{(o)} &= \prod_{I=0}^{M/2-1} \langle \Psi_0(\chi_{2I+1}) | \Psi_0(\chi_{2I+3}) \rangle, \\ \mathbf{\Pi}^{(e)} &= \prod_{I=0}^{M/2-1} \langle \Psi_0(\chi_{2I}) | \Psi_0(\chi_{2I+2}) \rangle. \end{aligned} \tag{2.32}$$

Using these definitions one can show that

$$\begin{aligned} C_3 &\approx \frac{2}{\Delta\chi^2} \mathrm{Im} \ln \left[\frac{(\mathbf{\Pi}^{(o)} \mathbf{\Pi}^{(e)})^{\frac{1}{2}}}{\mathbf{\Pi}} \right] + O(\Delta\chi^3), \\ C_4 &\approx \frac{4}{\Delta\chi^3} \mathrm{Re} \ln \left[\frac{(\mathbf{\Pi}^{(o)} \mathbf{\Pi}^{(e)})^{\frac{1}{4}}}{\mathbf{\Pi}} \right] + O(\Delta\chi^3). \end{aligned} \tag{2.33}$$

2.4 Connection to the distribution of Wannier centers

Cumulants of the type described in the previous section appear in the theory of polarization [83]. In this section we connect the cumulants to the distribution of Wannier centers. We consider a typical term contributing to cumulant C_M, which can be written in the form

$$C_{M,\alpha} = \frac{L}{2\pi} \int_{-\frac{\pi}{L}}^{\frac{\pi}{L}} dK \prod_{i=1}^{d} \langle u_{nK} | \partial_K^{m_i} | u_{nK} \rangle, \tag{2.34}$$

where $\sum_{i=1}^{d} m_i = M$ and where we have used the periodic Bloch functions $u_{nK}(x)$ as a basis. The periodic Bloch functions can be written in terms of Wannier

functions,

$$u_{nK}(x) = \sum_{p=-\infty}^{\infty} \exp(iK(pL - x))a_n(x - pL), \tag{2.35}$$

where $a_n(x)$ denote the Wannier functions. With this definition it holds that

$$\frac{L}{2\pi} \int_{-\pi/L}^{\pi/L} dK \int_0^L dx |u_{nK}(x)|^2 = \int_{-\infty}^{\infty} dx |a_n(x)| = 1. \tag{2.36}$$

We can rewrite a scalar product appearing in Eq. (2.34) as

$$\langle u_{nK}|\partial_K^m|u_{nK}\rangle = \sum_{\Delta p=-\infty}^{\infty} \exp(-iK\Delta pL) \int_{-\infty}^{\infty} dx \\ a_n^*(x - \Delta pL)(-ix)^m a_n(x). \tag{2.37}$$

Substituting Eq. (2.37) $C_{M,\alpha}$ and integrating in K results in

$$C_{M.\alpha} = \sum_{\Delta p_1=-\infty}^{\infty} ... \sum_{\Delta p_d=-\infty}^{\infty} \delta[\Delta P, 0] \tag{2.38}$$
$$\prod_{j=1}^{d} \left\{ \int_{-\infty}^{\infty} dx_j (-ix_j)^{m_j} a_n^*(x_j - \Delta p_j L) a_n(x_j) \right\},$$

where $\Delta P = \sum_{j=1}^{d} \Delta p_j$ and $\delta[\Delta P, 0]$ is a Kronecker delta.

We note that if the Wannier functions are localized in one unit cell, then the summation in the scalar product of Eq. (2.37) will be restricted to the term $\Delta p = 0$. In this case, the cumulants C_M will correspond to those of the Wannier centers.

2.5 Relation to response functions

The second GIC associated with the polarization gives a sum rule for the frequency-dependent conductivity. This was shown for a finite system by Kudinov [84], and the derivation was extended to periodic systems by Souza, Wilkens, and Martin [83], by replacing the ordinary matrix elements of the total position

operator by their counterparts valid in the crystalline case. Their result is

$$C_2 = \frac{\hbar}{\pi q_e^2 n_0} \int \frac{d\omega}{\omega} \bar{\sigma}(\omega), \tag{2.39}$$

where q_e denotes the charge, n_0 the density, and $\bar{\sigma}(\omega) = (V/8\pi^3) \int d\mathbf{k} \sigma^{\mathbf{k}}(\omega)$.

For an insulating (gapped) system one can show that the second cumulant provides an upper bound for the dielectric susceptibility, χ. This was shown by Baeriswyl [61] for an open system. This derivation is also easily extended to periodic systems by the appropriate replacement of the total position matrix elements, resulting in,

$$\chi \leq \frac{2q_e}{V\Delta_g} C_2. \tag{2.40}$$

In this equation Δ_g denotes the gap, V denotes the volume of the system.

For higher order cumulants, the derivation of relations such as Eq. (2.40) are not possible. However, in the classical limit, the cumulants correspond exactly to the response functions of their respective order (C_2 gives χ, C_3 gives the first non-linear response function, etc.).

2.6 Examples

2.6.1 A spin-$\frac{1}{2}$ particle in a precessing magnetic field

We now calculate the cumulants up to fourth order for one of the canonical examples for the Berry phase [77], a spin-$\frac{1}{2}$ particle in a precessing magnetic field. The Hamiltonian is given by

$$\hat{H}(t) = -\mu \mathbf{B}(t) \cdot \boldsymbol{\sigma}, \tag{2.41}$$

where $\boldsymbol{\sigma}$ are the Pauli matrices, and $\mathbf{B}(t)$ denotes the magnetic field,

$$\mathbf{B}(t) = \begin{bmatrix} \sin\theta\cos\phi \\ \sin\theta\sin\phi \\ \cos\theta \end{bmatrix}. \tag{2.42}$$

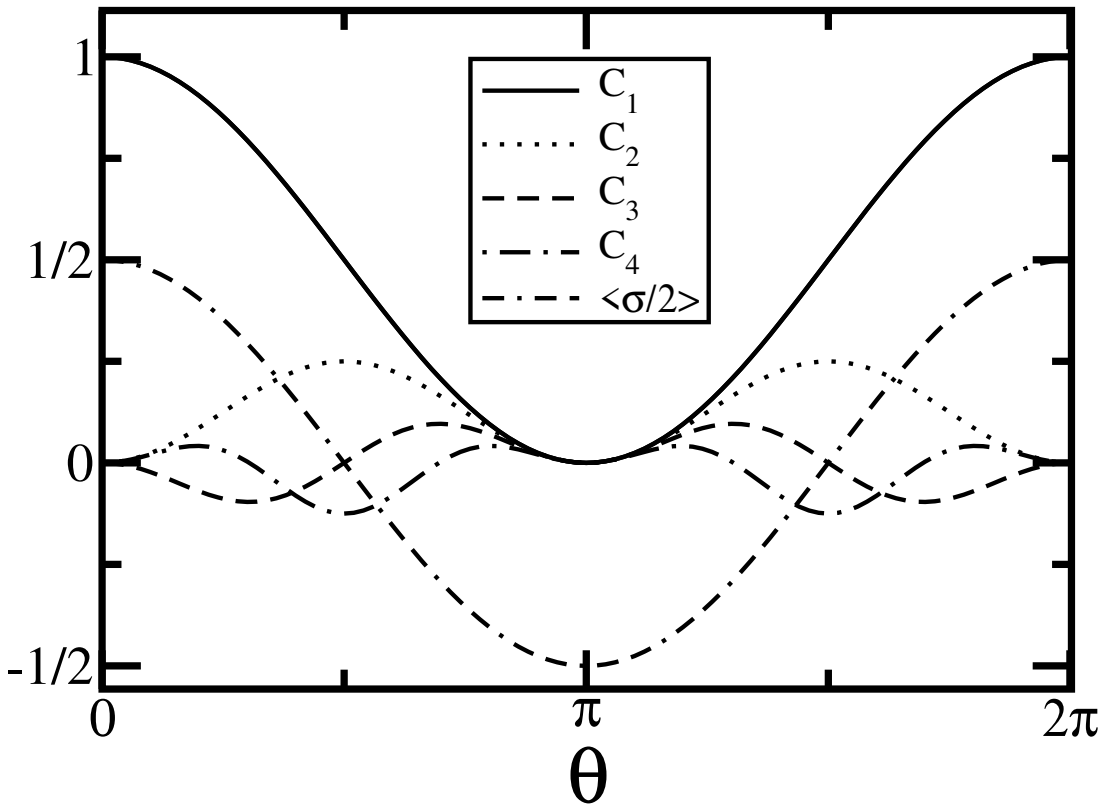

Figure 2.2: Cumulants of a spin$-\frac{1}{2}$ particle in a precessing field.

The z-component of the field is fixed, the projection on the $x-y$-plane is performing rotation, i.e. $\phi = \omega t$. We can proceed to evaluate the Berry phase and the associated cumulants by defining an adiabatic cycle in which ϕ rotates from zero to 2π. Using one of the eigenstates

$$|n_-(t)\rangle = \begin{bmatrix} -\sin\left(\frac{\theta}{2}\right) \\ e^{i\phi}\cos\left(\frac{\theta}{2}\right) \end{bmatrix}. \tag{2.43}$$

The associated cumulants (divided by 2π) evaluate to

$$\begin{aligned} C_1 &= \cos^2\left(\tfrac{\theta}{2}\right), \\ C_2 &= \left[\cos^2\left(\tfrac{\theta}{2}\right) - \cos^4\left(\tfrac{\theta}{2}\right)\right], \\ C_3 &= \left[\cos^2\left(\tfrac{\theta}{2}\right) - 3\cos^4\left(\tfrac{\theta}{2}\right) + 2\cos^6\left(\tfrac{\theta}{2}\right)\right], \\ C_4 &= \left[\cos^2\left(\tfrac{\theta}{2}\right) - 7\cos^4\left(\tfrac{\theta}{2}\right) + 12\cos^6\left(\tfrac{\theta}{2}\right) - 6\cos^8\left(\tfrac{\theta}{2}\right)\right]. \end{aligned} \tag{2.44}$$

Fig. 2.2 shows the cumulants as a function of the angle θ. C_1, the Berry phase associated with a spin$-\frac{1}{2}$ particle in a precessing magnetic field is a well-known

result. The spread is zero when the Berry phase is zero or π. The skew changes sign halfway between zero and π and the kurtosis also varies in sign as a function of the angle θ.

The operator $\hat{O}$ for this example can easily be shown to be the Pauli matrix $\frac{\sigma_z}{2}$. The first order cumulant is given by

$$\left\langle \frac{\sigma_z}{2} \right\rangle = \sin^2\left(\frac{\theta}{2}\right) - \cos^2\left(\frac{\theta}{2}\right). \tag{2.45}$$

in other words it is merely shifted compared to the Berry phase. The higher order cumulants are identical to those in Eqs. (2.44). In the operator representation of the Berry phase the meaning of the first and second cumulants is rendered more clear. For the value of θ for which $\langle \sigma_z/2 \rangle$ is either $\pm\frac{1}{2}$ the spread is zero. Indeed those are the maximum and minimum values the operator σ_z can take, hence the spread must be zero. It is obvious from these results that the cumulants derived from the Bargmann invariant give information about the probability distribution of the operator associated with the Berry phase.

2.6.2 Generalized Aubry–André model

We consider the generalized one-dimensional Aubry-André model, which is described by the following Hamiltonian

$$\hat{\mathcal{H}}_{GAA} = -\sum_{j=1}^{L} \Big[(t + \delta_j) c_{j+1}^{\dagger} c_j + \text{H.c.} \Big] + \sum_{j}^{L} \varepsilon_j \hat{n}_j \tag{2.46}$$

where

$$\begin{cases} \delta_j = \delta \cos(2\pi\beta j + \phi_\delta), \\ \varepsilon_j = V \cos(2\pi\beta j + \phi_V). \end{cases} \tag{2.47}$$

are commensurate (incommensurate) hopping modulations with periodicity $1/\beta$ and phase factor ϕ_δ, and the diagonal potential with periodicity $1/\beta$ and phase factor ϕ_V, respectively. The corresponding modulation amplitudes is set by δ, and V is the on-site potential strength. $\hat{n}_j = c_j^{\dagger} c_j$ are number operators, $c_j^{\dagger}(c_j)$ is the creation (annihilation operators) at position j on the lattice and t is the

hopping (or tunneling) amplitudes to the nearest neighbors. In the limit $\delta = 0$ (without off-diagonal modulation), this model reduces to the usual Aubry-André model [9]. Under this same conditions, for $V/t = 2$, it was shown by Harper [13] that this Hamiltonian can be formally derived from the reduction of an electron on a square lattice in a perpendicular magnetic field to a one-dimensional chain. The parameter $\beta = \Phi/\Phi_0$ denotes the flux quanta per plaquette. A rational (irrational) value of β renders the on-site potential periodic (quasiperiodic). On the other hand, when the relation between the hopping modulation and on-site phases are fixed, for example, $\phi_\delta = \phi_V + \beta\pi$, the GAA model can be formally derived from an ancestor 2D quantum Hall system on a lattice (Hofstadter model) with diagonal (next-nearest-neighbor) hopping terms [10, 14, 15]. However, experimentally, it is possible to design setups where hopping modulation and on-site phases can be tuned independently such as coupled optical waveguides [10, 15] by modulating the spacing between the widths and the waveguides. In this part, we will focus on the topological properties of the GAA model in terms of the independent hopping modulation and on-site phases.

There is no phase transition in the GAA model when β is rational. To highlight the new physics involved in the pure commensurate modulations of GAA model, we study the GICs with different values of the δ. When β is rational, the lattice is commensurate. We consider the $\beta = 1/2$ case when the even and odd sites feel different on-site potentials and commensurate hopping. It is well known that in the commensurate case, the system will not undergo a localization-delocalization transition as that in the incommensurate case. When $\beta = 1/2$, the Hamiltonian in Eq. (6.8) becomes

$$\begin{aligned}\hat{H} = &-\sum_j \Big[(t - \delta\cos(\phi_\delta))c_{2j}^\dagger c_{2j-1} + (t + \delta\cos(\phi_\delta))c_{2j+1}^\dagger c_{2j} + \text{H.c.})\Big] \\ &+ V\cos(\phi_V)\sum_j (c_{2j-1}^\dagger c_{2j-1} - c_{2j}^\dagger c_{2j})\end{aligned} \tag{2.48}$$

Then for this dimer chain, we use different notation for annihilation operators

over odd (as A-sites) and even sites (as B-sites).

$$\begin{aligned}\hat{H} = &-\sum_{j}\Big[(t-\delta\cos(\phi_\delta))c^{\dagger}_{B,j}c_{A,j} + (t+\delta\cos(\phi_\delta))c^{\dagger}_{A,j+1}c_{B,j} + \text{H.c.})\Big] \\ &+ V\cos(\phi_V)\sum_{j}^{L}(c^{\dagger}_{A,j}c_{A,j} - c^{\dagger}_{B,j}c_{B,j})\end{aligned} \tag{2.49}$$

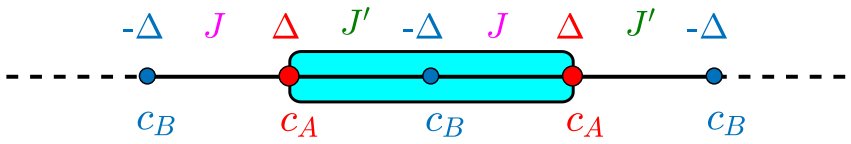

Figure 2.3: Schematic representation of the pure commensurate modulations of GAA model (blue box denotes the unit cell). c_A and c_B represents the different sublattices, and V refer to the on-site potential. J and J' are the alternating hoppings.

In this dimer Hamiltonian, $c^{\dagger}_{A,n}$ ($c^{\dagger}_{B,n}$) terms are the creation operators of particle localized on site A (or B) of the nth lattice cell (see Fig. 2.3). The variables J and J' in the above expression corresponds to

$$\begin{cases} J = t - \delta\cos(\phi_\delta), \\ J' = t + \delta\cos(\phi_\delta). \end{cases} \tag{2.50}$$

At half filling, the pure commensurate modulations of GAA model is a metal for $J = J'$, and an insulator otherwise. In order to characterize the topological phases, we need to calculate the gauge-invariant cumulants (and moments) associated with the Zak phase. First, in the basis of $[c^{\dagger}_{A,j}, c^{\dagger}_{B,j}]^T$, we transform the Hamiltonian into the momentum representation which can be written as

$$\begin{bmatrix} V\cos(\phi_V) & -\rho_k \\ -\rho_k^* & -V\cos(\phi_V) \end{bmatrix}\begin{pmatrix}\alpha_k \\ \beta_k\end{pmatrix} = \varepsilon_k\begin{pmatrix}\alpha_k \\ \beta_k\end{pmatrix} \tag{2.51}$$

where $\rho_k = Je^{ik} + J'e^{-ik}$. Solving Eq. (2.51), we obtain for the eigenenergies

$$\varepsilon_k = \pm\sqrt{J^2 + J'^2 + 2JJ'\cos(2k) + (V\cos(\phi_V))^2} \tag{2.52}$$

At a particular value of k we can write the eigenstate for the lower band as

$$\begin{pmatrix}\alpha_k \\ \beta_k\end{pmatrix} = \begin{pmatrix}\sin(\frac{\theta_k}{2}) \\ e^{-i\gamma_k}\cos(\frac{\theta_k}{2})\end{pmatrix}, \tag{2.53}$$

where

$$\theta_k = \arctan\left(\frac{|\rho_k|}{\Delta}\right),$$
$$\gamma_k = \arctan\left(\frac{(J - J')\sin(k)}{(J + J')\cos(k)}\right). \tag{2.54}$$

The cumulants can now be written in terms of the eigenstates.

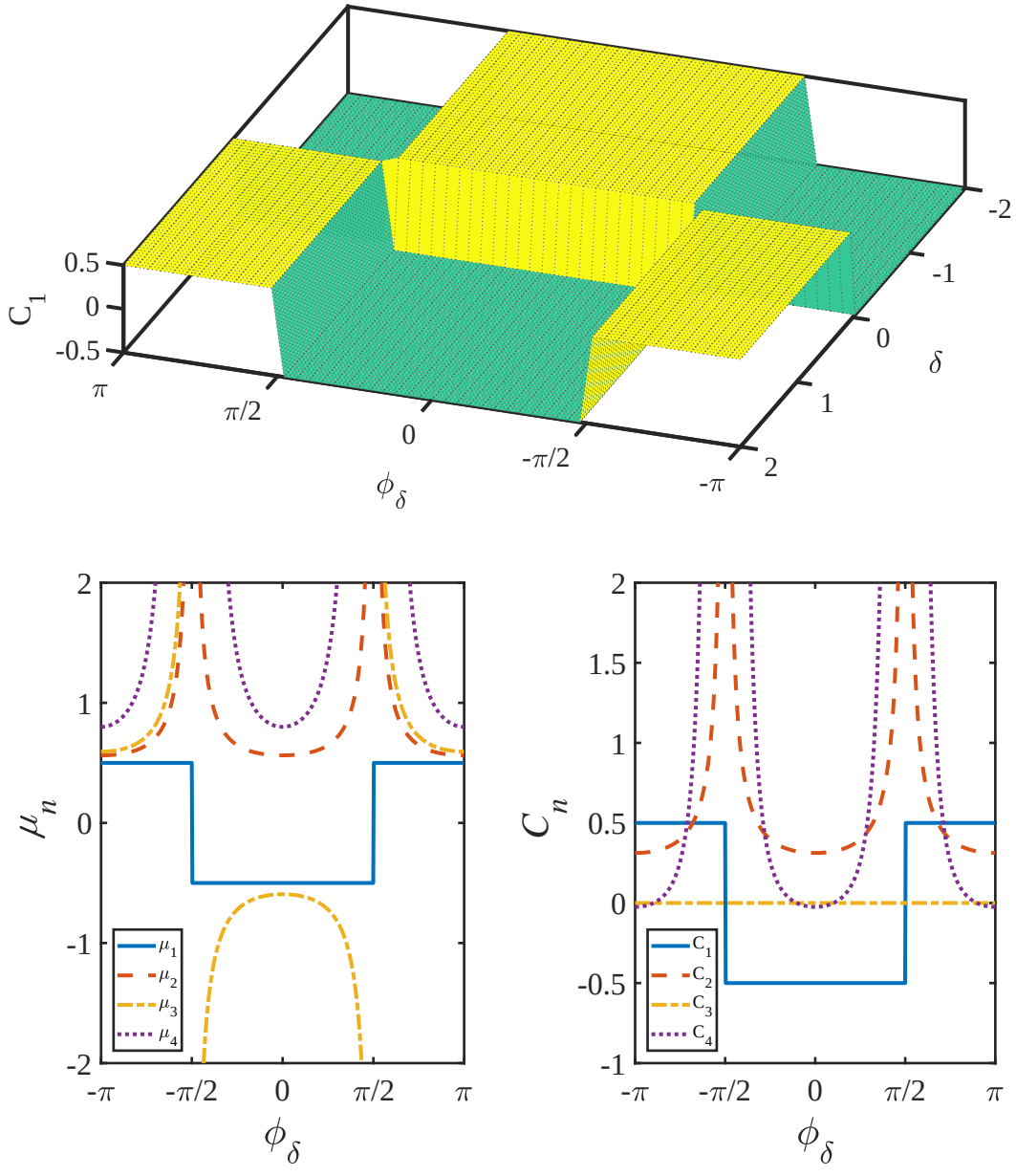

Figure 2.4: Moments and cumulants of GAA model for $\delta = 0.5$, $\phi_V = 0$, and $V = 0$ as a function of ϕ_δ.

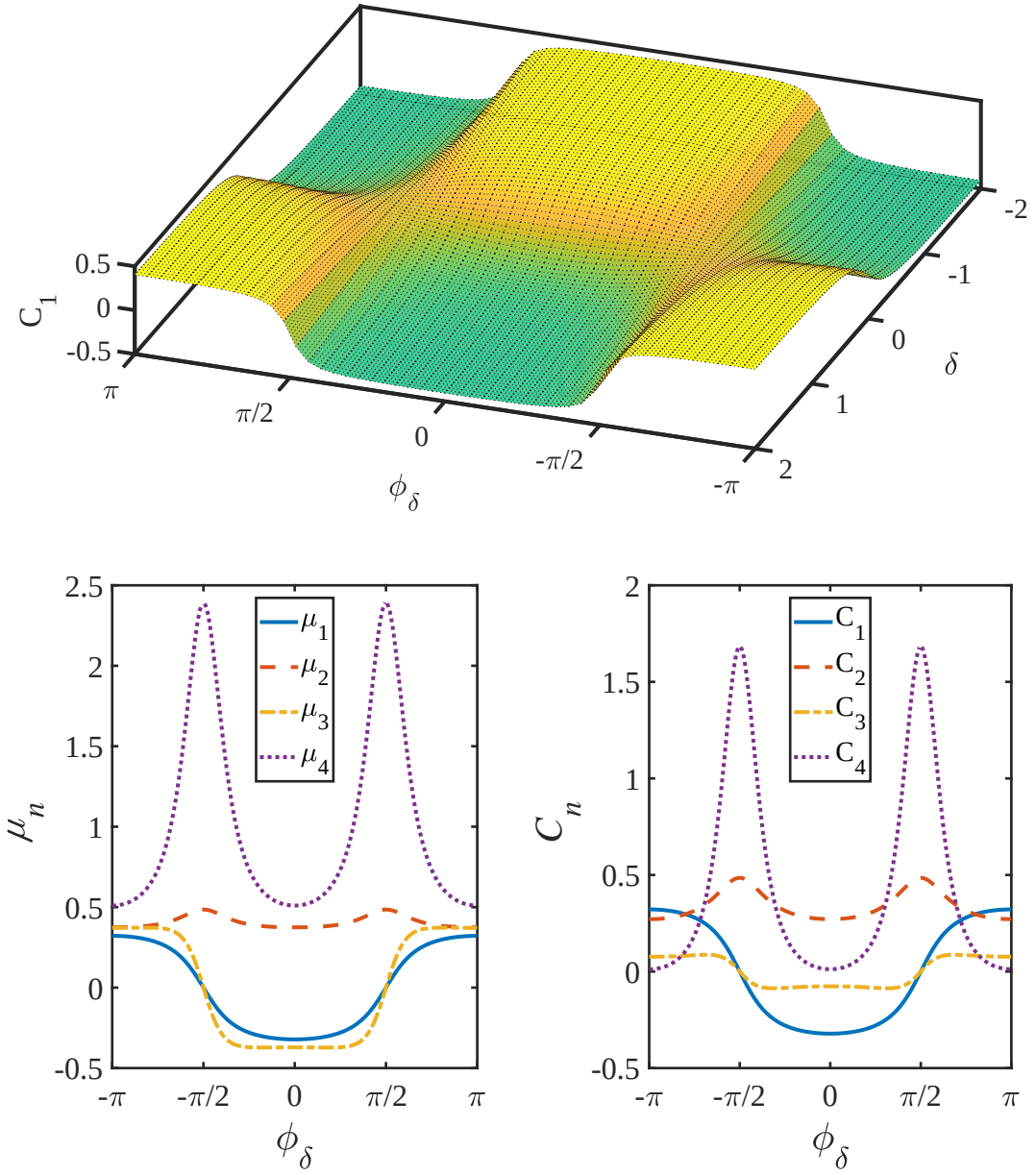

Figure 2.5: Moments and cumulants of GAA model for $\delta = 0.5$, $\phi_V = 0$, and $V = 0.5$ as a function of ϕ_δ.

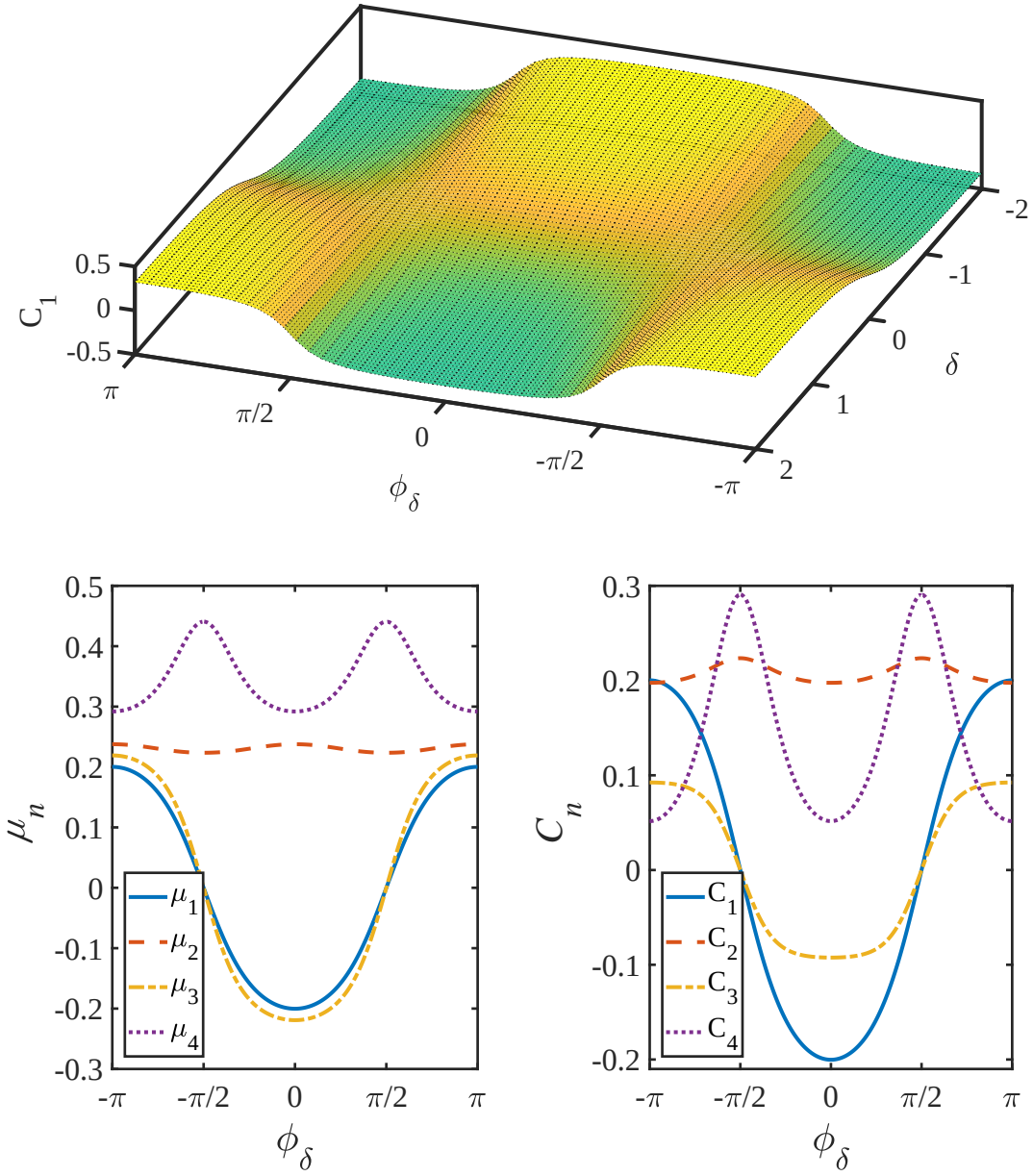

Figure 2.6: Moments and cumulants of GAA model for $\delta = 0.5$, $\phi_V = 0$, and $V = 1$ as a function of ϕ_δ.

2.6.3 Results and analysis

In this section, we extend the results presented in Ref. [40] as regards the GAA model to the case with two periodic phase parameters which acting as artificial dimensions to simulate 3D models. For the wave functions in Eq. (2.53), we calculated the first six GICs (first four GICs are shown here), from which we obtained the corresponding moments of GAA model versus ϕ_δ in Figs. 2.4-2.6 for $V = 0, 0.5, 1$, respectively.

We first look at the system with $V = 0$, which corresponds to the off-diagonal of GAA model with chiral symmetry. It can be seen that $\phi_\delta = \pm\pi/2$ is the critical point for topological phase transition where the sign of the first cumulant changes. When $-\pi/2 < \phi_\delta < \pi/2$ (or $J/J' > 1$), the first cumulant is thus identical $C_1 = -0.5$. On the other hand, for $\pi/2 < \phi_\delta < -\pi/2$ (or $J/J' < 1$), the first cumulant belongs to 0.5 and the signs of C_1 are inverted. We emphasize that, in general, the first cumulant depends on the choice of unit cell for the crystal. Similarly to Ref. [85], for the SSH model the Zak phase reduce to 0 and 1 rather than by $\pm 1/2$, as in some previous studies [40, 86]. Here, we find that the for our choice of the unit cell of the pure commensurate modulations of GAA model the first cumulants (C_1) are given by $\pm 1/2$. In this situation, to change the value of the C_1 one has to induce a topological transition. For $V = 0$, there is a sharp transition in C_1 from $1/2$ to $-1/2$ at $\phi_\delta = \pm\pi/2$. In this case, the cumulants C_2 (spread) and C_4 (kurtosis) diverge. Because of the chiral symmetry, for all value of ϕ_δ, the cumulant C_3 (skew) is zero. Actually, to change the value of the C_1 one has to induce a topological transition, or one has to pull the loop of $h(k) = ((J + J')\cos(k), (J - J')\sin(k), V\cos(\phi_V))$ through the origin in the $(d_x; d_y)$ plane. It can be seen that with an increase of the quasi-disorder strength V/t, phase change during the gradual transition. We now consider adiabatic deformation of insulating Hamiltonians with increase the potential, δ, which breaks chiral symmetry. Figures 2.5 and 2.6 also show the cumulants and moments for two values of the potential strength, $V = 0.5$ and 1. It can be seen that with an increase of the V, the Zak phase change during the gradual transition and C_3 is finite. Consequently, first cumulant or moment

can only take the value $1/2$ or $-1/2$ (modulo 2), in this case, because the system lacks inversion symmetry, they can have any values.

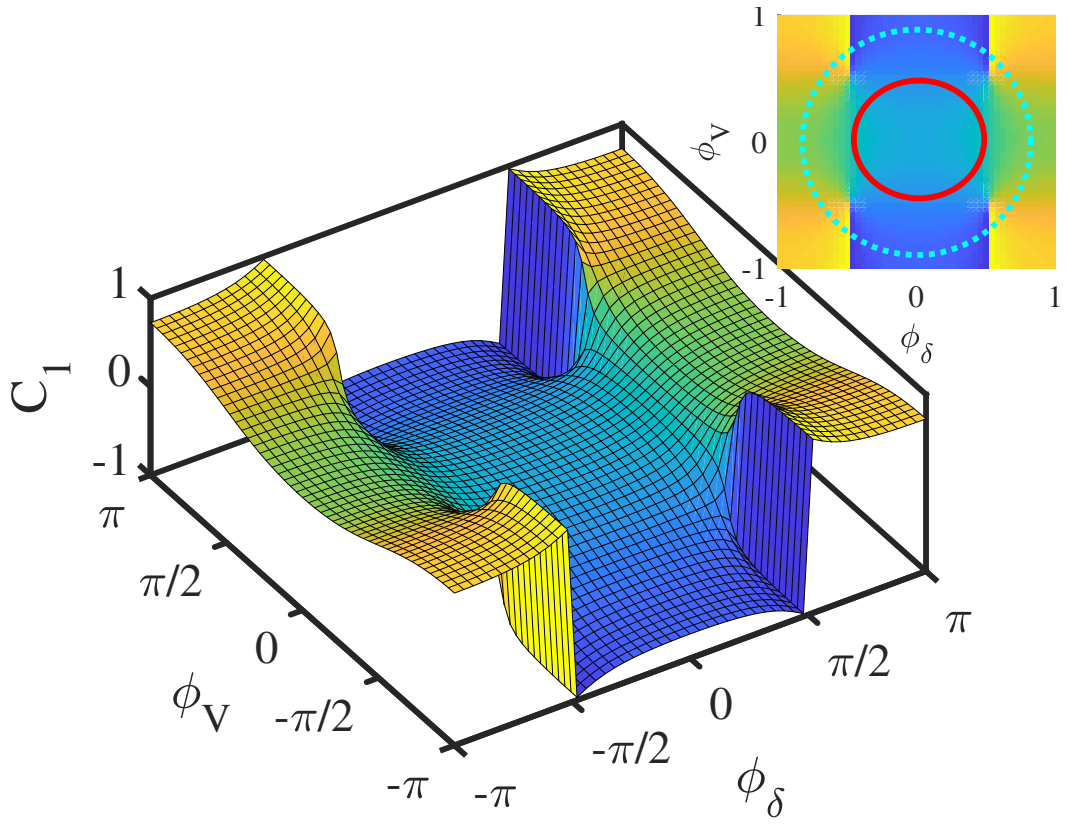

Figure 2.7: Polarization as a function of ϕ_δ and ϕ_V in the pure commensurate modulations of GAA Hamiltonian.At $\phi_\delta = 0$ and $\phi_V = 0$, if the radius of closed path encloses it is larger than $\pi/2$, there are foure singularities (from the first cumulant in a 3D plot we can appreciate the singularities) and the change in polarization is equal to $e/2$ (dash line circle of right inset). Also, if the radius of close path is smaller than $\pi/2$, the change in polarization is equal to zero (solid line circle of right inset).

In the following we will show how the C_1 (Zak phase) difference between the dimerizations $J > J'$ and $J < J'$ in the GAA model is related to a polarization change. King-Smith and Vanderbilt proved that the polarization change is related to the Zak phase [35]. The change in the polarization density is given by

$$\Delta P = -\frac{e}{2\pi}\int_{\lambda_0}^{\lambda_1} d\lambda \int_{-\pi}^{\pi} dk\ \Omega_{k,\lambda} \tag{2.55}$$

where $\Omega_{k,\lambda}$ indicates the Berry curvature. In this expression we have modified the

Hamiltonian with $\phi_\delta(\lambda)$ and $\phi_V(\lambda)$. Also, we have assumed that the adiabatic transformation is parametrized by λ. The Berry curvature for a two-dimensional parameter space (k, λ) takes the form

$$\Omega_{k,\lambda} = \partial_k A_\lambda - \partial_\lambda A_k \tag{2.56}$$

where the quantity A_λ and A_k are named the Berry connection and can be expressed as

$$\begin{cases} A_\lambda = \alpha_k^* \partial_\lambda \alpha_k + \beta_k^* \partial_\lambda \beta_k = \cos^2(\Theta(k,\lambda)) \partial_k \Gamma(k,\lambda), \\ A_k = \alpha_k^* \partial_k \alpha_k + \beta_k^* \partial_k \beta_k = \cos^2(\Theta(k,\lambda)) \partial_\lambda \Gamma(k,\lambda). \end{cases} \tag{2.57}$$

where $\Theta(k,\lambda) = \theta_k$ and $\Gamma(k,\lambda) = -\gamma_k$ are obtained from Eq. 2.54. Here, it is important to remark that the dependence on λ is implicit. Substituting this Berry curvature into the polarization density of Eq. 2.55 one arrives at

$$\Delta P = -\frac{e}{2\pi} \int_{-\pi}^{\pi} dk \ \cos^2(\gamma_k/2) \partial_k \theta_k \Big|_{\lambda_0}^{\lambda_1} \tag{2.58}$$

Comparing this equation with Zak phase (expression (2.59))

$$C_1 = \frac{1}{\pi} \int_{-\pi/2}^{\pi/2} \cos^2 \frac{\theta_k}{2} \partial_k \gamma_k \, dk, \tag{2.59}$$

reveals an elegant structure: polarization density can be regarded as the manifestation of the difference of the first cumulant (or Zak phase) between the initial and final states. Figure (2.7) displays the calculated first cumulant (Zak phase) and polarization as a function of ϕ_δ and ϕ_V. One can observe that at ($\phi_\delta = 0$, $\phi_V = 0$), when the radius of closed path encloses it, is larger than $\pi/2$, there are four singularities (because the periodicity of the system changing and the lower and upper bands touch each other), then the polarization density will be changed by $e/2$. For example, to change ϕ_δ and ϕ_V in time along this loop, one can consider that, $\phi_\delta(\lambda) = \phi_{\delta_0} \sin(\lambda)$ and $\phi_V(\lambda) = \phi_{V_0} \cos(\lambda)$. One should also remark that it depends on how many times the loop ($\phi_\delta(\lambda)$, $\phi_V(\lambda)$) encloses these singularities. The example with a radius smaller than $\pi/2$ remains mostly in the non-singularity limit, as can be seen in the inset panel of Fig. (2.7).

Chapter 3

Reconstruction of the probability distribution

In the previous chapter, we discused the gauge-invariant cumulants (GICs) associated with the Berry phase. One is lead to ask two questions. Which physical quantity do the GICs give information about? Can one reconstruct the probability distribution from the GICs?

The answer to the first question depends on the physical context in which the Berry phase is defined. In a crystalline solid the Berry phase (or Zak phase [34], in this context) corresponds to the macroscopic polarization. Zak showed [34] that the phase itself corresponds to the expectation value of the position over a Wannier function. For the higher order GICs Souza, Wilkens and Martin [83] showed that they only correspond to the cumulants of the distribution of the position associated with Wannier functions, if the Wannier functions themselves are localized within the unit cell (non-overlapping among different unit cells). Indeed, in the construction of tight-binding based lattice models, one starts with a continuum description, and assumes a localized basis of non-overlapping Wannier functions (see for example, Ref. [79]). In practice, however, constructing such a localized basis is not trivial [81].

The distribution of the polarization gauges the extent to which the system is localized in the full configuration space, a criterion [87] which distinguishes an insulator from a conductor. The second GIC was shown [84, 83] to be proportional to the integrated frequency dependent conductivity (sum rule). A gauge dependent definition of the spread (similar to the second GIC) was used to define the maximally localized Wannier function [81]. Also, the second cumulant was proposed [44] to distinguish conductors from insulators. In Ref. [39] the simplest system with a Berry phase, an isolated spin-$\frac{1}{2}$ particle in a magnetic field, was considered, and it was shown that (based on calculating the first four cumulants) the moments of this underlying distribution are all equal.

The Zak phase was measured in Ref. [86] in an optical lattice setup which corresponds to the experimental realization of the SSH model [88] and its extension the RM model [89]. The RM model is a lattice model with an alternating on-site potential, and hoppings with alternating strengths, depending on whether a given bond is odd or even. An interesting characteristic [90, 91] of the RM model is its topological behavior which manifests when an adiabatic cycle in the parameter space of the Hamiltonian encircles the point ($\Delta = 0$, $J = J' = 1$). Due to the fact that the polarization as a function of the parameters of the Hamiltonian is not single valued, the polarization in such a process changes by a "polarization quantum." A recent related study [92] realized quantized adiabatic charge pumping [93], also in the RM model.

In first part of this chapter, we calculate the leading GICs associated with the Zak phase for the RM model. Based on the GICs (or associated moments, GIMs) we approximately reconstruct the distribution associated with the polarization. The RM model is a lattice model, which implies that the underlying Wannier functions are non-overlapping among different unit cells, and that the GICs correspond to the distribution associated with the Wannier function. Hence, our reconstructed probabilities correspond to the squared modulus of the Wannier function. We show that in the fully dimerized limit the GIMs should all have the same magnitude, and that the sign of odd GIMs switch sign with respect to the direction of the polarization. We also focus on the line of the parameter plane

where the polarization shows a discontinuity. We also present two model calculations in which the evolution of the probability distribution is followed around the topologically nontrivial point of the RM model. As expected, the distribution migrates to the next unit cell, although its shape varies considerably during the cycle.

In second part, we study the one-dimensional spinless interacting SSH model [88]. The spinful version of this model was studied by Manmana et al. [94]. So far, although topological, the spinless version of this model has received relatively little attention. We develop a variational approach by extending the Baeriswyl wave function [95, 61] (BWF) to account for the alternating hoppings of the SSH. We compare the ground state energies to exact diagonalization results for small system sizes, finding excellent agreement. The phase diagram we find is remarkably similar to that of the KMH model [46, 54]. When all hopping parameters are equal, we find a conducting phase for small interaction (in our variational treatment a Fermi sea), and a correlated insulator with charge density wave ordering for large interaction. When the hoppings alternate, the small interaction phase is the SSH ground state, but as the interaction increases, the system tends towards charge density order, which is weakened by the hopping alternation. We also construct a parent Hamiltonian for the BWF type wave function we use. Our construction allows for plotting the curves traced out by varying k across the Brillouin zone in the space spanned by the components of the Hamiltonian.

We then study the behavior of the polarization distribution. In particular, we do reconstructions along two paths in the parameter space of the model, which connect topologically distinct states. Both paths connect two states with finite interaction parameter, but with opposite polarity in hopping. One path crosses the metallic phase line (the interaction parameter is constant), while the other passes through the insulating regime only (the interaction is varied). We find that in the first case, the maximum of the distribution remains constant until the metallic phase line is reached, there the distribution flattens, and after passing to the other side of the metallic phase line, the distribution has a maximum at a different polarization (a jump occurred in the Berry phase at the metallic phase

line). For the second path, the maximum, as well as the other cumulants vary smoothly, the distribution "walks across" from one polarization to the other.

To make sense of these results, we relate them to the well-known topological quantum phase transition which occurs in the SSH model. In the SSH model chiral symmetry gives rise to a symmetry protected topological phase separated from a topologically trivial phase by gap closure. Again we reconstruct the polarization distribution along two different paths. Both paths pass between topologically distinct phases, but along one the symmetries are always respected (gap closure occurs), while along the other, the symmetries are relaxed. The polarization distributions evolve exactly in the same manner.

3.1 Reconstruction of the probability distribution by maximizing information entropy

If the Wannier functions can be assumed to be localized within a unit cell, the moments calculated based on the GICs correspond to the actual moments associated with the Wannier orbitals. If all the moments are known, the full probability distribution can be reconstructed. However, in practice, usually only a finite number of cumulants are available. In this case, the cumulants can be used as constraints to improve the form of the probability distribution. The first and second cumulants give the average and the variance, and if only these two are available, the best guess for the probability distribution is a Gaussian. Higher order cumulants refine this guess. The third cumulant (skewness) provides information about the asymmetry of the distribution around the mean, while the fourth order one, (kurtosis) represents how sharp the maximum of the distribution is approached from either side.

Below we calculate the GICs of the Rice-Mele model, which is a lattice model (in other words, the Wannier functions are completely localized on particular

sites), and approximately reconstruct the probability distribution of the polarization. Our reconstruction is based [96, 97, 98] on maximizing information entropy under the constraints provided by the moments calculated. The expression for the entropy we use is

$$S[P(x)] = -\int dx P(x) \ln P(x), \tag{3.1}$$

minimized as a functional of $P(x)$ under the constraints

$$\mu_P^{(k)} = \int dx P(x) x^k, \tag{3.2}$$

as well as the constraint that $P(x)$ is normalized. The functional minimization of Eq. (3.1) under the constraints results in the functional differential equation

$$\frac{\delta}{\delta P(x)} \left[S[P(x)] - \sum_k A_k (\mu_P^{(k)} - \mu_C^{(k)}) \right] = 0, \tag{3.3}$$

where $\mu_C^{(k)}$ are the moments obtained from the cumulants of the Berry phase (see Eq. (2.9)), and A_k are Lagrange multipliers. The solution of Eq. (3.3) is

$$P(x) = C \exp\left(-\sum_k A_k x^k \right), \tag{3.4}$$

where C is the normalization constant. We determine the constants A_k by numerically minimizing the quantity

$$\chi^2 = \sum_k (\mu_P^{(k)} - \mu_C^{(k)})^2, \tag{3.5}$$

as a function of A_k. As our initial guess in all cases studied below, we take the Gaussian distribution defined by the first two cumulants obtained for the particular case. The minimization procedure we applied is the simulated annealing technique [99]. Below our reconstructions are based on calculating the first six GIMs in all cases.

3.2 Su-Schrieffer-Heeger and Rice-Mele models

The SSH model was first introduced [18] to understand the properties of one-dimensional polyacetylene. The RM model is an extension of the SSH model, it

includes an additional term, consisting of an alternating on-site potential, added in order to extend the SSH model to diatomic polymers. In recent decades it has been studied extensively due to the wealth of interesting physical phenomena it displays: topological soliton excitation, fractional charge, and non-trivial edge states[100, 88, 101, 102, 103, 104]. It was also realized as a system of cold atoms trapped in an optical lattice in one dimension recently [86]. The Berry phase in the RM model was studied by Vanderbilt and King-Smith [90]. In that study the point of the model in parameter space of the model which is metallic (and which is responsible for the topologically nontrivial behavior) was encircled in parameter space. This leads to the increase of C_1 (the Berry phase, or the polarization) by one polarization quantum, consistent with the quantization of charge transport [93, 35].

The hopping part of the SSH Hamiltonian reads:

$$\hat{H}_{SSH} = -J \sum_{i=1}^{N/2} c_{i,A}^{\dagger} c_{i,B} - J' \sum_{i=1}^{N/2} c_{i,B}^{\dagger} c_{i+1,A} + \text{H.c.}, \tag{3.6}$$

where N denotes the number of sites, the on-site potential has the form

$$\hat{H}_{\Delta} = -\Delta \sum_{i=1}^{N/2} c_{i,A}^{\dagger} c_{i,A} + \Delta \sum_{i=1}^{N/2} c_{i,B}^{\dagger} c_{i,B}. \tag{3.7}$$

The model is shown schematically in Fig. 5.1. This figure shows the one-dimensional lattice, including sublattices, the alternating hoppings, and the on-site potential. The unit cell is indicated in shaded yellow. Also shown is the continuous variable x, which runs from $-\infty$ to ∞, and will serve as the axis for the reconstructed probability distributions of the polarization calculated below.

The hoppings can also be expressed in terms of the average hopping t and the deviation δ as

$$J = \frac{t}{2} + \frac{\delta}{2}, \quad J' = \frac{t}{2} - \frac{\delta}{2}. \tag{3.8}$$

The total Hamiltonian we consider is

$$\hat{H} = \hat{H}_{SSH} + \hat{H}_{\Delta}. \tag{3.9}$$

The parameters J and J' are hopping parameters corresponding to hopping along alternating bonds. We take the lattice constant to be unity (the unit cell is two

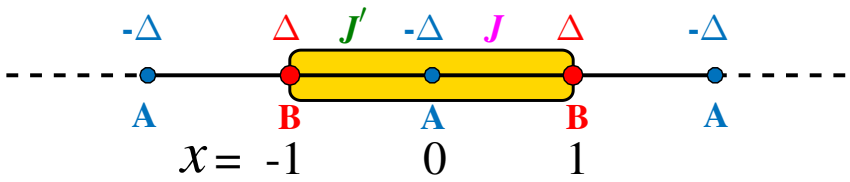

Figure 3.1: Schematic representation of the Rice-Mele model. Δ represents the on-site potential, A and B refer to the different sublattices. J and J' are the alternating hoppings. The unit cell is indicated in yellow. The x label corresponds to localization within the unit cell ($-1 < x < 1$). The variable x is continuous, below, in our subsequent calculations, the probability distribution will be shown as a function of x. The unit of x is the lattice constant.

lattice constants). The parameter Δ denotes the on-site potential, whose sign alternates from site to site. This model is metallic for $J = J'$ and $\Delta = 0$ but is insulating for all other values of the parameters. In reciprocal space this Hamiltonian becomes

$$\hat{H} = \sum_k \begin{pmatrix} \Delta & -\rho_k \\ -\rho_k^* & -\Delta, \end{pmatrix} \tag{3.10}$$

where

$$\rho_k = Je^{ik} + J'e^{-ik}. \tag{3.11}$$

At a particular value of k we can write the eigenstate for the lower band as

$$\begin{pmatrix} \alpha_k \\ \beta_k \end{pmatrix} = \begin{pmatrix} \sin\left(\frac{\theta_k}{2}\right) \\ e^{-i\phi_k}\cos\left(\frac{\theta_k}{2}\right) \end{pmatrix}, \tag{3.12}$$

where

$$\begin{aligned} \theta_k &= \arctan\left(\frac{|\rho_k|}{\Delta}\right) \\ \phi_k &= \arctan\left(\frac{(J-J')\sin(k)}{(J+J')\cos(k)}\right). \end{aligned} \tag{3.13}$$

The cumulants can now be written in terms of the eigenstates. For example,

$$C_1 = \frac{i}{\pi}\int_{-\pi/2}^{\pi/2} dk(\alpha_k^*\partial_k\alpha_k + \beta_k^*\partial_k\beta_k), \tag{3.14}$$

and the other cumulants can be constructed accordingly (note that the unit cell is $L = 2$).

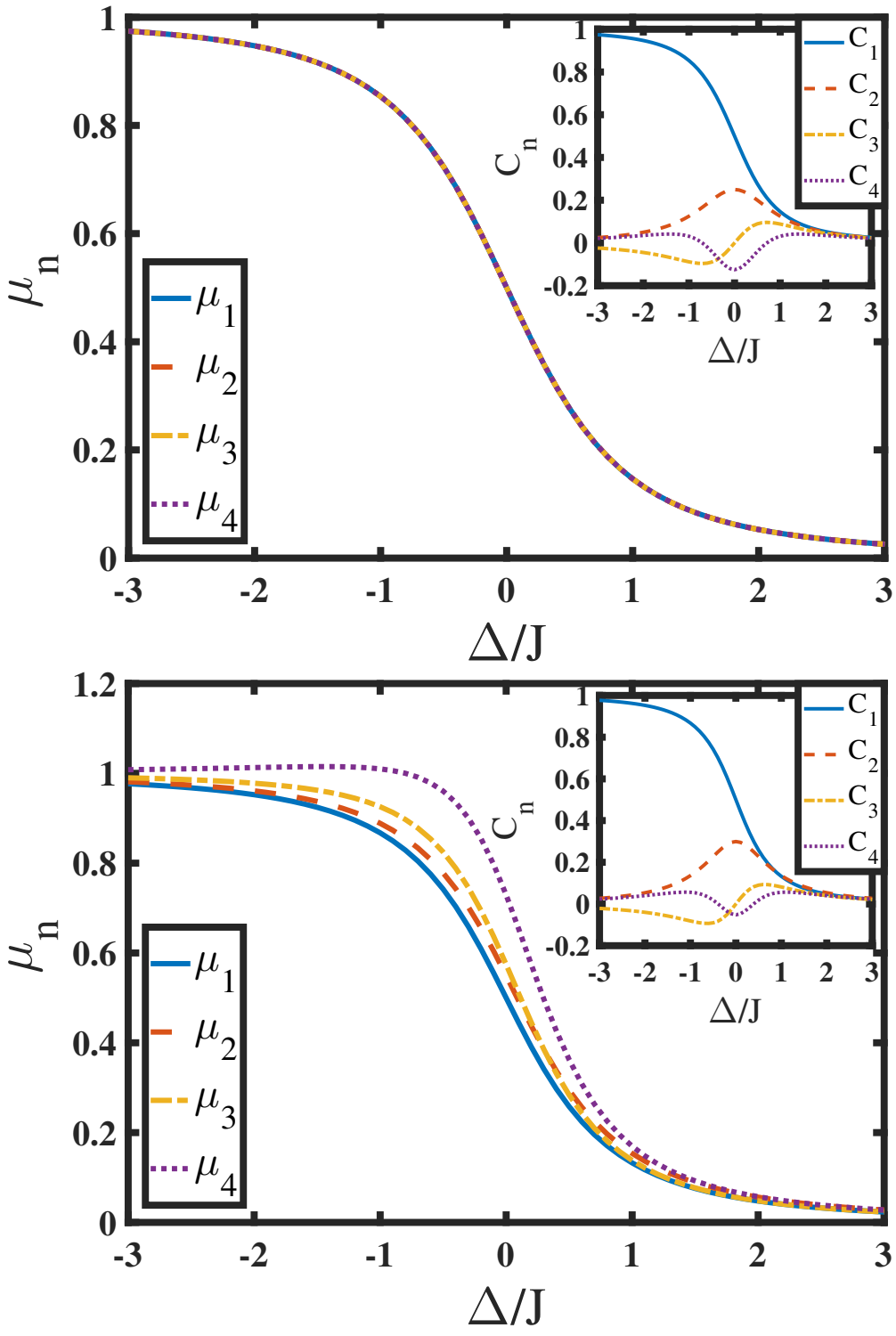

Figure 3.2: Moments for $J'/J = 0$ (upper panel) and 0.3 (lower panel) as a function of Δ/J. In these calculations $J = 1$. For $J'/J = 0$ the curves are identical. The insets show the corresponding cumulants.

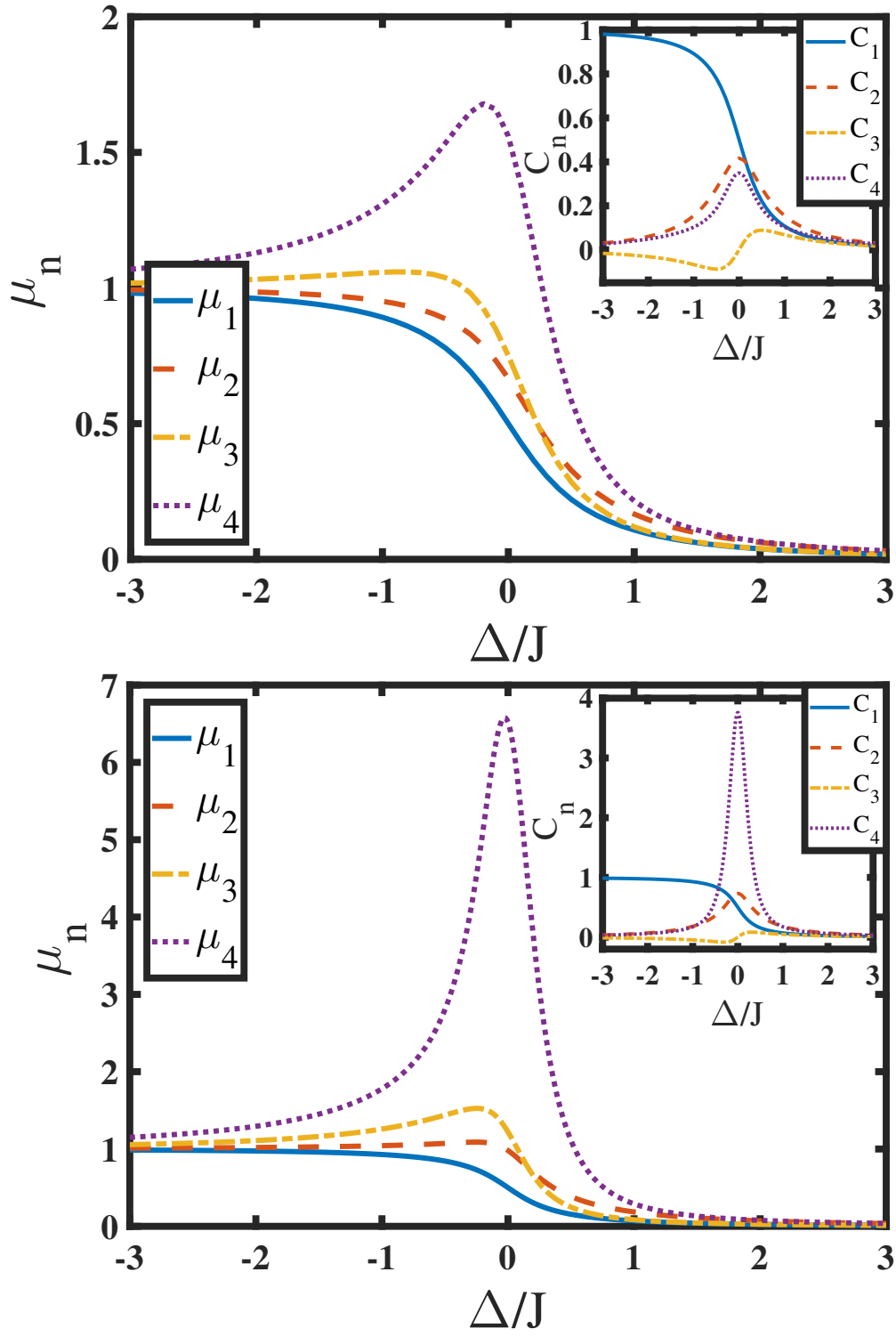

Figure 3.3: Moments for $J'/J = 0.5$ (upper panel) and 0.7 (lower panel) as a function of Δ/J. In these calculations $J = 1$. The insets show the corresponding cumulants.

3.2.1 Fully dimerized limit

Here we show that in the fully dimerized limit the GIMs should all have the same magnitude. In Ref. [39] and previous chapter we pointed out that the Berry phase can be related to an observable $\hat{O}$ fixed by requiring that

$$\partial_K H(K) = i[H(K), \hat{O}]. \tag{3.15}$$

This definition does not uniquely fix the operator $\hat{O}$. For example, for the magnetic field example the matrix $\sigma_z/2$ or $(\sigma_z + I)/2$ both satisfy Eq. (3.15). This arbitrariness causes a shift in the first cumulant. However, only the operator $(\sigma_z + I)/2$ will give a distribution in which all moments are equal, since this matrix has the form

$$(\sigma_z + I)/2 = \begin{pmatrix} 1 & 0 \\ 0 & 0 \end{pmatrix}, \tag{3.16}$$

and is equal to itself when raised to any power.

In the case of the RM model we first write the Hamiltonian with the parameter K explicitly as

$$\begin{aligned} \hat{H}(K) = \quad & -J \exp(iK) \textstyle\sum_{j=1}^{L/2} c_{j,A}^\dagger c_{j,B} + \text{H.c.} \\ & -J' \exp(iK) \textstyle\sum_{j=1}^{L/2} c_{j,B}^\dagger c_{j+1,A} + \text{H.c.} + \hat{H}_\Delta. \end{aligned} \tag{3.17}$$

The operator $\partial_K \hat{H}(K)$ is the current,

$$\begin{aligned} \partial_K \hat{H}(K) = \quad & -iJ \exp(iK) \textstyle\sum_{j=1}^{L/2} c_{j,A}^\dagger c_{j,B} + \text{H.c.} \\ & -iJ' \exp(iK) \textstyle\sum_{j=1}^{L/2} c_{j,B}^\dagger c_{j+1,A} + \text{H.c.}. \end{aligned} \tag{3.18}$$

We now write a form for the operator $\hat{O}$ as

$$\hat{O} = \sum_{j=1}^{L/2} x_j c_{j,A}^\dagger c_{j,A} + y_j c_{j,B}^\dagger c_{j,B}. \tag{3.19}$$

Evaluating the commutator gives

$$\begin{aligned} i[\hat{H}(K), \hat{O}] = & \, i \sum_{j=1}^{L/2} (y_j - x_j) J \exp(iK) c_{j,A}^\dagger c_{j,B} + \text{H.c.} \\ & i \sum_{j=1}^{L/2} (x_{j+1} - y_j) J' \exp(iK) c_{j+1,A}^\dagger c_{j,B} + \text{H.c.} \end{aligned} \tag{3.20}$$

For the case $J' = 0$ we can chose $x_j = 0$ and $y_j = 1$, so that $i[\hat{H}(K), \hat{O}]$ corresponds to the current. This is not the only choice, but with this choice the operator $\hat{O}$ when written in k-space corresponds to

$$\hat{O} = \sum_k (c^\dagger_{k,A} c^\dagger_{k,B}) \begin{pmatrix} 0 & 0 \\ 0 & 1 \end{pmatrix} \begin{pmatrix} c_{k,A} \\ c_{k,B} \end{pmatrix}, \tag{3.21}$$

which gives equal moments. Clearly, the choice for the spatial coefficients x_j and y_j are due to the fact that in this case the system consists of a set of independent dipoles. When J is taken to zero, and J' kept finite, then the appropriate choice to fix $\hat{O}$ is $x_j = 0$ and $y_j = -1$. If instead the sign of Δ is changed $\hat{O}$ is again defined by the $x_j = 0$ and $y_j = -1$. These results are clearly due to the reversal of the direction of the dipole moment within the unit cell. The results presented in Figs. 3.2 and 3.2 corroborate our derivation.

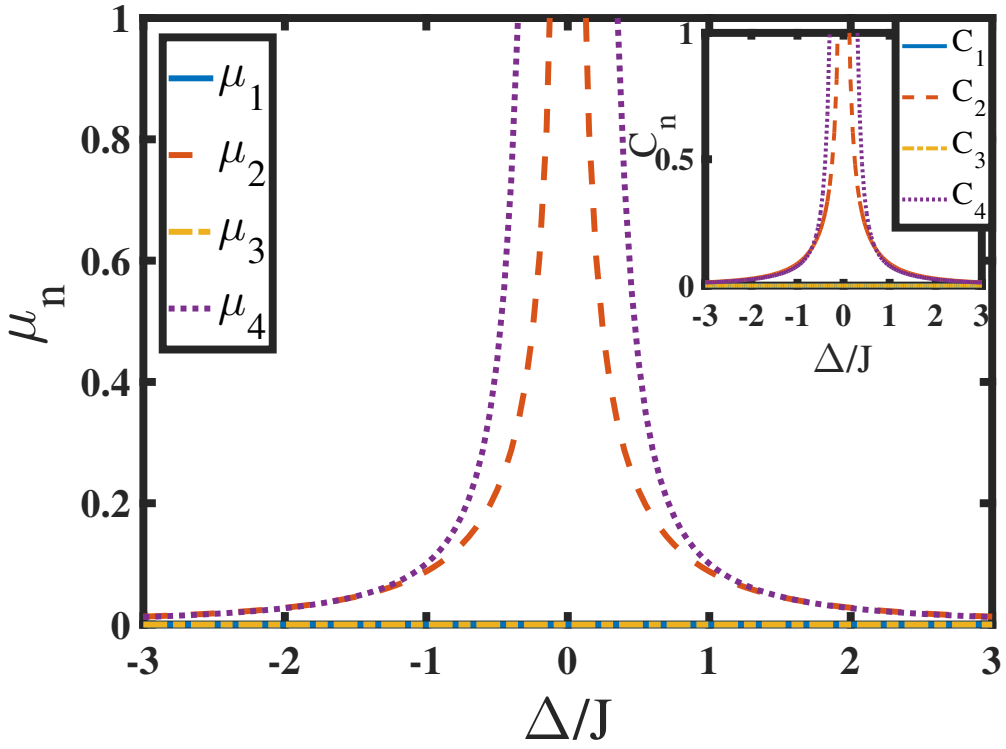

Figure 3.4: Moments for $J'/J = 1$ as a function of Δ/J. In these calculations $J = 1$. The inset shows the corresponding cumulants. In the limit $\Delta/J \to 0$ (the topological point of the model) the even cumulants diverge, while the odd cumulants are always zero for this case.

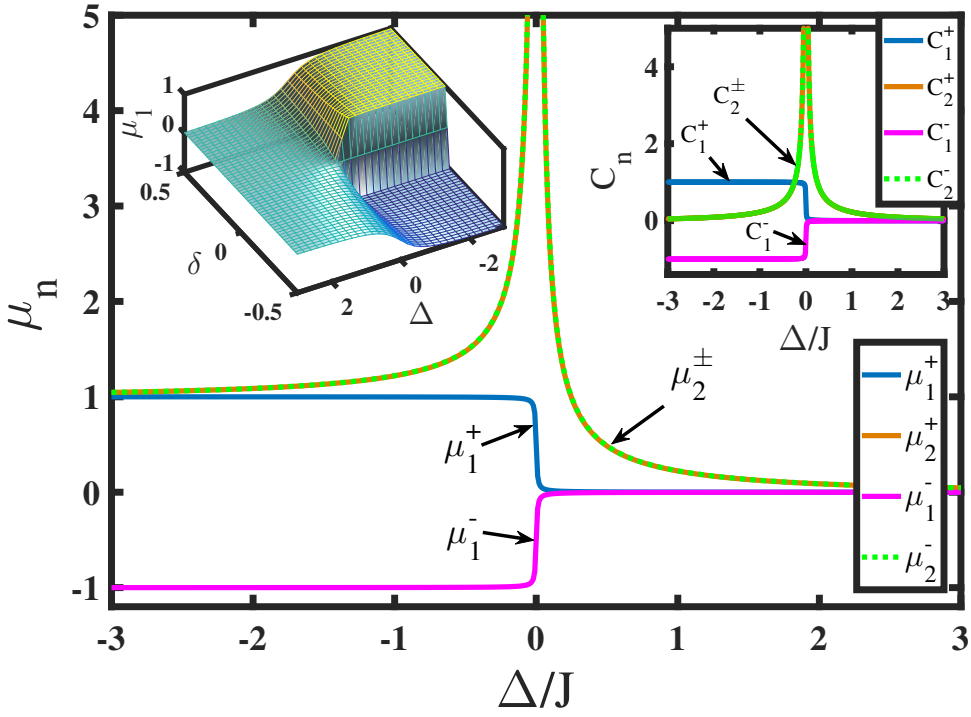

Figure 3.5: First two moments and cumulants (right inset) for $J = 1, J' = J \pm 0.006$. Left inset shows the first moment on the $\Delta - \delta$ plane, indicating the singular behavior along the line $\Delta < 0, \delta = 0$.

3.2.2 Results and analysis

We first look at the system with $J' = 0$. In this case, the band structure of the system is simply two flat lines in the Brillouin zone. The system can be thought of as a simple two-state system. We calculated the first four GICs, from which we obtained the corresponding GIMs. The results are shown in the uppermost panel of Figs. 3.2 and 3.3. The moments as a function of Δ/J all fall on the same curve in this case. If the hopping parameters J and J' are switched (not shown), the sign of the odd moments changes, the even moments remain the same. These results are in accordance with section 3.2.1.

Figs. 3.2 and 3.3 also shows the cumulants for different ratios; $J'/J = 0.3, 0.5, 0.7$. The deviation of the cumulants from one another is more pronounced, and increases with an increase of J'/J. However, the moments become equal for

any J'/J when $\Delta \to \pm\infty$. In this case also, the system becomes an independent array of two state systems. The band energies in all these cases vary continuously with k across the Brillouin zone.

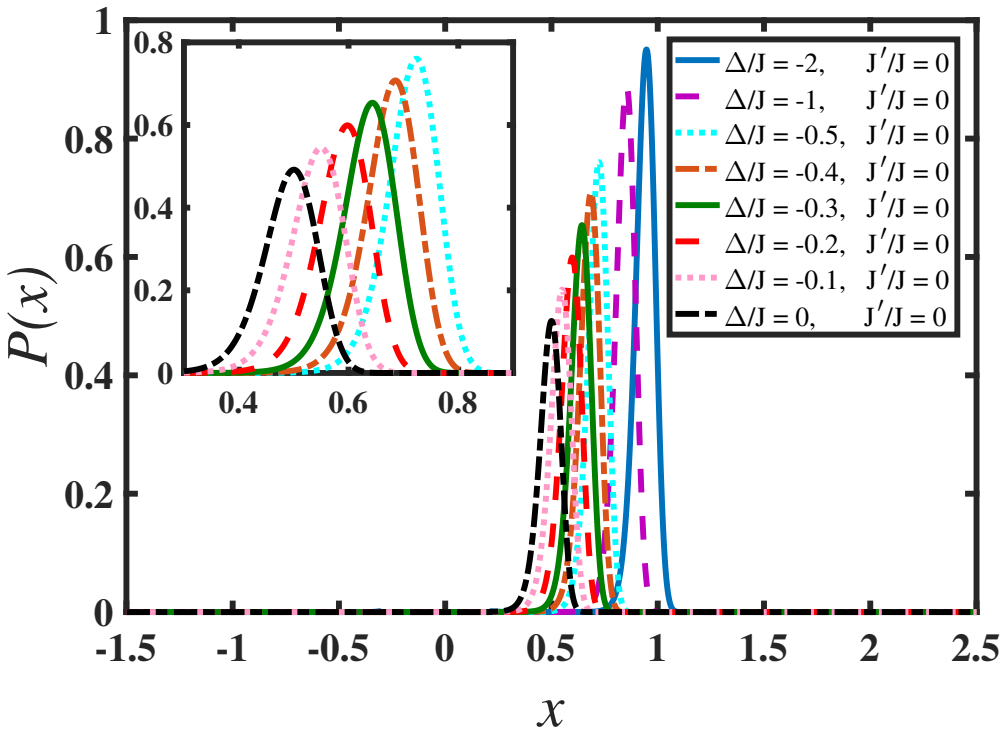

Figure 3.6: Normalized probability distribution of the polarization for different parameters of the Rice-Mele Hamiltonian. In these calculations $J = 1$. The unit of length in these figures is the lattice constant. Different values of Δ/J are shown for $J'/J = 0.0$. In the topmost panel ($J'/J = 0$) the inset shows the distribution for the cases $\Delta/J = 0.0, -0.1, -0.2, -0.3, -0.4, -0.5$)

The results for the case $J'/J = 1$ are also shown separately in Fig. 3.4, as well as the limits $J' \to_{\pm} J$. For finite Δ/J the odd cumulants are zero, indicating an even probability distribution. The ratio of the second and fourth cumulants rule out a Gaussian. As $\Delta/J \to 0$ a discontinuity in the slope of the band develops. In this case, the cumulants C_2 and C_4 diverge. Figure 3.5 shows what happens when J' is close to J (bigger or smaller) but the two are not quite equal ($J' = J + \epsilon$, ϵ a small number). We see that in this case the first moment is one or minus one, depending on the sign of ϵ, and zero is not approached as $\epsilon \to 0$ from either side. The left inset in the lower panel shows the behavior of the first moment on the

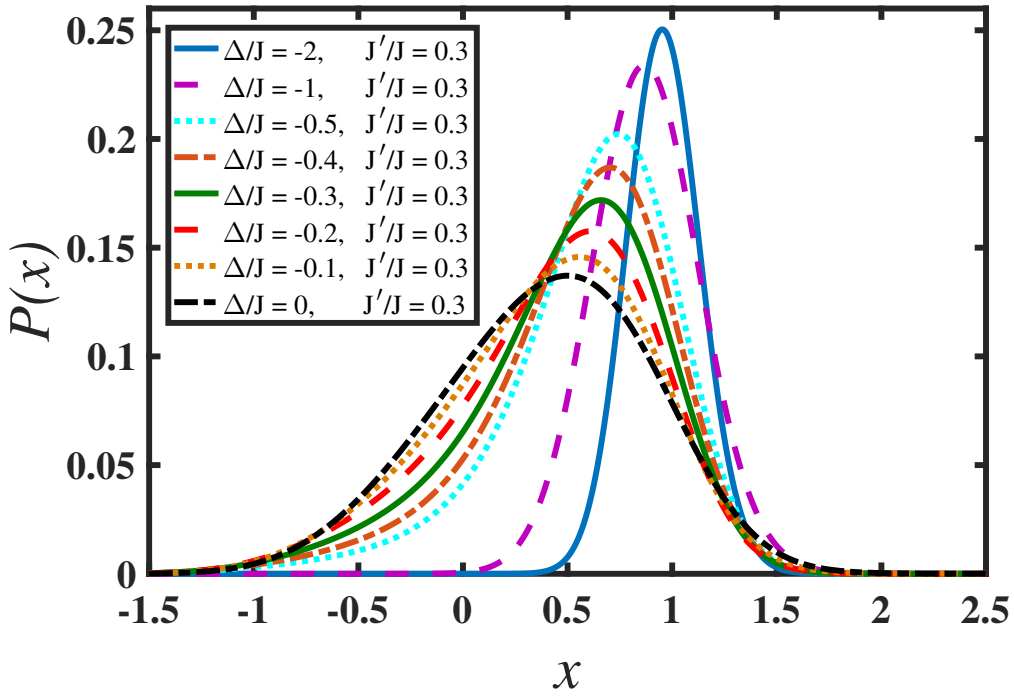

Figure 3.7: Normalized probability distribution of the polarization for different parameters of the Rice-Mele Hamiltonian. In these calculations $J = 1$. The unit of length in these figures is the lattice constant. Different values of Δ/J are shown for $J'/J = 0.3$. In the topmost panel ($J'/J = 0$) the inset shows the distribution for the cases $\Delta/J = 0.0, -0.1, -0.2, -0.3, -0.4, -0.5$)

$\Delta - \delta$ plane, indicating a discontinuity along the line $\Delta < 0, \delta = 0$ (the well-known result of Vanderbilt and King-Smith [91, 90]). The moments and cumulants we find are consistent with the behavior shown in the left inset of the lower panel of the figure.

In Figs. 3.6, 3.7, 3.8, and 3.9 we show examples of reconstructed probability distributions for $J'/J = 0.0, 0.3, 0.5, 0.7$, in each case for several values of Δ/J. χ^2 (defined in Eq. (3.5)) is tabulated in the appendix (Table A.1). The most localized example ($J'/J = 0$ and $\Delta/J = -2$) shows a sharp peak around $x = 1$; as Δ decreases the curves shift to the left and spread out, but their shape is always very similar (for smaller values of Δ/J this is emphasized in the inset). The maximum of the probability distribution is always between zero and one. These curves are all cases for which all the moments are equal. As the alternate hoppings

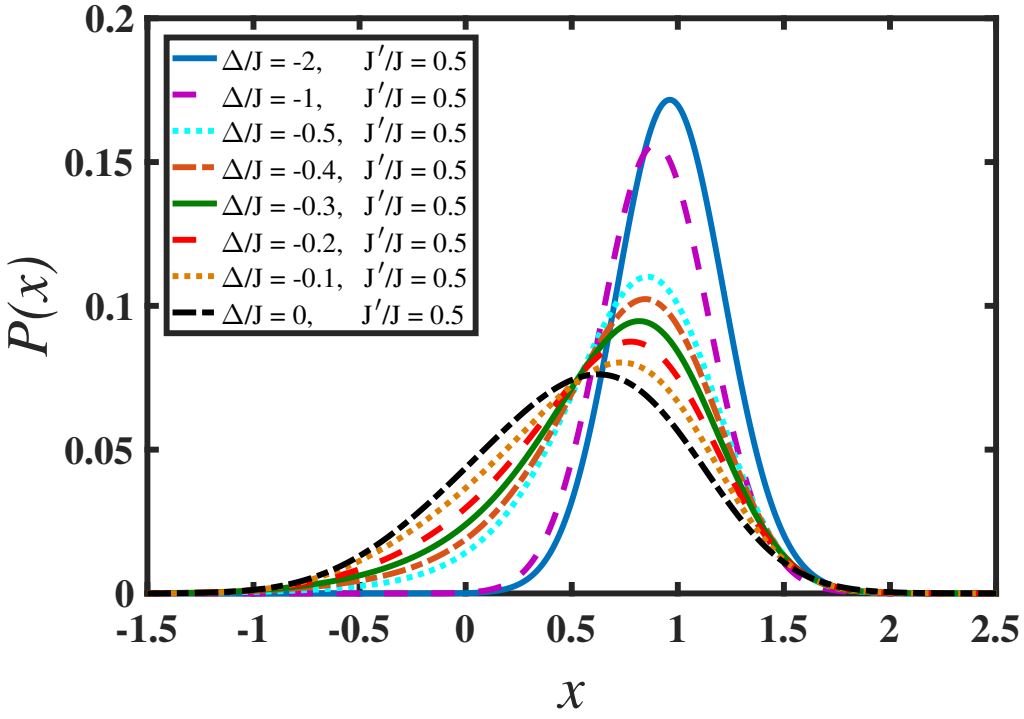

Figure 3.8: Normalized probability distribution of the polarization for different parameters of the Rice-Mele Hamiltonian. In these calculations $J = 1$. The unit of length in these figures is the lattice constant. Different values of Δ/J are shown for $J'/J = 0.5$. In the topmost panel ($J'/J = 0$) the inset shows the distribution for the cases $\Delta/J = 0.0, -0.1, -0.2, -0.3, -0.4, -0.5$)

(J') are turned on, the shifting occurs in a qualitatively different manner. Initially ($\Delta/J = -2$ in all cases) the curves are centered very near $x = 1$. $\Delta/J = -2$ is for most cases well in the region where the moments are equal. As Δ decreases, the distributions shift, but they do this by becoming asymmetric about their mean, with the density increasing on the side left of the maxima of the distributions. The shape of the distributions changes considerably. This is clearly due to the fact that in these latter cases the moments vary as Δ is varied, and they are not all equal. The maxima for the cases for which $J'/J \neq 0$ shift much less as Δ/J is varied. When Δ/J changes sign (results not shown), the polarization becomes centered around $x = 0$ end of the unit cell and the probability distributions are reflections of the ones shown in Figs. 3.6, 3.7, 3.8, and 3.9 across $x = 1/2$.

The probability distributions for the case $J' = J = 1$ are also shown separately

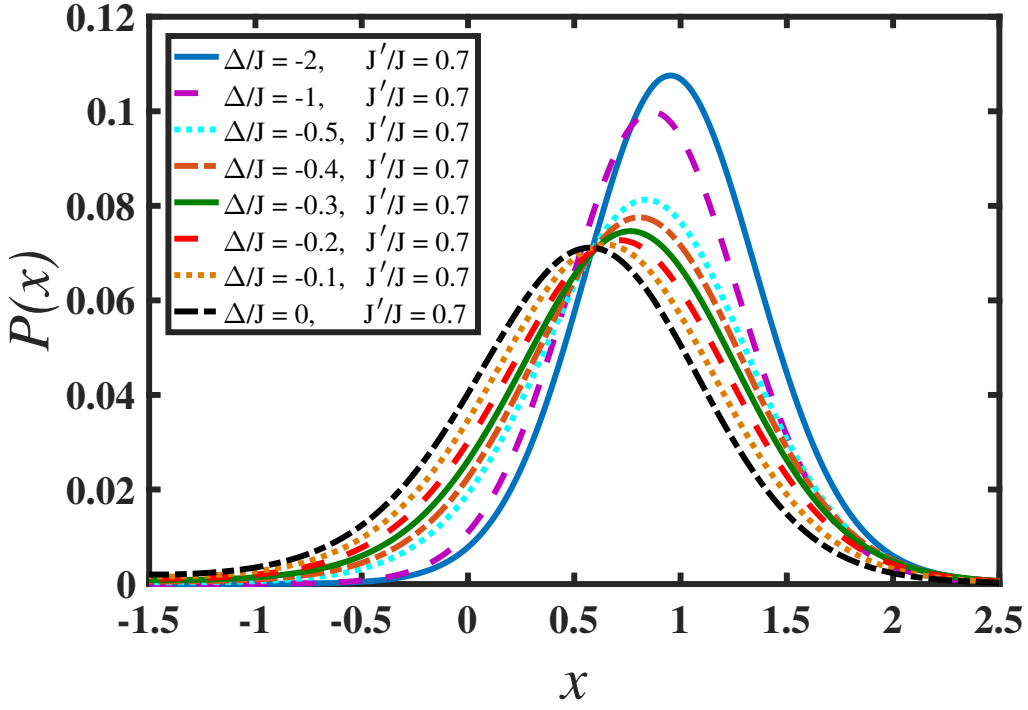

Figure 3.9: Normalized probability distribution of the polarization for different parameters of the Rice-Mele Hamiltonian. In these calculations $J = 1$. The unit of length in these figures is the lattice constant. Different values of Δ/J are shown for $J'/J = 0.7$. In the topmost panel ($J'/J = 0$) the inset shows the distribution for the cases $\Delta/J = 0.0, -0.1, -0.2, -0.3, -0.4, -0.5$)

in Fig. 3.10 (with χ^2 tabulated in Table A.1), as well as the case J' close to J. All of the $J' = J$ distributions are symmetric around the origin. As $\Delta/J \to 0$ the distribution broadens, and it is clear that a conducting phase is approached [44]. If $\Delta < 0$ then the polarizations are localized near $x = \pm 1$ depending on whether J' is smaller or larger than J. This is consistent with Figs. 3.4, and 3.5.

In Figs. 3.11 and 3.12 we show the evolution of the reconstructed probability distributions along two cyclic paths which encircle the topologically non-trivial point of the RM model, one with radius unity, the other with radius 0.2 in the Δ/t, δ/t plane. In these calculations the parametrization was different from the previous ones, here t was set to unity, rather than J (see Eq. (3.8)). For the points A^*, B, ... in Figs. 3.11 and 3.12 the values of Δ/J and J'/J are shown in Table A.2. The upper panel in both figures show the evolution of

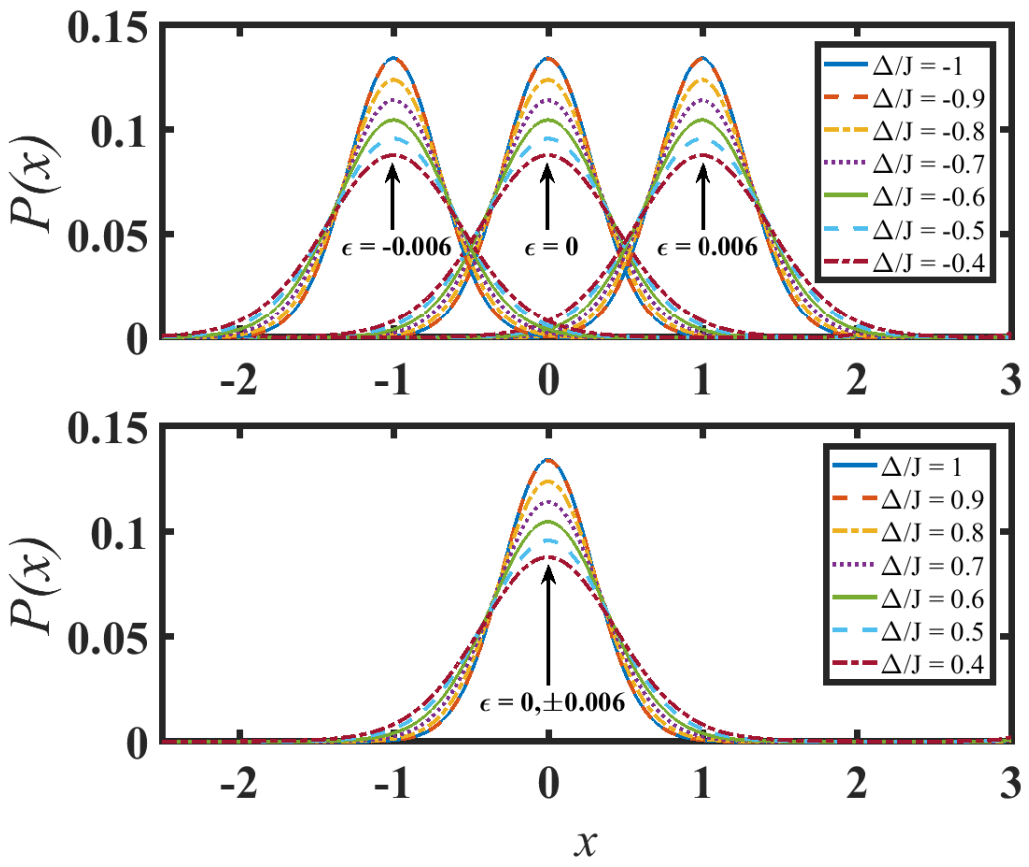

Figure 3.10: Normalized probability distribution of the polarization for cases $J' = J$ and $J' = J \pm \epsilon$ ($\epsilon = 0.006$). In these calculations $J = 1$. The unit of length is the lattice constant. Different values of Δ/J are shown. Upper panel(lower panel): $\Delta/J < 0$ ($\Delta/J > 0$).

the different GIMs(GICs). The even moments are single-valued, the odd ones are not. This follows from gauge invariance properties of the cumulants (Eq. (2.8)). The first cumulant is only gauge invariant modulo 2π times an integer [91, 90], the others do not change at all due to a gauge transformation. The odd GIMs depend on combinations of the GICs which involve odd combinations of the cumulants, therefore they are not multivalued in general. In both sets of figures (3.11 and 3.12) the points A^* are not exactly on the $\phi = -\pi/2$ axis, but instead we numerically realize the limit $\phi = \lim_{\delta\Phi\to 0^+}(-\pi/2 + \delta\Phi)$. In the actual calculation we took $\delta\Phi = 2\pi/1000$. Also, the point $\phi = -\pi/2$ or $\phi = 3\pi/2$ is excluded from the curves shown in the upper panels of the two figures.

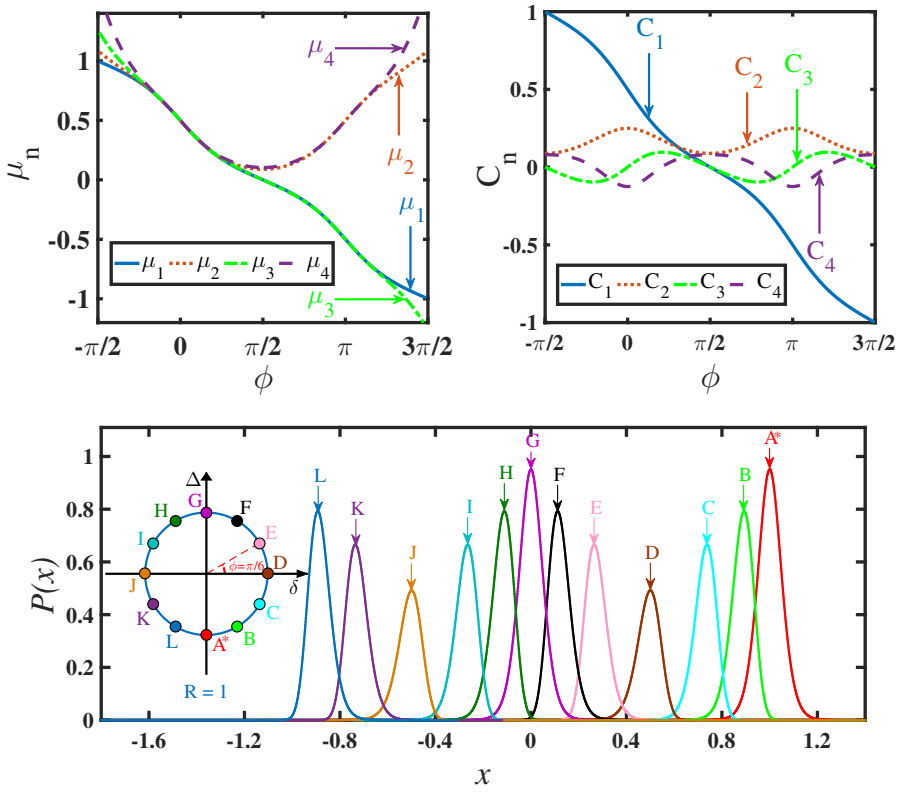

Figure 3.11: Moments, cumulants, and probability distribution along a circle of radius 1 in the Δ/t vs. δ/t plane. In these calculations $t = 1$. The path encircles the topological point $\Delta/t = 0, \delta/t = 0$. The top panels shows the gauge invariant moments and cumulants along the circle as a function of angle. The lower panel follows the evolution of the probability distribution. The point A^* is at an angle $\phi = -\pi/2 + 2\pi/1000$, not $\phi = -\pi/2$. In the lower panel the unit of x is the lattice constant. The points $\phi = -\pi/2, 3\pi/2$ are excluded from the curves shown in the upper panels.

The example with radius unity (Fig. 3.11) remains mostly in the fully dimerized limit, as can be seen in the upper panel of the figure. The odd moments and even moments are always equal. Except for a small region near $\phi/\pi = 0.5$ the absolute values of the moments are equal. The lower panel shows the evolution of the probability distribution along the path. Starting from a relatively sharp distribution localized near $x = 1$, the maximum moves to the left. Before reaching half the unit cell, the distribution spreads. After passing through the midpoint the system, where the maximum is the smallest, the distribution begins to localize again until $x = 0$. From there this tendency is repeated. Indeed, the distribution ends up at $x = -1$ at the end of the process: the Wannier function

"walked" to an equivalent position in the next unit cell. For the case of the smaller radius (0.2, Fig. 3.11) the initial distribution is broader, and as the cycle is traversed, the maximum of the distribution oscillates with a smaller amplitude, but the "walking" to a new equivalent position still occurs.

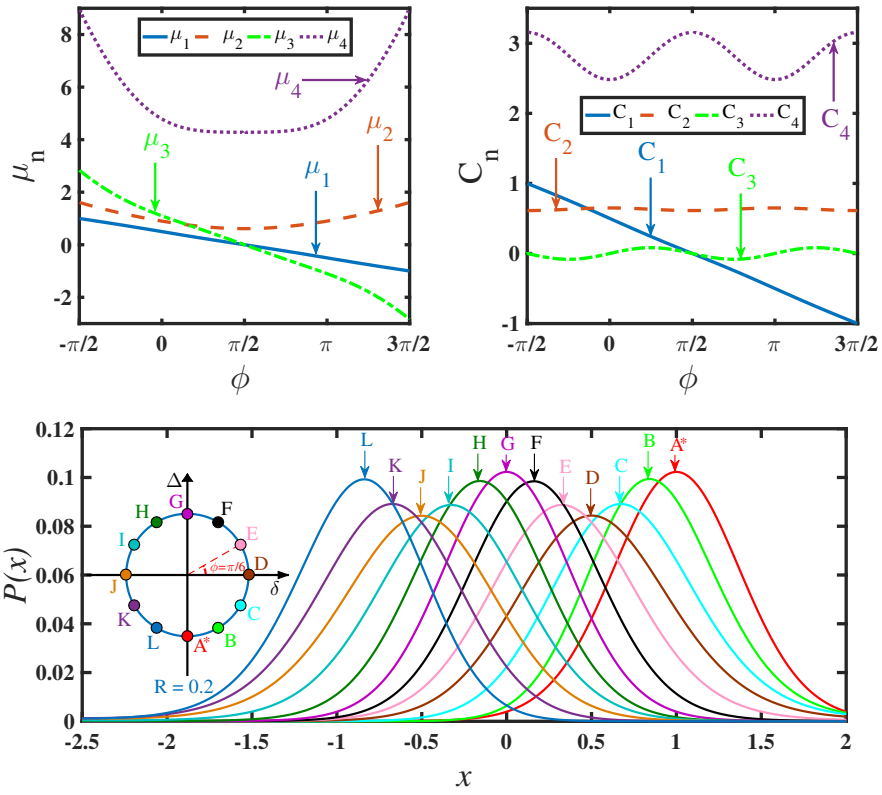

Figure 3.12: Moments, cumulants, and probability distribution along a circle of radius 0.2 in the Δ/t vs. δ/t plane. In these calculations $t = 1$. The path encircles the topological point $\Delta/t = 0, \delta/t = 0$. The upper panel shows the gauge invariant moments and cumulants along the circle as a function of angle. The top panels shows the gauge invariant moments and cumulants along the circle as a function of angle. The lower panel follows the evolution of the probability distribution. The point A^* is at an angle $\phi = -\pi/2 + 2\pi/1000$, not $\phi = -\pi/2$. In the lower panel the unit of x is the lattice constant. The points $\phi = -\pi/2, 3\pi/2$ are excluded from the curves shown in the upper panels.

In both Figs. 3.11 and 3.12 it is clear that the odd moments do not correspond to single-valued functions. The values of the odd moments depend on whether we

approach the original point from which the cycle begins ($\delta = 0, \Delta < 0$) from the left or the right. At the same time, the probability distributions for some cases with $\delta = 0, \Delta < 0$ are shown in Fig. 3.10; they are centered around zero and they spread as Δ/J is decreased. This suggests the limiting cases from either direction give different results from the result for fixing the Hamiltonian parameters such that $\delta = 0, \Delta < 0$.

3.3 Interacting Su-Schrieffer-Heeger model

We study the interacting SSH model in one dimension at half filling. This model consists of a hopping parameter, which alternates between odd and even bonds, and an interaction term if two particles are on nearest neighboring (NN) sites. For the case of uniform hopping for all bonds, the model can be solved by the Bethe ansatz, and it is known that an ideal conductor (finite Drude weight) to insulator phase transition takes place [105].

The Hamilton operator of the model consists of two terms, the SSH term ($\hat{h}_{SSH}$) and the interaction term ($\hat{h}_V$) and can be written as

$$\hat{H} = \overbrace{-\frac{1}{2}\sum_{n=1}^{L}[t + (-1)^n\delta]c_n^\dagger c_{n+1} + \text{H.c.}}^{\hat{h}_{SSH}} + \overbrace{\frac{V}{2}\sum_{n=1}^{L} n_n n_{n+1}}^{\hat{h}_V}. \tag{3.22}$$

where $c_n^\dagger$ (c_n) creates (annihilates) a particle at site n, $n_n = c_n^\dagger c_n$ is the density operator at site n. t denotes the average hopping, taken as unity in the following, δ denotes the deviation in hopping between odd and even sites. V is the Couloumb interaction between NNs. For $\delta = 0$ the ideal conductor insulator transition occurs at $V = 2$ in units of t. In the rest of the thesis we use units of t. Figure (3.13) illustrates the model and the meaning of the different parameters.

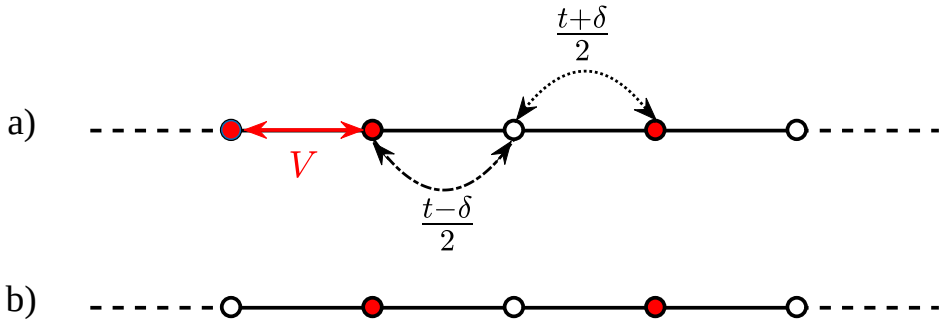

Figure 3.13: Graphical representation of our model Hamiltonian (part a)) and the charge density wave (CDW) state (part b)). Filled(Empty) circles indicate lattice sites occupied(not occupied) by particles. In part a) V indicates the interaction, t indicates the average hopping, δ denotes the amount by which the hopping alternates between even and odd bonds.

3.3.1 The Baeriswyl variational wave function

The BWF [61, 95, 106, 107] already has a history of successfully reproducing the properties of strongly correlated models. It was originally developed for the fermionic Hubbard model, but it has been applied to the bosonic Hubbard [65] as well as quenches interacting spinless fermions [66].

In this section we describe the BWF [61, 95], its extensions necessary to account for the alternating hoppings of the SSH model, and write down the solution for the variational energy in closed form.

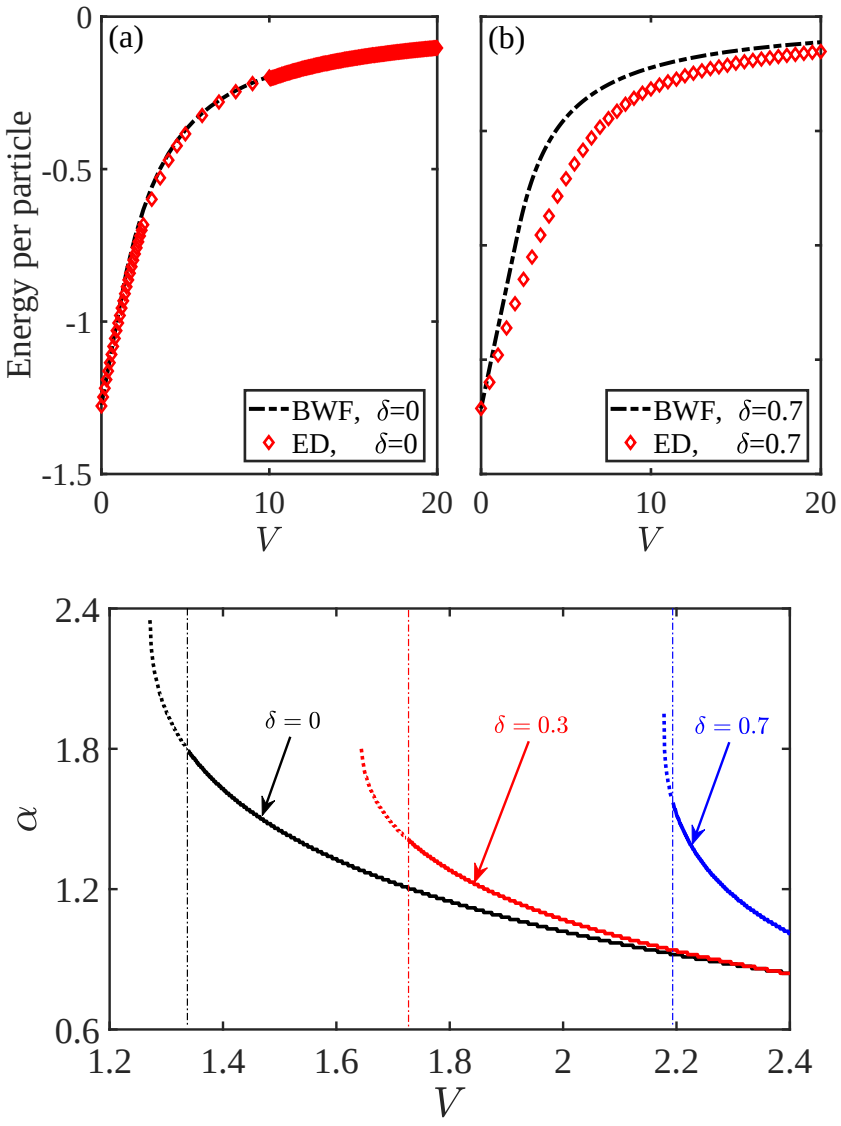

Figure 3.14: Upper panel: The variational ground state energy per particle for (a) $\delta = 0$, and (b) $\delta = 0.7$ based on the Baeriswyl wave function compared to exact diagonalization for 12 lattice sites . Lower panel: the variational parameter as a function of interaction strength for $\delta = 0, \pm 0.3$ and ± 0.7. Solid lines indicate the global minimum in the CDW type insulating phase. Dashed lines indicate metastable insulating phases on the metallic side of the phase diagram.

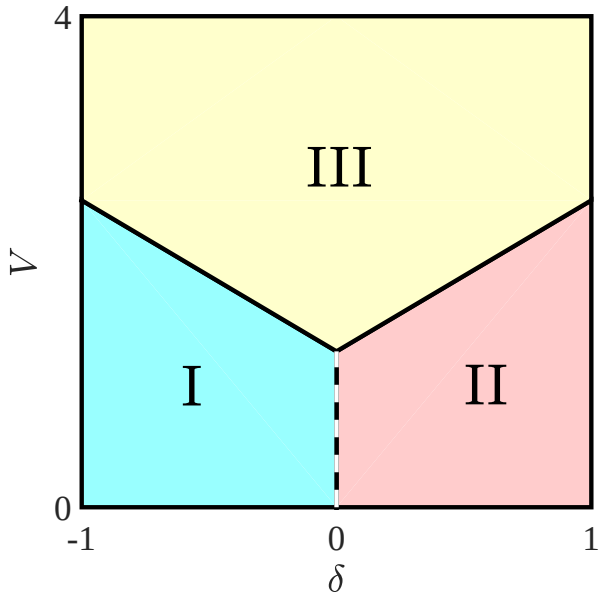

Figure 3.15: Phase diagram. I and II are SSH states (Hartree-Fock approximation). III is a CDW type phase, with finite skew when δ differs from zero. The dashed line indicates a Fermi sea (ideal conductor).

The BWF starts with the wave function at infinite interaction (a charge-density wave) and acts on this wave function with a kinetic energy based projector. In analogy to this idea we write [108]

$$|\Psi_B(\alpha)\rangle = N_B \exp(-\alpha \hat{h}_{SSH})|\Psi_\infty\rangle, \tag{3.23}$$

where α denotes the variational parameter and $|\Psi_\infty\rangle$ stands for a perfectly ordered charge density wave, and N_B is a normalization constant. Our further calculations are rendered easier by the particularly simple form of $|\Psi_\infty\rangle$,

$$|\Psi_\infty\rangle = \prod_{k \epsilon RBZ} \frac{1}{\sqrt{2}}(c_k^\dagger + c_{k+Q}^\dagger)|0\rangle \tag{3.24}$$

where $Q = \pi$ is ordering wave vector (the lattice constant was assumed to be unity), the product runs through the reduced Brillouin zone (RBZ) and $|0\rangle$ is

fermionic vacuum state. Fourier transforming the Hamiltonian results in,

$$\hat{h}_{SSH}(k) = \begin{bmatrix} c_k^\dagger & c_{k+\pi}^\dagger \end{bmatrix} \begin{bmatrix} \epsilon(k) & i\gamma(k) \\ -i\gamma(k) & -\epsilon(k) \end{bmatrix} \begin{bmatrix} c_k \\ c_{k+\pi} \end{bmatrix} \tag{3.25}$$

$$\hat{h}_V = -\frac{V}{L} \sum_{k,k',q} \epsilon(q) c_{k+q}^\dagger c_k c_{k'-q}^\dagger c_{k'} \tag{3.26}$$

where $\epsilon(k) = -t\cos k, \gamma(k) = -\delta \sin k$. With the help of the Pauli matrix representation of the SSH noninteracting Hamiltonian,

$$\hat{h}_{SSH}(k) = \epsilon(k)\sigma_z - \gamma(k)\sigma_y \tag{3.27}$$

the SSH Hamiltonian based projector can be expanded as

$$\exp(-\alpha \hat{h}_{SSH}(k)) = \cosh(\alpha h(k))\hat{\hat{I}} - \sinh(\alpha h(k))\hat{\hat{h}}_{SSH}(k) \tag{3.28}$$

where $h(k) = \sqrt{t^2 \cos^2 k + \delta^2 \sin^2 k}$, $\hat{\hat{I}}$ is the 2-by-2 identity matrix, and

$$\hat{\hat{h}}_{SSH}(k) = \frac{\hat{h}_{SSH}(k)}{h(k)}, \tag{3.29}$$

a unit vector in the space spanned by $\epsilon(k)$ and $\gamma(k)$. Now, applying the projector (3.28) on the CDW state (Eq. (3.24)) we obtain the normalized wave function,

$$|\Psi_B(\alpha)\rangle = \prod_{k \epsilon RBZ} \frac{A(k)c_k^\dagger + A(k+Q)c_{k+Q}^\dagger}{\sqrt{2\cosh\left[2\alpha h(k)\right]}} |0\rangle, \tag{3.30}$$

with

$$A(k) = \cosh\left[\alpha h(k)\right] - \frac{\sinh\left[\alpha h(k)\right]}{h(k)}\epsilon(k) + i\gamma(k)\frac{\sinh\left[\alpha h(k)\right]}{h(k)}. \tag{3.31}$$

Having derived the action of the projector on the CDW state, we can now evaluate the variational estimate for the ground state energy by calculating the expectation value of Eq. (3.25) over our extended Baeriswyl wave function. We give the expectation values of the SSH Hamiltonian and of the interaction separately as

$$\langle \hat{h}_{SSH} \rangle = -\sum_k h(k) \tanh\left[2\alpha h(k)\right] \tag{3.32}$$

and

$$\langle \hat{h}_V \rangle = \frac{VL}{4} - \frac{V}{L} \sum_{i=1}^{3} |T_i|^2 \tag{3.33}$$

where

$$T_1 = \sum_k \left[\frac{1}{2\cosh\left[2\alpha h(k)\right]} + \frac{i\gamma(k)}{2h(k)} \tanh\left[2\alpha h(k)\right] \right] \tag{3.34}$$

$$T_2 = \sum_k \left[\frac{\epsilon(k)}{2} - \frac{\epsilon(k)^2}{2h(k)} \tanh\left[2\alpha h(k)\right] \right]$$

$$T_3 = \sum_k \left[\frac{\epsilon(k)}{2\cosh\left[2\alpha h(k)\right]} + \frac{i\epsilon(k)\gamma(k)}{2h(k)} \tanh\left[2\alpha h(k)\right] \right].$$

For the $t-V$ model these expressions were derived in Ref. [66].

We obtain the normalized wave function,

$$|\Psi_B(\alpha)\rangle = \prod_{k\epsilon RBZ} \frac{A(k)c_k^\dagger + A(k+Q)c_{k+Q}^\dagger}{\sqrt{2\cosh\left[2\alpha h(k)\right]}} |0\rangle, \tag{3.35}$$

with

$$A(k) = \cosh\left[\alpha h(k)\right] - \frac{\sinh\left[\alpha h(k)\right]}{h(k)} \epsilon(k) + i\gamma(k) \frac{\sinh\left[\alpha h(k)\right]}{h(k)}. \tag{3.36}$$

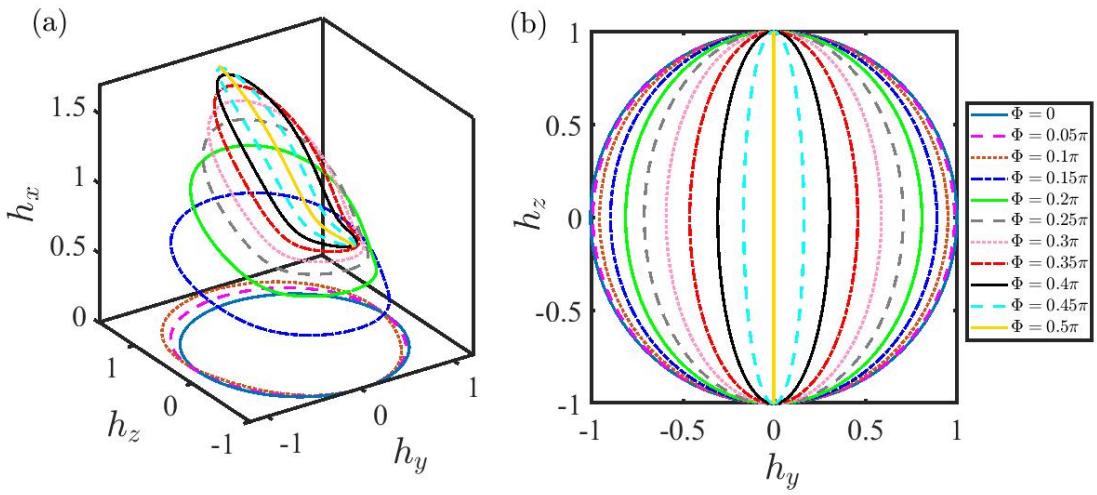

Figure 3.16: Curves traced out by the Hamiltonian in the Brillouin zone. Left panel shows the correlated system, $\delta = \cos(\phi), V = 1 + 4\sin(\phi)$. On the right panel $\delta = \cos(\phi), V = 1$. For both panels, the values of the variable ϕ are indicated in the legend on the right.

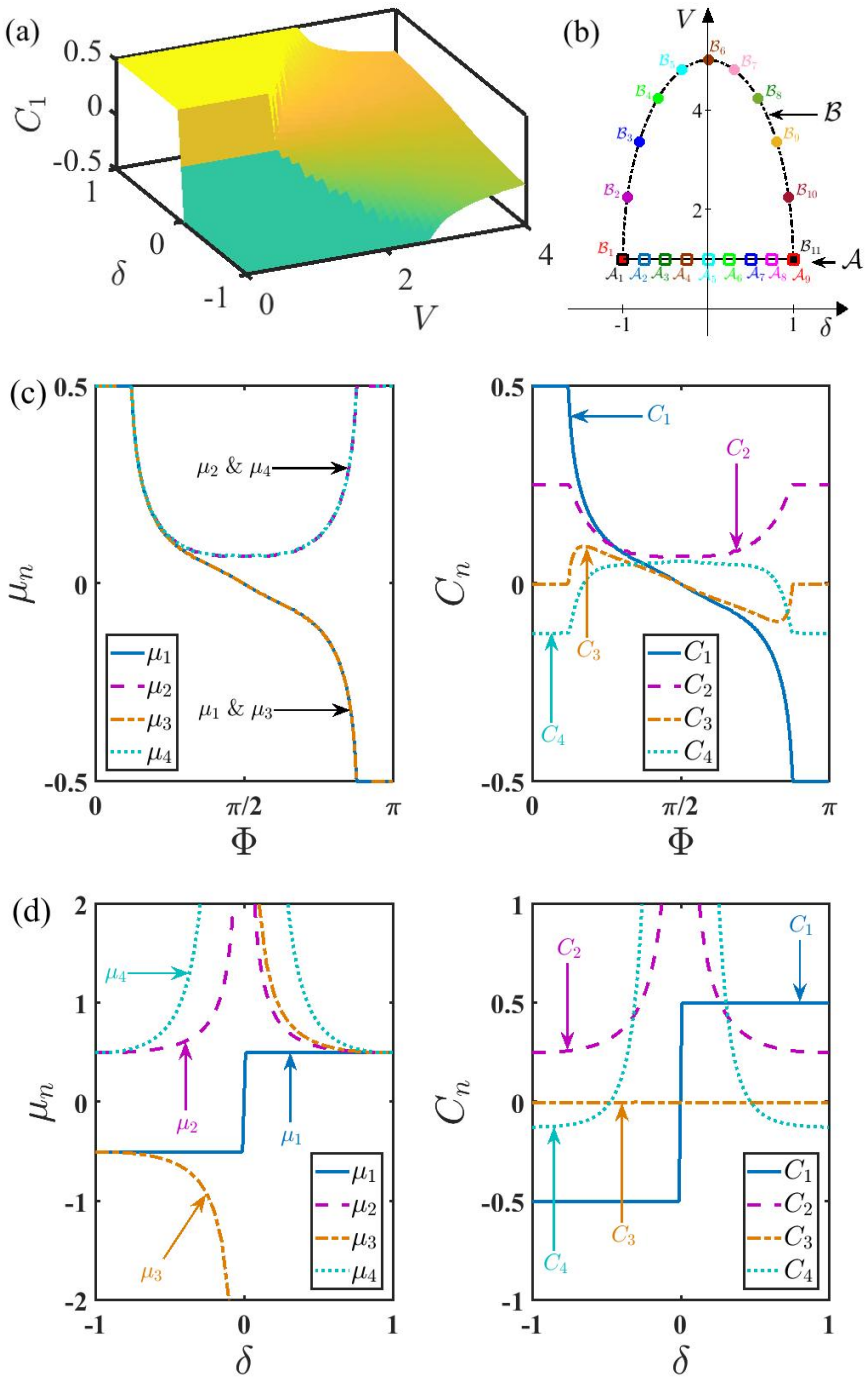

Figure 3.17: (a) First cumulant, (C_1) or polarization, of the interacing Su-Schrieffer-Heeger model as a function of δ and V. (b) Lines in the $\delta - V$ plane for which we calculate the cumulants and reconstruct the polarization. Two paths are shown between the points $-1, 1$ and $1, 1$: path $\mathcal{A}$ is a straight line, path $\mathcal{B}$ is a semi-ellipse. (c) Moments and cumulants along the semi-elliptic ($\mathcal{B}$) path. (d) Moments and cumulants along the straight line ($\mathcal{A}$) path.

This newly derived wave function gives exact results in two extreme limits, $V \to 0$ and $V \to \infty$. In the former the total energy becomes equal to the energy of the SSH model, while in the latter the total energy tends to zero. In between these two opposite extreme limits a comparison of numerically calculated total energy with exact diagonalized calculation and optimal minimization parameter is given in the upper panel of Fig. 3.14 for a small sized system. The extended BWF gives results which compare well in all cases, although as δ increases, the agreement worsens.

3.3.2 Parent Hamiltonian of the Baeriswyl wave function

Visualizing topological phase transitions is greatly aided in the case of Hamiltonians which are two-state in k-space via plotting the curves traced out by sweeping through the Brillouin zone [109]. The standard way is to write the two-state Hamiltonian in the form $H(k) = \mathbf{h}(k) \cdot \sigma$, where $\mathbf{h}(k)$ is a three-dimensional vector which traces out a closed curve in the space spanned by $h_x(k)$, $h_y(k)$, $h_z(k)$.

We can use the results of the previous subsection to construct an effective parent Hamiltonian for the BWF, which is also of the form $H(k) = \mathbf{h}(k) \cdot \sigma$. Our construction consists of two steps. First, inspecting Eqs. (3.32)-(3.34), we are able to write the total energy (apart from the constant shift $VL/4$) as a *single* sum over k, as $E = \sum_k \tilde{\epsilon}_k$. Since Eqs. (3.34) include double k-sums, these contributions to $\tilde{\epsilon}(k)$ appear as single k-sums. Second, we consider the coefficients at k and $k+Q$, and obtain the angles θ_k and ϕ_k according to the normalized equation

$$\tilde{\epsilon}_k \begin{bmatrix} \cos(\theta_k) & \sin(\theta_k)e^{-i\phi_k} \\ \sin(\theta_k)e^{i\phi_k} & -\cos(\theta_k) \end{bmatrix} \begin{bmatrix} \frac{\sin(\theta_k)}{2} \\ -\frac{\cos(\theta_k)}{2}e^{i\phi_k} \end{bmatrix} = -\tilde{\epsilon}_k \begin{bmatrix} \frac{\sin(\theta_k)}{2} \\ -\frac{\cos(\theta_k)}{2}e^{i\phi_k} \end{bmatrix},$$

where we equate

$$\begin{aligned} \frac{A(k)}{\sqrt{2\cosh\left[2\alpha h(k)\right]}} &= \frac{\sin(\theta_k)}{2} \\ \frac{A(k+Q)}{\sqrt{2\cosh\left[2\alpha h(k)\right]}} &= -\frac{\cos(\theta_k)}{2}e^{i\phi_k}. \end{aligned} \tag{3.37}$$

This procedure guarantees that summing over the RBZ gives the correct ground state energy, and that at each k-vector, the correct coefficients $A(k)$ and $A(k+Q)$ are obtained.

3.3.3 Polarization and gauge invariant cumulants

Here we give the basic expressions for the gauge invariant cumulants, for the reconstruction of the polarization we refer the reader to Chapter 2 or Ref. [40].

In our model the wave function is of the form given in Eq. (3.35). The cumulants can be obtained in a straightforward way, for example,

$$\gamma_m(k) = A^*(k)\partial_k^m A(k) + A^*(k+Q)\partial_k^m A(k+Q). \tag{3.38}$$

Using $\gamma_m(k)$ the cumulants can be constructed according to Eq. (2.8), however the integrals and the normalization are now over the RBZ.

3.3.4 Results and analysis

The phase diagram of the model according to our calculations is shown in Fig. 4.7. For all values of δ the variational parameter at which the total energy is minimized is finite for large V indicating a CDW type insulating phase. At some V_t for each δ, the minimum at finite V becomes a local minimum, with $\alpha = \infty$ becoming the global minimum, meaning that within our variational approximation the phase transition is first order (see Fig. 3.14). The small V phase at $\delta = 0$ is a Fermi sea, while for finite δ it is an SSH state. The metastable phase disappears at some finite δ. Phase III is an insulating phase. When $\delta = 0$ the skew is zero in this phase, when it is finite, a finite skew develops (see Fig. 3.17). Our phase diagram is qualitatively similar to the two-dimensional KMH model, where the topologically non-trivial phases at small interaction become magnetically ordered insulating phases [46, 54].

We also calculated the curves traced out by the vector $\mathbf{d}$ which defines the

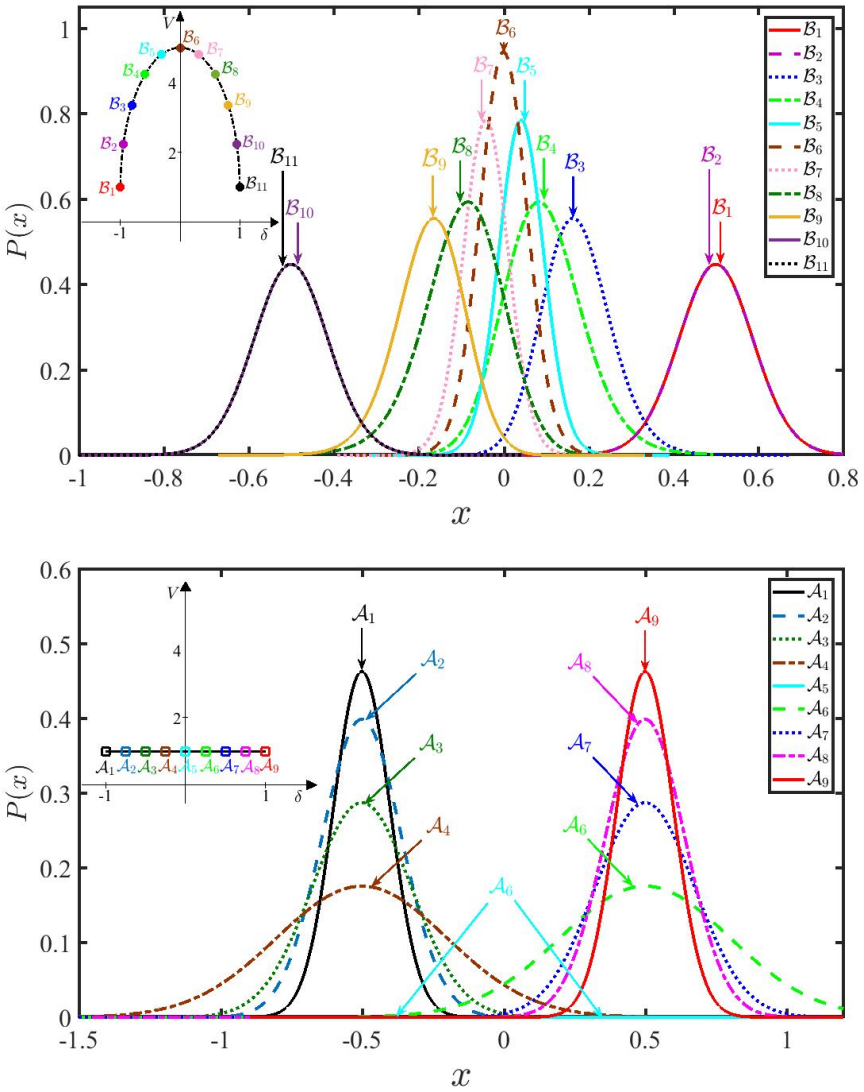

Figure 3.18: Reconstructed polarization distributions along the two paths shown indicated in Fig. 3.17. The upper panel(lower panel) shows reconstructed polarizations along the ellipse(straight line) between the points $-1, 1$ to $1, 1$ on the $\delta - V$ plane.

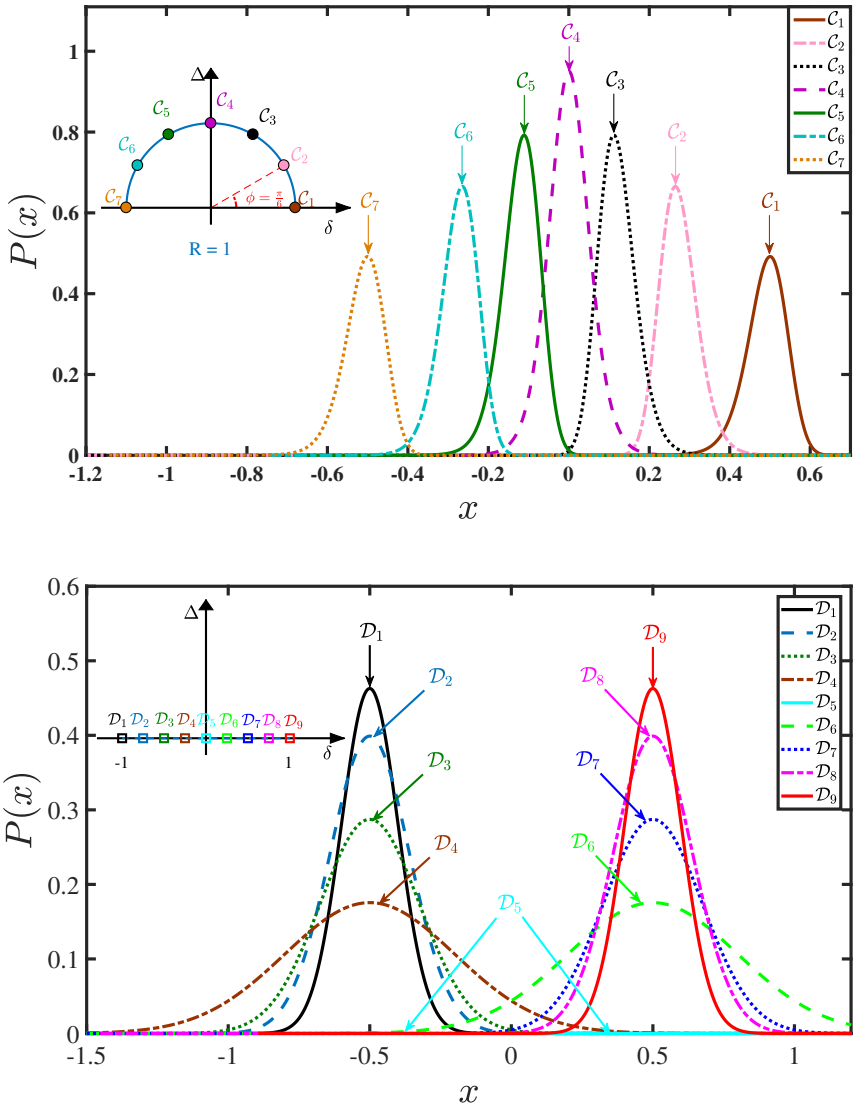

Figure 3.19: Reconstructed polarization for the Rice-Mele model along the paths indicated in the inset of each plot. The paths are represented on the $\delta - \Delta$ plane.

parent Hamiltonian derived in section 3.3.2, shown in Fig. 3.16. The left panel (part (a)) shows the curve traced out by the Brillouin zone along specific points of a curve in the parameter space of the Hamiltonian which starts at $\delta = -1, V = 1$ and ends at $\delta = 1$ and $V = 1$. The curve in between is an ellipse which does not cross the metallic phase line. The curves traced out our cyclic in three dimensions. At $\delta = 0$ is approached the cyclic curves become "thinner" and at $\delta = 0$ itself the BZ is represented by a line rather than a cyclic curve. The right panel (part (b)) shows what happens along the straight line $V = 1$ but δ varying from minus one to one. This is exactly what happens in the SSH model, whose Hamiltonian is $d_z = -t\cos(k)$ and $d_y = -\delta sin(k)$. As δ approaches to zero (gap closure) the curve becomes a line along the y-axis. The left panel gives some indication of the effect of correlation. Standard mean-field theory of the SSH model gives the RM model corresponding to an additional term in the d_x directions with a renormalized on-site potential strength, and whose curves (not shown) would be similar to panel (b) of Fig. 3.16, but with a shift in the d_x direction. One difference between mean-field theory and our BWF based treatment can be seen in the curves of panel (a) of Fig. 3.16.

In part (a) of Fig. 3.17 we show the polarization (C_1) on the $\delta - V$ plane. The polarization is take to be zero in the limit $V \to \infty$. As V decreases the absolute value of the polarization increases, its sign depends on the sign of δ. For finite δ the polarization saturates at a finite value of δ. Particularly interesting is the behavior at $\delta = 0$, where the polarization remains the same value, but we see that below $V < 1.3365...$ it rises rapidly from $\delta < 0$ to $\delta > 0$, almost discontinuously. For $V > 1.3365...$, the rise in C_1 across $\delta = 0$ is smooth.

In part (b) of this Figure we show two paths we have chosen for our subsequent analysis. Paths $\mathcal{A}$ and $\mathcal{B}$ both connect the points $-1, 1$ and $1, 1$ on the $\delta - V$ plane, but path $\mathcal{A}$ crosses the line segment $\delta = 0$, $0 < V < 1.3365...$, while $\mathcal{B}$ does not, it passes $\delta = 0$ above the point $V = 1.3365....$ For the elliptical path the moments and cumulants are shown in part (c) of the Figure. All cumulants and moments change continuously C_2 is minimum at $\delta = 0$. In contrast to this, along the linear path C_1 changes discontinuously. C_2 increases sharply around $\delta = 0$, indicating delocalization. All the cumulants change rapidly around $\delta = 0$,

the even cumulants are even functions, while the odd ones are odd.

In Fig. 3.18 we show reconstructed polarization distributions along a chosen set of points along the two different paths $\mathcal{A}$ and $\mathcal{B}$. Along the elliptical path ($\mathcal{B}$) the polarization distribution "walks across" smoothly between the two positions related by symmetry. The distribution is a smooth function, the maximum changes continuously, and the shape of the distribution indicates a localized state (insulating). In contrast to this, when the polarization is reconstructed along the line which crosses the line $\delta = 0, 0 < V < 1.3365...$, the maximum of the distribution remains fixed in the interval $\delta > 0$, while the width of the distribution is increasing (the distribution is becoming more delocalized). At $\delta = 0$ the distribution is flat, the system is delocalized. We interpret this as a conducting state. For $\delta < 0$ the distribution localizes around a different maximum. As the absolute value of δ increases the distribution becomes more localized.

We can relate the effect of the correlation to what happens around the topologically nontrivial point [91] of the SSH and RM models. We take as the definition of the RM model to be the SSH model defined above, plus an alternating on-site potential, which breaks the chiral symmetry, of the form $\Delta \sum_j (-1)^j c_J^\dagger c_j$, where Δ denotes the strength of the potential. In Fig. 3.19 we show reconstructed polarizations along a semi-circle on the $\delta - \Delta$ plane, and along a line along which the model is SSH, with a topological phase transition protected by symmetry. The gap closure (phase transition) point is at $\delta = \Delta = 0$. The symmetry broken semi-circular path shows an evolution of the polarization distribution similar to the upper panel in Fig. 3.18 with the maximum shifting continuously, while along the linear path, the maximum shifts discontinuously between the $\delta < 0$ and $\delta > 0$ cases.

Chapter 4

Topological physics in one-dimensional systems

Topological ladder models are one-dimensional systems which, however, often exhibit effects usually associated with two dimensions. Since a ladder consists of two legs separated by a finite distance, and enclosing a definite area, it is possible to apply a magnetic field perpendicular to this area and observe a quantum Hall response. Another way to think about this is to realize that to demonstrate the existence of chiral edge currents, one needs a strip, which is also an effective one-dimensional system, with a finite width (a ladder is a strip with width of one, or a small number of, lattice constants). We construct a topological ladder model, one-dimensional, which lead to the Haldane and Kane-Mele model in two dimensions.

4.1 A one-dimensional analog of the Haldane model

The model is effectively 1D, inversion and time-reversal symmetries are broken simultaneously. The model is a two-legged ladder model with an on-site potential

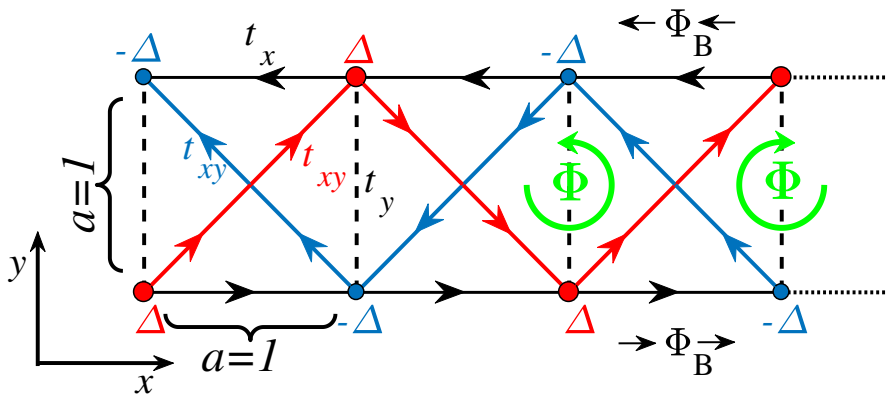

Figure 4.1: Ladder model. The hopping parameters are defined as follows: t_x denotes hopping along the legs of the ladder, t_y denote the hoppings perpendicular to legs, t_{xy} denotes hoppings occurring diagonally between legs, connecting second nearest neighbors. The sites in red(blue) indicate where the site depedendent potential is positive(negative). A Peierls phase of Φ is introduced along the diagonal hoppings. These can be thought of as arising from magnetic impurities residing halfway through the perpendicular (t_y) hoppings and arranged antiferromagnetically.

and diagonal hoppings with a Peierls phase. The hoppings connecting the different legs of the ladder perpendicularly move the positions of the gaps within the reduced Brillouin zone (BZ) towards the origin. Turning on a finite flux along the diagonal bonds allows closure of either gap.

Our model is represented in Fig. 4.1. The legs of the ladder are one-dimensional tight-binding models with an alternating on-site potential of strength Δ. We study the model at half-filling. The hopping parameters for hoppings along the legs are t_x, t_y denote hoppings perpendicular to the legs, and t_{xy} denotes diagonal hoppings. A Peierls phase of Φ is introduced along the diagonal bonds. Since the phases are directed such that they close around squares, they can be viewed as magnetic impurities placed along the t_y bonds. In contrast to the Haldane model [25] (HM), the fluxes in neighboring closed squares circulate in the opposite direction, corresponding to an antiferromagnetic line of impurities. If t_y and t_{xy} are zero, but t_x and Δ are finite, the model exhibits two equal gaps at the edge of the reduced BZ (where the energy difference at half-filling is minimum). Turning on t_y moves both of these gaps towards the origin. Turning

on t_{xy} and a finite Φ allows the closing of either gap without closing the other. An external magnetic field applied perpendicular to the ladder is indicated by the other Peierls phase Φ_B.

The Hamiltonian of the model in reciprocal space (taking the lattice constant to be unity) can be written as a 4×4 matrix as

$$H(\Phi, \Phi_B) =$$

$$\sum_k \begin{pmatrix} \Delta & -2t_x\cos(k+\Phi_B) & -2t_{xy}\cos(k+\Phi) & -t_y \\ -2t_x\cos(k+\Phi_B) & -\Delta & -t_y & -2t_{xy}\cos(k-\Phi) \\ -2t_{xy}\cos(k+\Phi) & -t_y & \Delta & -2t_x\cos(k-\Phi_B) \\ -t_y & -2t_{xy}\cos(k-\Phi) & -2t_x\cos(k-\Phi_B) & -\Delta \end{pmatrix}. \tag{4.1}$$

We first focus on the case $\Phi_B = 0$. In this case it is convenient to write the Hamiltonian as a sum of three terms, each of which is a direct product of a 2×2 matrix and one of the Pauli matrices as

$$H(\Phi, 0) = \sum_k \left[\begin{pmatrix} 0 & -2t_{xy}\cos(k)\cos(\Phi) \\ -2t_{xy}\cos(k)\cos(\Phi) & 0 \end{pmatrix} \otimes I_2 \right. \tag{4.2}$$
$$\left. + \begin{pmatrix} -2t_x\cos(k) & -t_y \\ -t_y & -2t_x\cos(k) \end{pmatrix} \otimes \tau_x + \begin{pmatrix} \Delta & 2t_{xy}\sin(k)\sin(\Phi) \\ 2t_{xy}\sin(k)\sin(\Phi) & \Delta \end{pmatrix} \otimes \tau_z \right],$$

In Eq. (4.22) I_2 denotes the 2×2 identity matrix, and $\tau_x\tau_y, \tau_z$ denote the Pauli spin matrices. The overall Hilbert space can be viewed as a direct product of two two-dimensional spaces. The Pauli matrices in Eq. (4.22) act in the "right" subspace. A rather convenient fact is that the matrix

$$U = \frac{1}{\sqrt{2}} \left[\begin{pmatrix} 1 & 1 \\ 1 & -1 \end{pmatrix} \otimes I_2 \right], \tag{4.3}$$

will diagonalize all three of the matrices on the left of each of the terms comprising $H(\Phi, 0)$, and the gap closure conditions can be readily obtained. The second term of $H(\Phi, 0)$ results in a diagonal 2×2 matrix with elementss $\lambda_x^{\pm} = -2t_x\cos(k) \pm t_y$ times τ_x. Requiring that either one is zero gives the values of k at which the gaps reside ($k^{\pm}$). The third term becomes a diagonal 2×2 matrix with elements

$\lambda_z^{\pm} = \Delta \pm 2t_{xy}\sin(k)\sin(\Phi)$ multiplying tau_z. Substituting either of $k^{\pm}$ and requiring that one of the $\lambda_z^{\pm}$ is zero leads to a band structure in the reduced BZ with one gap closed (either at k^+ or at k^-). Two examples of the band structure as a function of the external parameters are shown in Fig. 4.2. The phase diagram is shown in the inset of Fig. 4.2. Gap closure occurs at the lines.

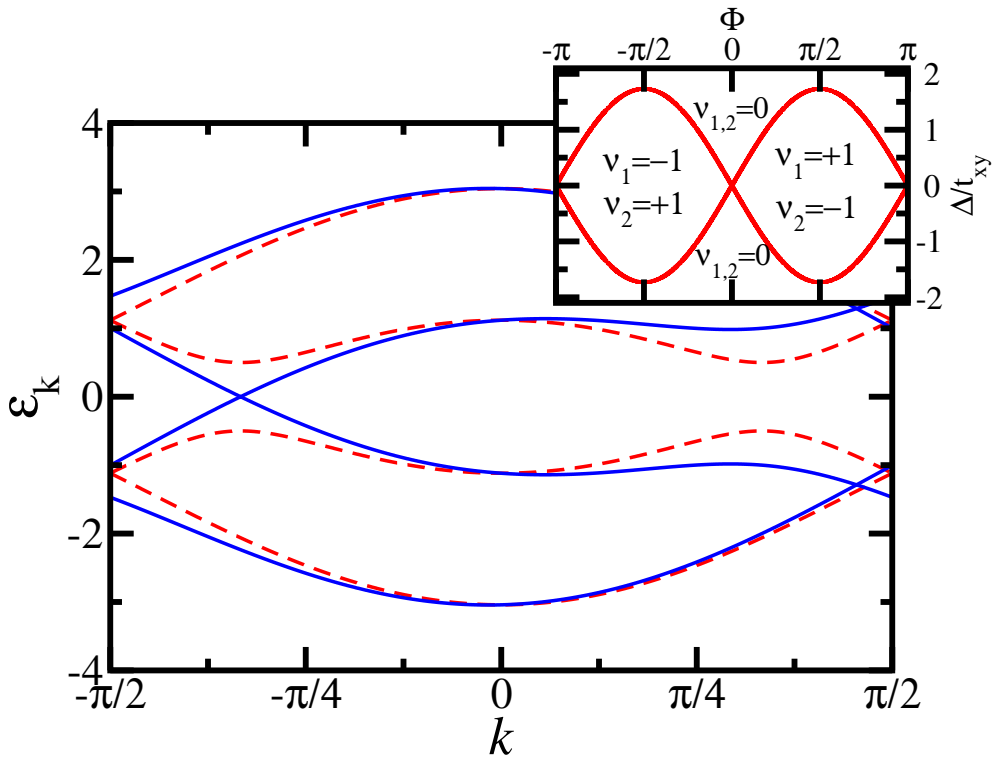

Figure 4.2: Band structure within the reduced Brillouin zone (RBZ). The red dashed lines indicate the band structure for a system with $t_x = 1, t_y = 1, t_{xy} = 0, \Delta = 0.5$. At half-filling this system is gapped. For $t_y = 0$ the gaps would be at the edge of the RBZ ($k = \pm\frac{\pi}{2}$). Finite t_y causes the gaps to move towards the origin (the gap is at $k^{\pm} = \pm\text{acos}(\frac{t_y}{2t_x})$). The blue solid lines indicate gap closure when t_{xy} is made finite ($t_{xy}\sin(k^{\pm})\sin(\Phi) = \Delta$, ($\Phi = \frac{\pi}{2}$)). The inset shows the phase diagram (where gap closure occurs) for $t_x = 1, t_y = 1$. The lines separate two insulating phases. The red(black) lines indicates gap closure occurring at $k^+(k^-)$.

The shape of the phase diagram, and more importantly, the meaning of the

parameters on the axes (Δ vs. Φ) bears a definite resemblance to the HM [25]. The main reason for this is that like in the HM, inversion symmetry is broken via an on-site potential, and simultaneously, TRS is broken by introducing a Peierls phase on second nearest neighbor hoppings. If one was to apply Haldane's steps in a one-dimensional chain (Rice-Mele model with Peierls phase on second nearest neighbor bonds), no gap closure would result, since in this case the distance between two nearest neighbors is twice the lattice constant, and the contribution at the gap closure points (which are at the edge of the RBZ) would be zero. The ladder configuration allows for second nearest neighbors whose length is not equal to two lattice constants, and the closing of the gap at either k^+ or k^-. We note in passing that a Haldane like phase diagram is exhibited in an extended SSH model, in which the Peierls phases on hoppings between different sublattices differ [104].

To characterize the symmetry, let us consider the case $\Phi = \pi/2$. PHS is achieved by $c_k \to c_k^\dagger$ and $c_k^\dagger \to c_k$ which reverses the signs of all matrix elements. PHS can also be realized by the operator $C = i(I_2 \otimes \tau_y)$, which squares to minus one. If $\Delta = 0$ TRS is realized by $T = (I_2 \otimes \tau_x)\kappa$, which squares to plus one, and the system is in the CI symmetry class. Finite Δ breaks TRS, and the symmetry class of the model becomes C. The operator $R = (I_2 \otimes \tau_x)$ can also act as the reflection of the different legs of the ladder. This operator anti-commutes with the PHS operator, but commutes with the TRS.

For a complete topological characterization, however, it is expedient to start with the Hamiltonian after applying the similarity transformation in Eq. (4.3). Considering the case $\Phi = \pi/2$ for simplicity results in

$$h(\pi/2, 0) = U^{-1} H(\pi/2, 0) U = h_x \otimes \tau_x + h_z \otimes \tau_z, \tag{4.4}$$

where h_x is a 2×2 diagonal matrix with elements $-2t_x \cos(k) \pm t_y$ and so is h_z with $\Delta \mp 2t_{xy} \sin(k)$. Hence, we have two decoupled subsystems whose Hamiltonian is similar to the model analyzed by Jackiw and Rebbi [101], where zero-mode edge states were already demonstrated. If one of the 2×2 models is Fourier transformed back to real space, the result is a Creutz model with a potential Δ on all the sites forming one leg of the ladder, and $-\Delta$ on the other. The symmetry

characterization for $\Delta = 0$ is BDI [110, 111], for finite Δ the TRS and PHS are broken, but CS is maintained, leading to AIII. Both of these have a $\mathbb{Z}$ topological index.

It is instructive to compare at this point to the spin-dependent "doubling" situation in the Kane-Mele model. The Kane-Mele model can be constructed in two steps. One first takes two Haldane models, one for each spin, and couples them via a Rashba term. In the Haldane model TRS is broken, but in the combined system it is restored, and at TRS invariant k-points a degeneracy is guaranteed by Kramers theorem. Our model can be constructed by taking two extended Creutz models, which are not PHS invariant individually, but their combination is PHS-1. The Creutz models in our case are arrived at after transforming our original Hamiltonian, meaning that they are defined in terms of quasi-particles, rather than real particles on the lattice, hence the analog of "doubling" is in terms of linear combinations of orbitals (the transformation in Eq. (4.3) combines sites in a unit cell with either both Δ or both $-\Delta$). There is no Kramers theorem, but a degeneracy can be produced by tuning the reflection and TRS breaking terms. The gap closure does not have to occur at TRS invariant points.

4.1.1 Winding number of Haldane-like model

Extending the work of Ryu *et al.* [112] we construct the topological index. The ground state projector can be written as

$$P(k) = \frac{1}{2}[I_4 - \bar{Q}(k)] = \frac{1}{2}[I_4 - \mathbf{h}(k) \otimes \tau]. \tag{4.5}$$

The matrix $\bar{Q}(k)$ can be brought into off-diagonal form ($Q(k)$) by applying the transformation

$$\frac{1}{\sqrt{2}} \left[I_2 \otimes \begin{pmatrix} 1 & 1 \\ i & -i \end{pmatrix} \right], \tag{4.6}$$

and switching the order of multiplication for the direct product we arrive at the $Q(k)$ matrix

$$Q(k) = \begin{pmatrix} 0 & q(k) \\ q(k)^* & 0 \end{pmatrix}, \tag{4.7}$$

where $q(k)$ is a diagonal 2×2 matrix with elements $-h_z(k)-ih_x(k)$. The winding number [112] is given by

$$\nu = \frac{i}{2\pi}\int_{-\pi}^{\pi} \mathrm{Tr}\left[q^{-1}(k)\partial_k q(k)\right] dk = \nu_1 + \nu_2, \tag{4.8}$$

where

$$\nu_j = \frac{i}{2\pi}\int_{-\pi}^{\pi} \left[q_j^{-1}(k)\partial_k q_j(k)\right] dk, \tag{4.9}$$

with

$$\begin{aligned} q_1(k) &= \Delta - 2t_{xy}\sin(k) + it_y + 2it_x\cos(k) \\ q_2(k) &= \Delta + 2t_{xy}\sin(k) - it_y + 2it_x\cos(k). \end{aligned} \tag{4.10}$$

The winding numbers can be written as contour integrals,

$$\nu_j = \frac{(-1)^j}{2\pi i}\oint \frac{d\mathbf{z}}{\mathbf{z}-\mathbf{z}_j}, \quad j = 1,2 \tag{4.11}$$

where the integral is around the ellipse defined by the curve

$$\mathbf{z} = t_x\cos(k) + it_{xy}\sin(k), \tag{4.12}$$

with $-\pi \le k < \pi$, and

$$\begin{aligned} \mathbf{z}_1 &= \frac{-t_y}{2} + i\frac{\Delta}{2} \\ \mathbf{z}_2 &= \frac{t_y}{2} + i\frac{\Delta}{2}. \end{aligned} \tag{4.13}$$

Both winding numbers will be zero, if the points $\mathbf{z}_1$ and $\mathbf{z}_2$ fall outside the curve defined by Eq. (4.12). Since the curve is symmetric with respect to the imaginary axis, the two points will be either both inside the curve or outside. When the points are inside, $-\nu_1 = 1 = \nu_2$. The topological index can be called the *mirror winding number*, the one-dimensional analog of the mirror Chern number[113, 114]. The conditions for the points to fall on the curve correspond to the gap closure conditions derived above.

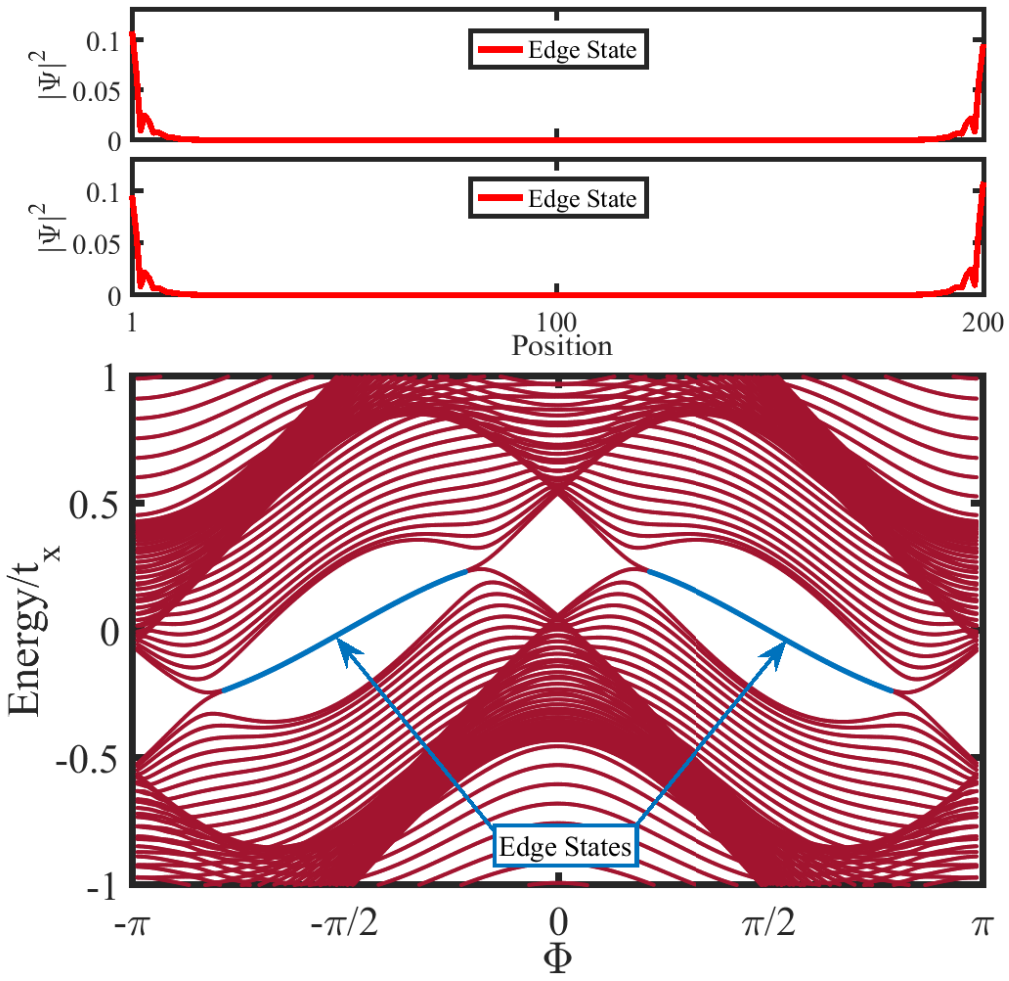

Figure 4.3: Lower panel: band structure of a system of size 100 sites with open boundary conditions. In this calculation $t_x = 1$, $t_y = 1$, and $t_{xy} = 0.3$. Inside the lobes (see inset of Fig. 4.2) edge states arise. Upper two panel: squared modulus of the wavefunction for the two edge states averaged over the two legs of the ladder, for $\Phi = \pi/2$ for a system of 200 sites.

Figure 4.3 shows the band structure of the system under open boundary conditions. The lower panel shows the band structure when Φ is scanned between $-\pi, \pi$ for $t_x = t_y = 1$, and $t_{xy} = 0.3$. Inside the lobes of the phase diagram two edge states are found (indicated in blue color in the figure). The upper panels of the figure show the squared modulus of these edge states. Each one is localized near the ends of the ladder.

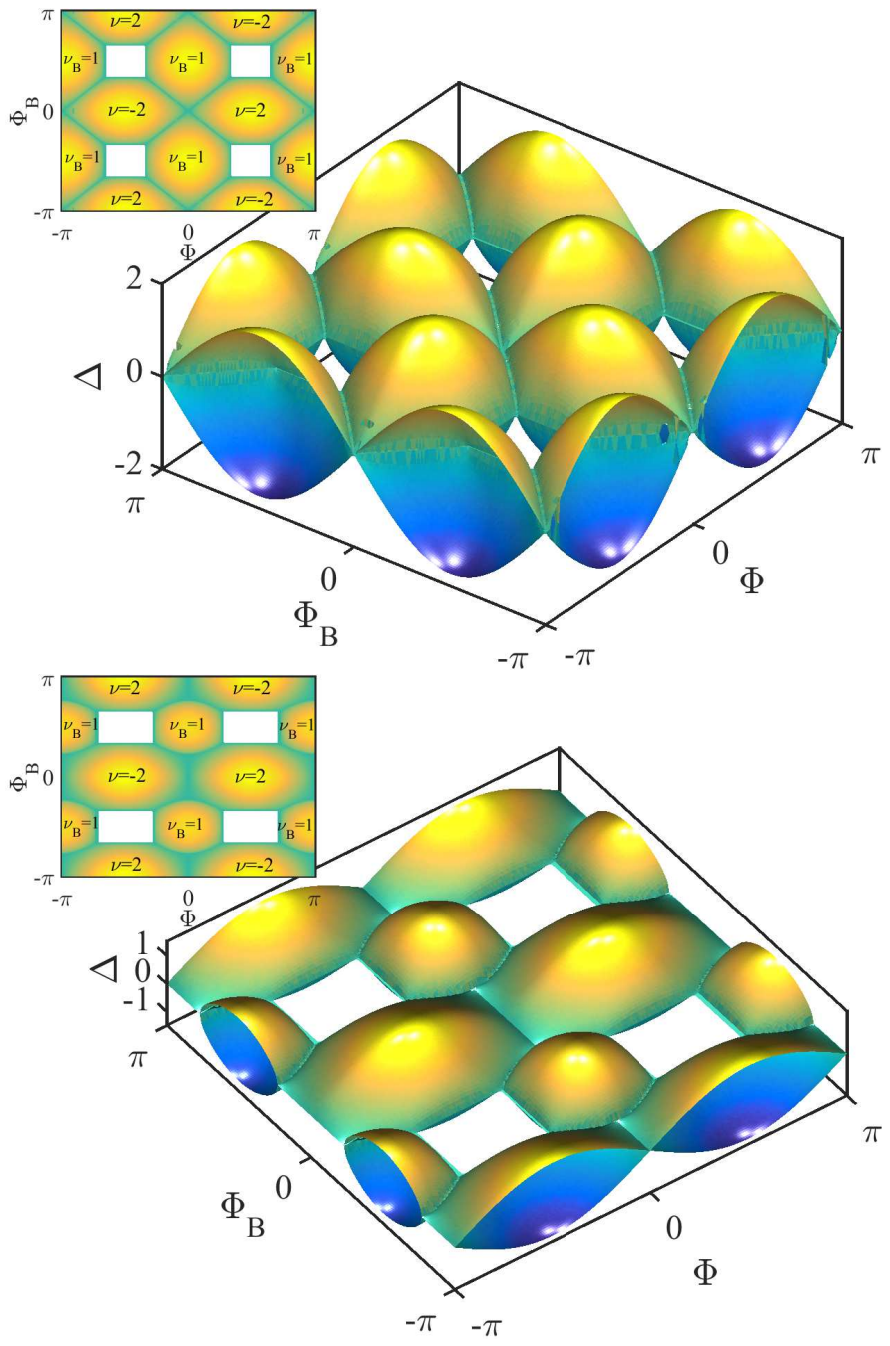

Figure 4.4: Examples of phase diagrams in three dimensions. The upper(lower) panel shows the phase diagram Δ, Φ, Φ_B for $t_x = t_y = t_{xy} = 1$ ($t_x = t_y = 1, t_{xy} = 0.75$). The phase diagram was determined by searching for the gap closure.

4.1.2 Hall response of the Haldane-like model

We have also considered the Hall response of the system, to a magnetic field perpendicular to the plane of the ladder. The Středa formula [115, 116] for the Hall conductance reads

$$\sigma_H = ec \left. \frac{\Delta n}{\Delta \Phi_B} \right|_{\mu}, \tag{4.14}$$

We applied a magnetic field by threading a flux Φ_B on the bonds with hopping parameter t_x in opposite directions on each legs of the ladder (as indicated in Fig. 4.6). We first calculate the chemical potential for half-filling for $\Phi_B = 0$. Subsequently we calculated the number of states below the chemical potential at $\Phi_B = 0$ when the flux is changed by a flux quantum per unit cell. In the topologically non-trivial phase changing the flux in either direction leads to a decrease in the number of states below the chemical potential, by two particles. This happens for both positive and negative flux. In the topologically trivial phase there is no change in the number of particles when a flux is threaded.

We now investigate the model with $\Phi = 0$, and a flux $\Phi_B = \pi/2$, corresponding to a magnetic field perpendicular to the ladder. The behavior we find is very similar to what we found for the finite Φ case. The PHS operator in this case is $C = [i\sigma_y \otimes \tau_x]$, again squaring to minus one ($\sigma_x, \sigma_y, \sigma_z$ denote the Pauli matrices acting in the "left" subspace). The TRS is $T = [\sigma_x \otimes I_2]K$, which squares to one, i.e. the system falls in the CI symmetry class. The operator $[\sigma_x \otimes I_2]$ is also an inversion operator, although, unlike in the previous case, it inverts halfway along a chosen bond, horizontal in Fig. 4.6. For the case $\Delta = 0$ we obtain a Hamiltonian similar to that in Eq. (4.22),

$$\begin{aligned} H(0, \pi/2) = \sum_k \Bigg[\sigma_x \otimes \begin{pmatrix} -2t_{xy}\cos(k) & -t_y \\ -t_y & -2t_{xy}\cos(k) \end{pmatrix} \\ + \sigma_z \otimes \begin{pmatrix} 0 & -2t_x \sin(k) \\ -2t_x \sin(k) & 0 \end{pmatrix} \Bigg]. \end{aligned} \tag{4.15}$$

Here we can apply the similarity transformation via

$$V = \frac{1}{\sqrt{2}} \left[I_2 \otimes \begin{pmatrix} 1 & 1 \\ 1 & -1 \end{pmatrix} \right], \tag{4.16}$$

and arrive at

$$h(0,\pi/2) = V^{-1}H(0,\pi/2)V = \sigma_x \otimes g_x + \sigma_z \otimes g_z, \tag{4.17}$$

with g_x and g_z being 2×2 diagonal matrices with elements $-2t_{xy}\cos(k) \mp t_y$ and $\mp 2t_x \sin(k)$, respectively. The two 2×2 models which form the 4×4 model are two Creutz models [71, 72] with band structures displaced with respect to each other by π. The transformation in Eq. (4.16) combines sites of the same ladder leg within a unit cell, therefore the Creutz models in this case are defined in terms of quasi-particles of this kind. The gap closures occur at $k = 0$ and π when $t_y = \pm 2t_{xy}$. We can again construct the mirror winding number scheme used above. For the topological state the curve

$$\mathbf{z} = t_{xy}\cos(k) + it_x \sin(k) \tag{4.18}$$

will include the points $\pm t_y/2$, with winding numbers of opposite signs. If these points are outside the curve, both winding numbers will be zero. It is well-known that the Creutz model is topological and exhibits edge states [71].

For finite values of Δ the topological state survives, since the state is adiabatically connected to the $\Delta = 0$ state. The phase diagram can be determined from the fact that the gap closure has to occur at $k = 0$ (a single point in the reduced Brillouin zone). Setting k to zero in the Hamiltonian we can diagonalize the resulting matrix, and obtain the gap closure condition,

$$\Delta = \pm\sqrt{(4t_{xy}^2 - t_y^2)\left(1 - \left(\frac{t_x}{t_{xy}}\cos(\Phi_B)\right)^2\right)}. \tag{4.19}$$

At last, for the case $\Phi = \pi/2$ we consider adding a term of the form $\Gamma[\sigma_z \otimes \tau_z]$, which still preserves PHS, but mixes the two Creutz-like subsystems (in this sense an analog of the Rashba term in the Kane-Mele model). The q-matrix in this case becomes

$$q(k) = h_x + ih_z + \begin{pmatrix} 0 & \Gamma \\ \Gamma & 0 \end{pmatrix}. \tag{4.20}$$

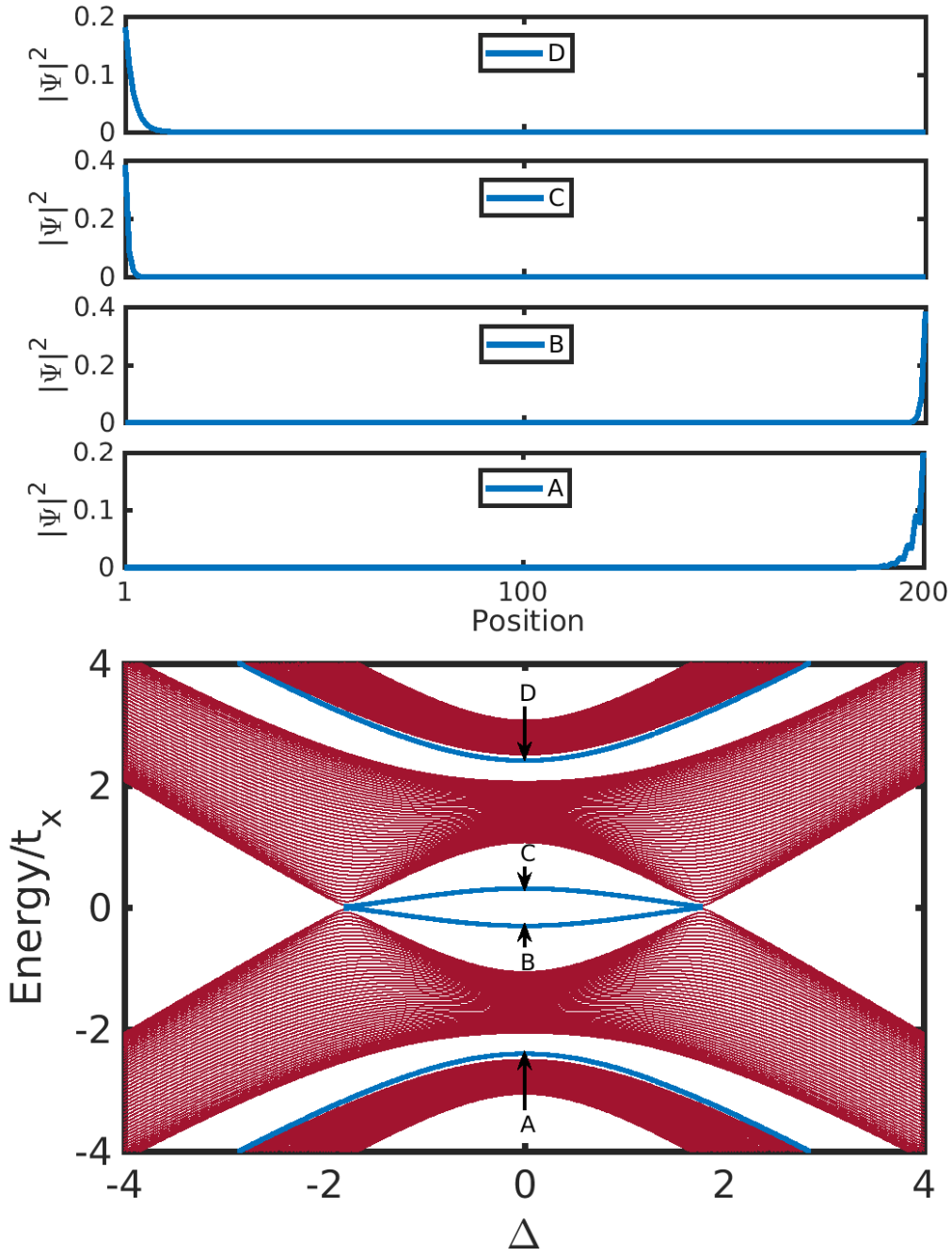

Figure 4.5: Band structure of system with finite $\Gamma = 0.5$ and edge states (upper four panels). The other parameters are $t_x = t_y = t_{xy} = 1$, $\Phi = \pi/2$, and $\Phi_B = 0$. The variable Δ is scanned. Localized edge states are found at quarter, half, and three-quarter fillings.

Although the derivation is more cumbersome than in the previous case, due to the off-diagonal elements of the q-matrix, the winding number falls into the same two pieces as in Eqs. (4.8-4.13), the gap closure conditions for the two contributions are the same as before.

In Fig. 4.5 the band structure is shown for a system with $\Gamma = 0.5$, $t_x = t_y = t_{xy} = 1$, $\Phi = \pi/2$, $\Phi_B = 0$ scanned over the variable Δ. The four midgap states, two at half filling, one at quarter and three-quarter fillings are evaluated at $\Delta = 0$. The upper panels show that these midgap states are indeed localized edge states. The state at half-filling are non-degenerate, unlike for zero Γ. Note that the states form "particle-hole" pairs: for a given negative energy state, there is a positive energy state which is localized on the other edge.

4.2 A one-dimensional analog of the Kane-Mele model

The Creutz model is a quasi-1D ladder model which exhibits a quantum phase transition separating a trivial phase from a symmetry-protected topological phase. The topological phase is characterized by a winding number, and if open boundary conditions are applied, localized edge states are found. Let t_x denote hoppings along the legs, t_y the hoppings perpendicular to the legs, and t_{xy} the diagonal hoppings along unit cells. In the original Creutz model a magnetic field perpendicular to the plane of the system is applied, resulting in Peierls phases along the legs of the ladder, pointing in opposite directions on different legs of the ladder. For a Peierls phase of $\pi/2$ the resulting Hamiltonian is

$$H_C = -\sum_k [(2t_x \sin(k))\hat{\sigma}_z + (t_y + 2t_{xy}\cos(k)\hat{\sigma}_x)]. \tag{4.21}$$

Gap closure occurs at the points $k = 0, \pi$, depending on whether $t_y = 2t_{xy}$ or $t_y = -2t_{xy}$. Our first step is to set the bonds on the upper(lower) leg to $t_x(-t_x)$ and introduce Peierls phases of $\pi/2$ on the diagonal bonds as indicated in Fig.

4.6. The Hamiltonian is now

$$H_1 = -\sum_k [(2t_x \cos(k))\hat{\sigma}_z + (t_y + 2t_{xy}\cos(k+\Phi)\hat{\sigma}_x)]. \tag{4.22}$$

The first term alone corresponds to a band stucture with one-dimensional Dirac points at $k = \pm\pi/2$, which are time-reversal invariant pairs. The second term opens gaps in general with masses of opposite signs at opposite Dirac points. The phase diagram (determined by the gap closure condition) is the same as that of the HM,

$$\frac{t_y}{2t_{xy}} = \pm\sin(\Phi). \tag{4.23}$$

The sign in Eq. (4.23) determines which of the two gaps in the Brillouin zone closes.

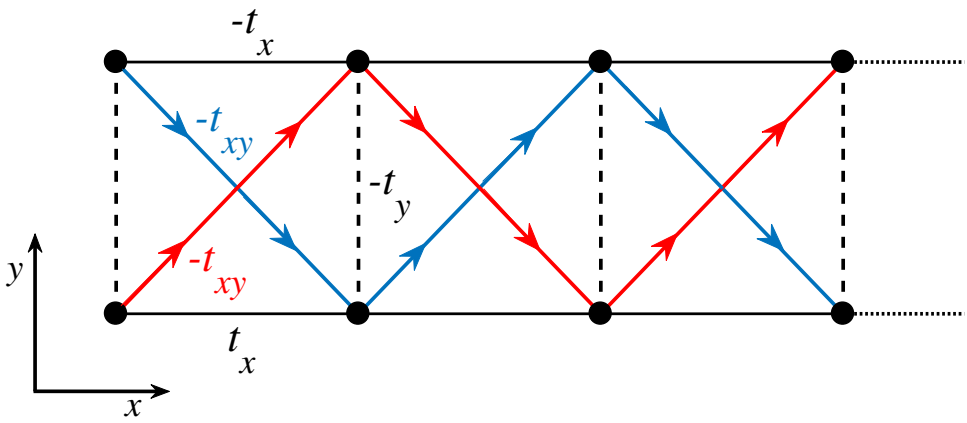

Figure 4.6: Graphic representation of our model. $t_x(t_y)$ denotes hoppings along horizontal(vertical) bonds. t_{xy} denotes diagonal bonds. We apply Peierls phases along the diagonal bonds along the directions indicated.

Given that the gap closures occur at time-reversal invariant points, we can proceed to construct a one-dimensional analog of the Kane-Mele model, by first introducing spin,

$$H_2 = \sum_k d_1(k)\Gamma^{(1)} + d_2(k)\Gamma^{(2)} + d_{25}(k)\Gamma^{(25)}, \tag{4.24}$$

where we have used the following Γ-matrices,

$$\Gamma^{(a)} = \{\sigma_x \otimes I_2, \sigma_z \otimes I_2, \sigma_y \otimes \sigma_x, \sigma_y \otimes \sigma_y, \sigma_y \otimes \sigma_z\}, \tag{4.25}$$

with $a = 1, ..., 5$, and

$$\Gamma^{(ab)} = \frac{1}{2i}[\Gamma^{(a)}, \Gamma^{(b)}], \tag{4.26}$$

H_2 can be viewed as the "square" of the H_1 Hamiltonian. We can now add the Rashba spin orbit coupling term resulting in

$$H = H_2 + d_3(k)\Gamma^{(3)} + d_{35}(k)\Gamma^{(35)}. \tag{4.27}$$

The coefficients in Eqs. (4.24) and (4.27) are given by

$$\begin{aligned} d_1(k) = -t_y, d_2(k) = -2t_x \cos(k), d_3(k) = \lambda_R \\ d_{25}(k) = 2t_{xy} \sin(k), d_{35}(k) = 2\lambda_R \sin(k). \end{aligned} \tag{4.28}$$

4.2.1 Symmetry analysis and topological indices

Using the appropriate time-reversal, particle-hole and chiral symmetry operators, one-dimensional models can be placed [50, 68] into topological classes. For the shifted Creutz model (Eq. (4.21)), the operator $T = i\sigma_x K (C = i\sigma_z K$, with K denoting complex conjugation) can be taken to be the time reversal (particle hole) operator, and the time-reversal ($T^\dagger H(k)T = H(-k)$), partile-hole ($C^\dagger H(k)C = -H(-k)$) and chiral symmetries ($S^\dagger H(k)S = -H(k)$, where $S = TC$ is the chiral symmetry operator). This implies that the band-structure comes in pairs of $\pm\epsilon_k$. $T^2 = C^2 = S^2 = 1$, placing the Creutz model in the BDI class. For the shifted Creutz model for $\Phi = \pi/2$ (Eq. (4.22)) the time-reversal and particle-hole symmetries are destroyed, but the chiral symmetry remains ($S^\dagger H(k)S = -H(k)$), implying that the band-structure again comes in pairs of $\pm\epsilon_k$. The model falls in the symmetry class AIII.

For the spinful model we study, Eqs. (4.24) and (4.27) the time-reversal and particle-hole operators take the form $T = i(I_2 \otimes \sigma_y)K$, $C = i(\sigma_y \otimes \sigma_x)K$. In this case the square of the operators is $T^2 = C^2 = -1$, and $S^2 = 1$, placing these models in the CII symmetry class. One can refine the symmetry characterization further by also considering the reflection operator [69, 70], which sends k to $-k$ without altering the spin. This operator is $R = (I_2 \otimes \sigma_x)$, which anti-commutes

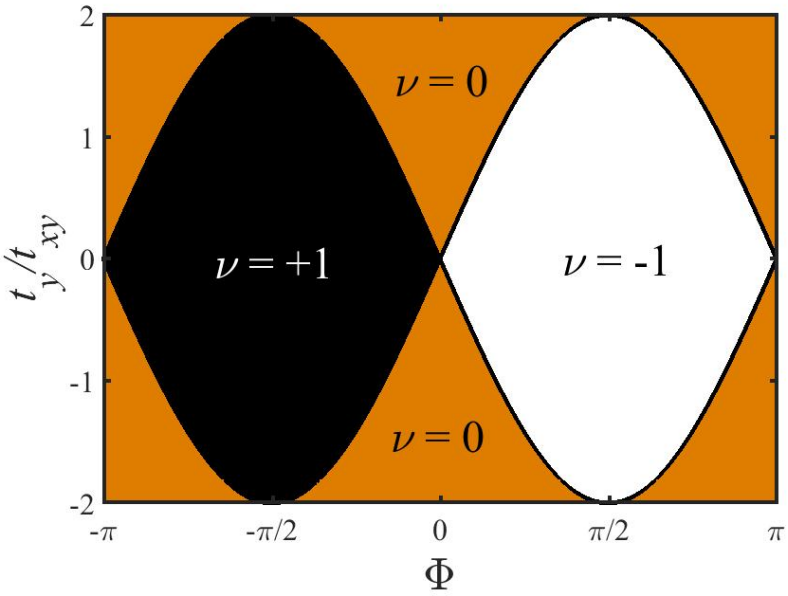

Figure 4.7: Phase diagram of the system where gap closure occurs. The numbers in the figures denote the topological winding number.

with T, but commutes with C. In terms of mirror symmetry class [69, 70] the model falls in class C, with a topological index of $2\mathbb{Z}$.

For the a chiral symmetric Hamiltonian (Eq. (4.22)) we apply a unitary transformation [112], constructed from spinors of spin in the y direction,

$$U = \frac{1}{\sqrt{2}} \begin{pmatrix} 1 & 1 \\ i & -i \end{pmatrix}, \tag{4.29}$$

to our Hamiltonian. This leaves us with the off-diagonal form,

$$\mathcal{H}_T = U^\dagger \mathcal{H} U = \tag{4.30}$$
$$= 2t_x \cos(k)\sigma_x + [t_y - 2t_{xy}\sin(k)]\sigma_y = \begin{pmatrix} 0 & q \\ q^\dagger & 0 \end{pmatrix}.$$

where $q = 2t_x \cos(k) - i[t_y - 2t_{xy}\sin(k)]$. The winding number density is given by,

$$w(k) = iq^{-1}(k)\partial_k q(k), \tag{4.31}$$

from which the winding number can be obtained by integrating across the full

Brillouin zone after setting $t_x = t_{xy} = 1$, resulting in

$$\mathcal{W} = \int_{-\pi}^{\pi} \frac{dk}{2\pi} w(k), \tag{4.32}$$

which can be turned into a contour integral around the unit circle via $z = e^{ik}$. If the point $(0, it_y/2)$ is within the ellipse defined by $(2t_x \cos(k), 2t_{xy} \sin(k))$ with $0 \leq k < 2\pi$, the winding number is minus one. Otherwise it is zero.

We proceed to extend this result to Eq. (4.24). In this case we have 4-by-4 block-diagonal Hamiltonian,

$$\begin{aligned} \mathcal{H}(k) &= 2t_x \cos(k)\sigma_0 \otimes \sigma_z - 2t_{xy} \sin(k)\sigma_z \otimes \sigma_x + t_y \sigma_0 \otimes \sigma_x \\ &= \begin{pmatrix} h^{\uparrow} & 0 \\ 0 & h^{\downarrow} \end{pmatrix} \end{aligned} \tag{4.33}$$

where

$$h^{\uparrow,\downarrow} = \begin{pmatrix} 2t_x \cos(k) & t_y \mp 2t_{xy} \sin(k) \\ t_y \mp 2t_{xy} \sin(k) & -2t_x \cos(k) \end{pmatrix}$$

After transforming Hamiltonian under $(\sigma_0 \otimes U)$, where U is given by Eq. (4.29),

$$\mathcal{H}_T(k) = (\sigma_0 \otimes U)^{\dagger} \, \mathcal{H}(k) \, (\sigma_0 \otimes U) = \begin{pmatrix} h_T^{\uparrow} & 0 \\ 0 & h_T^{\downarrow} \end{pmatrix} \tag{4.34}$$

where $h_T^{\uparrow} = \begin{pmatrix} 0 & q_1 \\ q_1^{\dagger} & 0 \end{pmatrix}$ and $h_T^{\downarrow} = \begin{pmatrix} 0 & q_2 \\ q_2^{\dagger} & 0 \end{pmatrix}$ while

$$\begin{aligned} q_1 &= 2t_x \cos(k) - i(t_y - 2t_{xy} \sin(k)) \\ q_2 &= 2t_x \cos(k) - i(t_y + 2t_{xy} \sin(k)). \end{aligned} \tag{4.35}$$

Notice that our 4×4 Hamiltonian is simply two independent Creutz models. The overall winding number will be the sum of the winding number of each Creutz model, the two possible values therefore are minus two or zero, depending on whether the point $z = -it_y/2$ falls inside or outside the ellipse defined by the Brillouin zone, respectively.

The fundamental group corresponding to topological index of the Hamiltonian of each spin channel is $\mathbb{Z}$. The space of $\mathcal{H}_T$ is decomposed into direct sum of subspaces of $h^{\uparrow}$ and $h^{\downarrow}$:

$$\mathcal{H}_T = h^{\uparrow} \oplus h^{\downarrow}, \tag{4.36}$$

hence, the fundamental group representation of topological index can be written as sum of fundamental groups of two subspaces,

$$2\mathbb{Z} = \mathbb{Z} + \mathbb{Z} \tag{4.37}$$

which is consistent with symmetry analysis outcome.

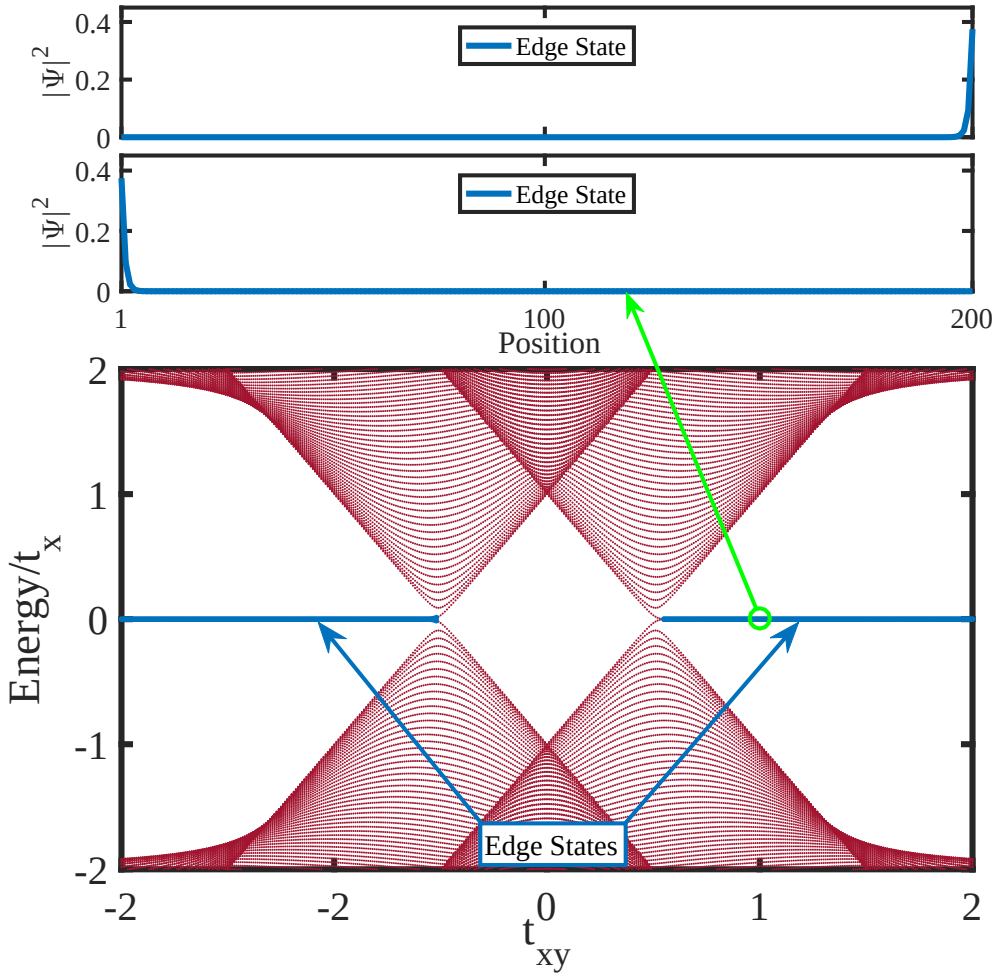

Figure 4.8: Energy spectrum of the shifted Creutz model with 200 sites, open boundary conditions as a function of t_{xy}. The parameters are $t_x = 1$ and $t_y = 1$. The blue lines indicate states which are not present when periodic boundary conditions are applied. The square magnitude of these states are shown in the upper panels. They are localized near the edges of the chain.

4.2.2 Středa-Widom formula for quantum spin Hall systems

In the case of the QH effect, a very useful [117, 32] formula was derived by Středa [115] via quantum transport equations, and also by Widom [116] via thermodynamic Maxwell relations. The generalization to the QSH effect, similar to the Středa approach, was done by Yang and Chang [118]. Here we attempt to derive this via Widom's thermodynamic considerations.

As a starting point, we take the view that a topological insulator consists of two magnets of opposite polarization for each spin. We also invoke a spin-dependent magnetic field, and a corresponding spin-dependent vector potential, $\mathbf{B}_\sigma$ and $\mathbf{A}_\sigma$, respectively. Such a procedure was recently applied by Dyrdal *et al.* [119] to calculate the properties of a two-dimensional electron gas with Rashba spin-orbit coupling. Under the first assumption the spin current can be written as

$$\mathbf{J}_{SH} = c\nabla \times [\mathbf{M}_\uparrow - \mathbf{M}_\downarrow] \,. \tag{4.38}$$

We can derive the electric field from the chemical potential as $\mathbf{E} = \nabla(\mu/e)$, we can write the spin current as

$$\mathbf{J}_{SH} = (ec)\mathbf{E} \times \frac{\partial}{\partial \mu} [\mathbf{M}_\uparrow - \mathbf{M}_\downarrow] \,. \tag{4.39}$$

We can apply the Maxwell relation and arrive at

$$\mathbf{J}_{SH} = \mathbf{E} \times \left[\frac{\partial (nec)}{\partial \mathbf{B}_\uparrow} - \frac{\partial (nec)}{\partial \mathbf{B}_\downarrow}, \right] . \tag{4.40}$$

resulting in a QSH conductivity of

$$\sigma_{SH} = ec \left[\frac{\partial n}{\partial B_\uparrow} - \frac{\partial n}{\partial B_\downarrow} \right]_\mu , \tag{4.41}$$

where we took the magnetic fields for both spins to be pointing perpendicular to the plane (justifying the neglect of tensor notation). We can rewrite this expression in terms of particle number and magnetic flux as

$$\sigma_{SH} = \left[\frac{\partial \nu}{\partial \Phi_\uparrow} - \frac{\partial \nu}{\partial \Phi_\downarrow} \right]_\mu . \tag{4.42}$$

This expression points to a definite procedure to calculate σ_{SH}; calculate the Fermi level in the absence of flux, then introduce a spin-dependent flux quantum, and count the number of particles which cross the Fermi level. In our approximate implementation, we use equal and opposite flux for the different spin channels on the t_{xy} bonds. Following Dyrdal *et al.* [119] we neglect the effect of the spin-dependent vector potentials on the Rashba spin-orbit coupling term.

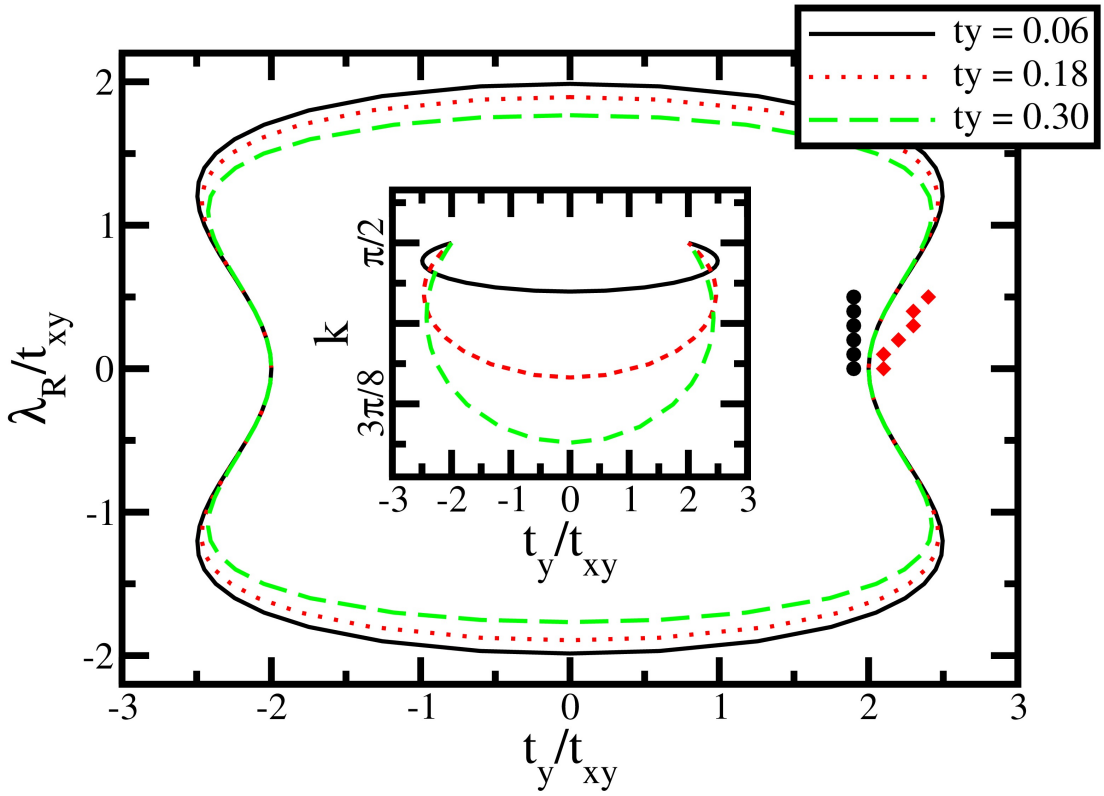

Figure 4.9: Main figure: phase diagram for systems with $t_x = 1, t_{xy} = 0.06, 0.12, 0.18$ in the t_y vs. λ_R plane. The inset indicates the k vector at which gap closure occurs as a function of t_y/t_{xy}. The black filled circles and red filled diamonds on the left side of the phase diagram indicate systems for which we have tested our Středa-Widom formula. For the black filled circles we found a quantized quantum spin Hall response, while we found no response for the red diamonds.

4.2.3 Results of Kane-Mele-like model

The gap in the band structure of the shifted Creutz model closes at $k = -\pi/2$ and $\pi/2$ depending on whether $t_y = 2t_{xy}$ or $t_y = -2t_{xy}$. When the boundary conditions are open edge states are found as shown in the shifted Creutz model (Fig. 4.8). The combination of two shifted Creutz models, one for each spin, restore time reversal invariance with gap closures at $k = \pm\frac{\pi}{2}$. Obviously, this system will also exhibit edge states.

Turning on the Rashba coupling term gives rise to a phase diagram shown in Fig. 4.9 for three cases. The plots are based on a calculation in which $t_x = 1$, $t_{xy} = 0.03, 0.18$ and 0.30. The phase diagram in the λ_R/t_{xy} vs. t_y/t_{xy} is shown for these three cases. The topological phase is the one which includes the origin, outside of this region the phase is trivial. The lines indicate where gap closure occurs. Along the phase boundary the system becomes an ideal conductor with a finite Drude weight. The inset shows the absolute value of the k points at which the gap closure occurs as a function of t_y/t_{xy}.

We also studied the quantized transport properties of the models, based on the approximate implementation of the result in Eq. (4.41). For no Rashba coupling we find that the trivial phase exhibits no σ_{SH} response, in other words, upon turning on the spin-dependent flux on the diagonal bonds leads to no change in the number of particles below the Fermi level. In the topological phase, the flux decreases the number of particles under the Fermi level by two. For small values of the Rashba coupling $\lambda_R \approx 0.5t_{xy}$ we find the same. In Fig. 4.9 we indicate the points at which we made calculations (black filled circles and red filled diamonds). At larger values of λ_R our approximations appear to break down. However, we emphasize that the topological region is adiabatically connected to the $\lambda_R = 0$ region and is therefore the same quantum phase (also characterized by the $2\mathbb{Z}$ winding number derived above).

Chapter 5

Enhanced charge transport at the ideal-conductor/insulator interface

Recently it was shown [120] that the Drude weight, the quantity sensitive to ideal conduction, can also be cast in terms of a topological invariant. The invariant of the Drude weight is different from the ones which appear in the above examples: it is an integral over a rectangle formed by the total position and the total momentum, rather than the band structure. However, the argument leading to current carrying edge states, namely that the topological invariant has to be "cut" at an interface between two systems with different values for the invariant appears to be still valid. The question which arises is: can one expect unusual transport properties at such interfaces, similar to topological insulators?

In this chapter this question is investigated. Our approach here is phenomenological. We consider a system with an interface on a square lattice: on one side of the interface the Hamiltonian consists only of nearest neighbor hopping (tight-binding), on the other nearest neighbor hopping plus an alternating on-site potential. The former is a simple ideal conductor with a Drude weight proportional to the kinetic energy (which is the maximum value the Drude weight can

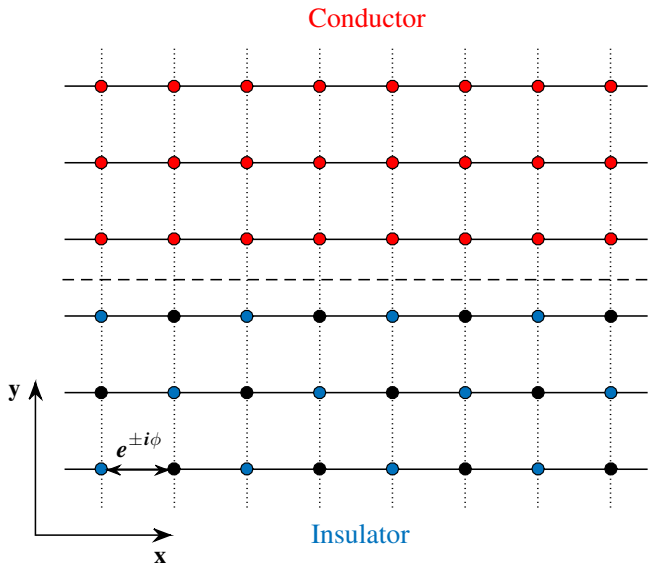

Figure 5.1: Schematic view of the lattice model studied in this thesis. The upper half is a simple tight-binding model (ideal conductor) the lower half is a band-insulator. The dashed line indicates an interface.

take). At half-filling, the latter system is a gapped insulator with a Drude weight of zero. We investigate the electronic structure and the transport properties of this system at half-filling with particular attention to the interface.

The band structure as a function of momentum in the direction parallel to the interface shows states in the gap, and one-dimensional band-crossings at the Fermi level at half-filling. We also calculate the kinetic energy, the spread of the total momentum, and the Drude weight along different lines of bonds which run parallel to the interface. We find that the kinetic energy and the Drude weight is sharply peaked in the line of bonds at the interface, and both quantities decrease at lines which are far from it. The spread in total momentum is minimum at the interface. These results suggest that charge transport is enhanced at the interface between an ideal conductor and an insulator. We interpret this as phenomenological evidence for topological behavior at a conductor insulator interface.

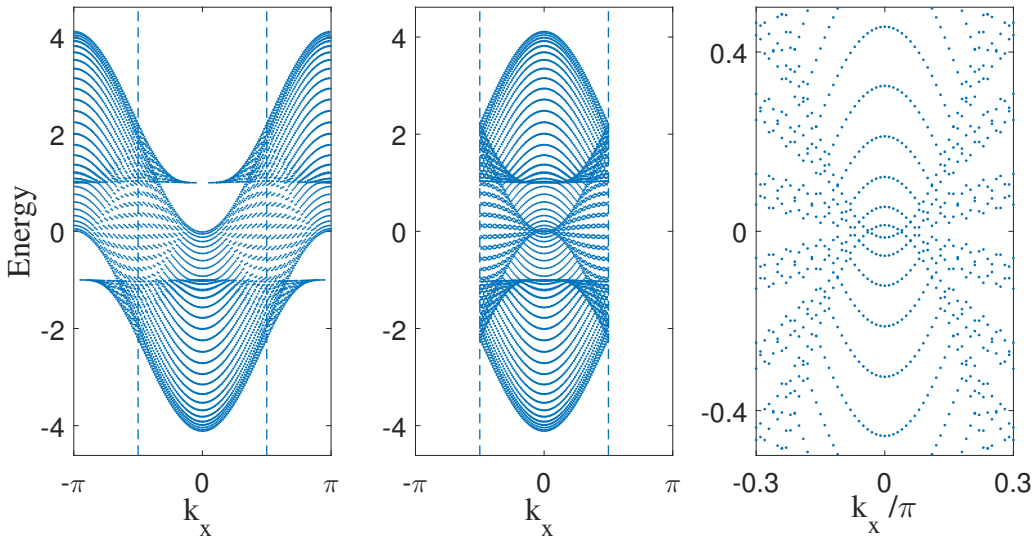

Figure 5.2: Band structure of the model with $U = 1$ as a function of k_x. The lattice is bipartite in the x-direction, the Brillouin zone in this direction is halved (restricted Brillouin zone). The left side is the raw data, the center plot is the data in the restricted Brillouin zone, the right shows the band structure zoomed to near the Fermi level at half-filling.

5.1 The Drude weight as a topological invariant

It was recently shown that the transport coefficient of ideal conduction, the Drude weight, can be expressed in terms of a topological invariant. This suggests that an interface between an ideal conductor and an insulator, across which the topological invariant abruptly changes its value, should exhibit topological edge states. For this derivation [120] we start with a one-dimensional system of N identical particles with Hamiltonian

$$\hat{H}(\Phi) = \sum_{j=1}^{N} \frac{(\hat{p}_j + \Phi)^2}{2m} + V(\hat{x}_1, ..., \hat{x}_N). \tag{5.1}$$

Φ denotes an external perturbation. We assume periodic boundary conditions, $\Psi(..., x_j, ...) = \Psi(..., x_j + L, ...)$.

Kohn [87] defined the Drude weight, the criterion for conduction, as

$$D = \left.\frac{\partial^2 E(\Phi)}{\partial \Phi^2}\right|_{\Phi=0}, \tag{5.2}$$

where $E(\Phi)$ denotes the ground state energy of the system. The first of derivative of the ground state energy with respect to Φ is the current,

$$J(\Phi) = \frac{\partial E(\Phi)}{\partial \Phi}. \tag{5.3}$$

Writing the ground state energy as $E(\Phi) = \langle \Psi(\Phi)|\hat{H}(\Phi)|\Psi(\Phi)\rangle$, the current becomes

$$J(\Phi) = \frac{N\Phi}{m} + \sum_{j=1}^{N} \langle \Psi(\Phi)|\frac{\hat{p}_j}{m}|\Psi(\Phi)\rangle. \tag{5.4}$$

At this point, we can write the momentum operators in the coordinate representation as

$$\hat{p}_j = i\frac{\partial}{\partial x_j}. \tag{5.5}$$

The sum over momenta acting on the ground state wavefunction can be rewritten as the total momentum acting on the same wavefunction. Consider the wavefunction $\Psi(x_1 + X, ..., x_N + X)$. In this case we have

$$i\sum_{j=1}^{N} \frac{\partial}{\partial x_j}\Psi(x_1, ..., x_N) = i\,\frac{\partial}{\partial X}\Psi(x_1 + X, ..., x_N + X)\Big|_{X=0}. \tag{5.6}$$

We can average the total momentum over the unit cell, resulting in

$$J(\Phi) = \frac{N\Phi}{m} + \frac{i}{mL}\int_0^L dX \langle \Psi(\Phi)|\frac{\partial}{\partial X}|\Psi(\Phi)\rangle. \tag{5.7}$$

Taking the derivative with respect to Φ, associating Φ with the crystal momentum (a shift in Φ corresponds to a shift in the crystal momentum), and averaging over the Brillouin zone, we obtain

$$D = \frac{N}{m} + \frac{i}{m2\pi}\int_{-\pi/L}^{\pi/L}\int_0^L dX dK[\langle \partial_K \Psi|\partial_X \Psi\rangle - \langle \partial_X \Psi|\partial_K \Psi\rangle]. \tag{5.8}$$

The second term in this equation is an integral over a curvature. Its form is very similar to the well-known TKNN invariant [8], which corresponds to the Hall conductance, and is quantized in quantum Hall system.

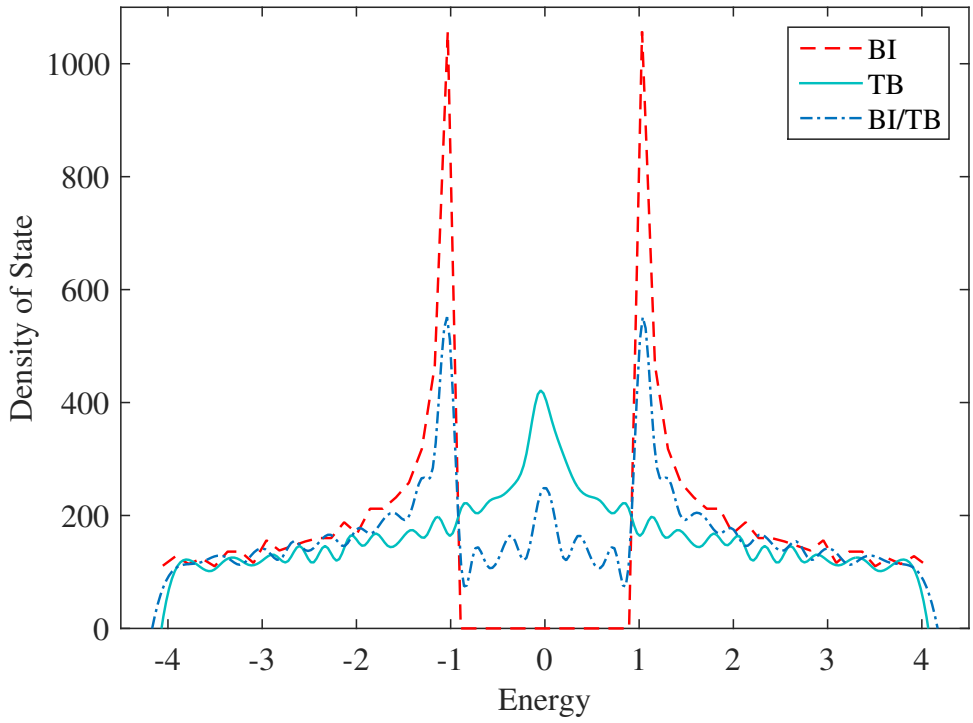

Figure 5.3: Density of states for crystalline insulator, tight-binding, and model with an interface between the two ($U = 1$). The crystalline insulator is gapped, the system with interface is not gapped, but the density is smaller near $E = 0$ than in the tight-binding system.

5.2 Model: The ideal-conductor/insulator interface

The models we study are based on the following Hamiltonians. One is the tight-binding Hamiltonian

$$\hat{H}_{TB} = -t \sum_{x,y} (c^{\dagger}_{x,y} c_{x+1,y} + c^{\dagger}_{x,y} c_{x,y+1} + \text{H. c.}) \tag{5.9}$$

and the band-insulator (BI) Hamiltonian,

$$\hat{H}_{BI} = \hat{H}_{TB} + \hat{H}_U, \tag{5.10}$$

with

$$\hat{H}_U = U \sum_{x,y}^{N} (-1)^{x+y} n_{x,y}, \tag{5.11}$$

in two-dimensions on a square lattice. In Eqs. (5.9) and (5.10) $n_{x,y} = c^{\dagger}_{x,y} c_{x,y}$ are number operators, $c^{\dagger}_{x,y}(c_{x,y})$ are creation(annihilation operators) at position x, y on the lattice. The on-site potential term $\hat{H}_U$ alternates in a checkerboard pattern from site to site. To study the properties of the conductor-insulator interface, we study two models. One is the tight-binding model with periodic boundary conditions in the x-direction and open boundary conditions in the y-direction. We also study a two-dimensional lattice model, part of which is described by the tight-binding Hamiltonian (Eq. (5.9)), part of it by the band-insulator (Eq. (5.10)), with two interfaces between the two. Periodic boundary conditions are assumed in both directions. Figure 5.1 shows a schematic view of the model. The Hamiltonian is quadratic, and the solution of the model can be obtained by numerical diagonalization. We study the system at half filling. Apart from this model we also study a TB model extended in the x-direction, and applying open and periodic boundary conditions in the y-direction. We have also checked an interface between an Anderson localized insulator and a TB model.

Figure 5.2 shows the band structure of the system for the case $U = 1$. In the x-direction (Figure 5.1) the lattice is bi-partite, therefore the Brillouin zone is halved in this direction (restricted Brillouin zone $-\pi/2, \pi/2$). The band structure for the insulating system is gapped, with a gap proportional to U. The band structure of the model with the interface shows band crossings at the Fermi level (zoomed figure on the right) somewhat reminiscent of the band structure of the Su-Schrieffer-Heeger model [88]. The crossings are definitely due to the presence of the interface. Figure 5.3 shows the density of states. At the Fermi level, the density of states for the system with an interface is smaller than for the pure TB model.

5.3 Results

In Figure 5.4 the kinetic energy resolved to bonds parallel to the interface is shown. The variable y is the y-coordinate of the set of bonds (according to Figure 5.1) whose kinetic energy contribution is considered. The left half of the

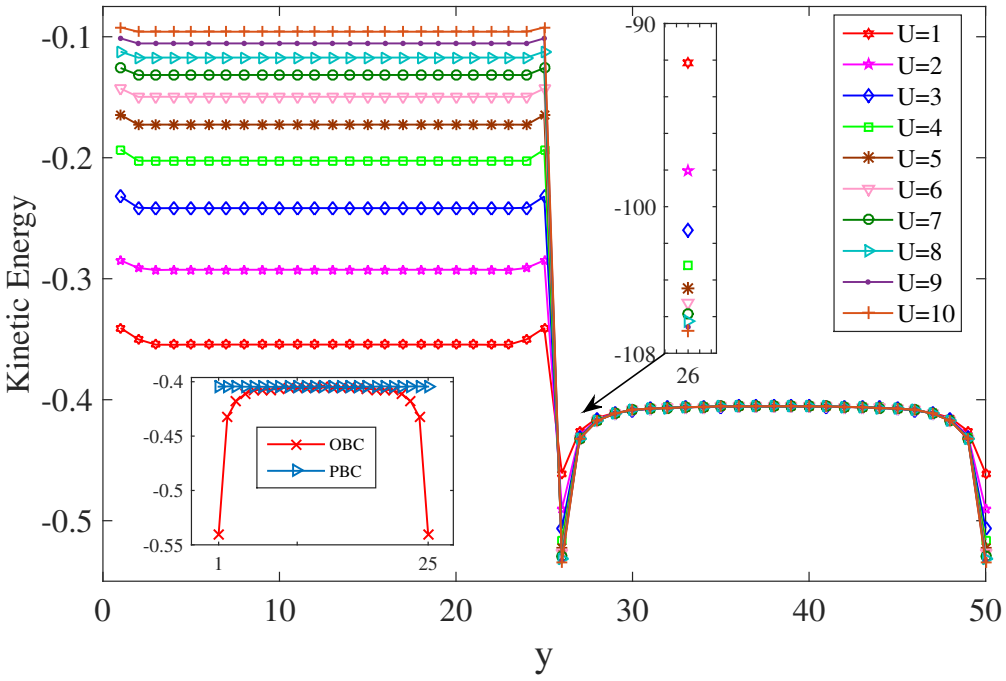

Figure 5.4: Kinetic energy resolved to bonds parallel to the interface for different values of U. The variable y indicates the y-coordinate of the bonds according to Figure 5.1. Clearly, the kinetic energy is peaked (in the negative direction) at the interface.The inset shows the value of the kinetic energy for bonds running along the interface for different values of U. The size of the systems studies is 50×200.

Figure corresponds to the insulating part of the model, the right to the conducting part. We see that as U is increased, the absolute value of the kinetic energy on the insulating side decreases. On the conducting side the absolute value of the kinetic energy is larger than on the insulating side. The absolute value of the kinetic energy is sharply peaked at the interfaces on the conducting side. As U is increased the value of this peak kinetic energy (its absolute value) increases, and it approaches a maximum asymptotically. The inset shows the same results for a simple TB model with open or periodic boundary conditions. The kinetic energy again peaks at bonds along the edge of the system.

The peak of the kinetic energy alone does not necessarily indicate enhanced transport. In Figure 5.5 the Drude weight, resolved to lines of bonds parallel to the interface, as was done for the kinetic energy, are shown. In this calculation, first the wavefunctions in two-dimensional real space $\Psi_i(x, y)$ were obtained.

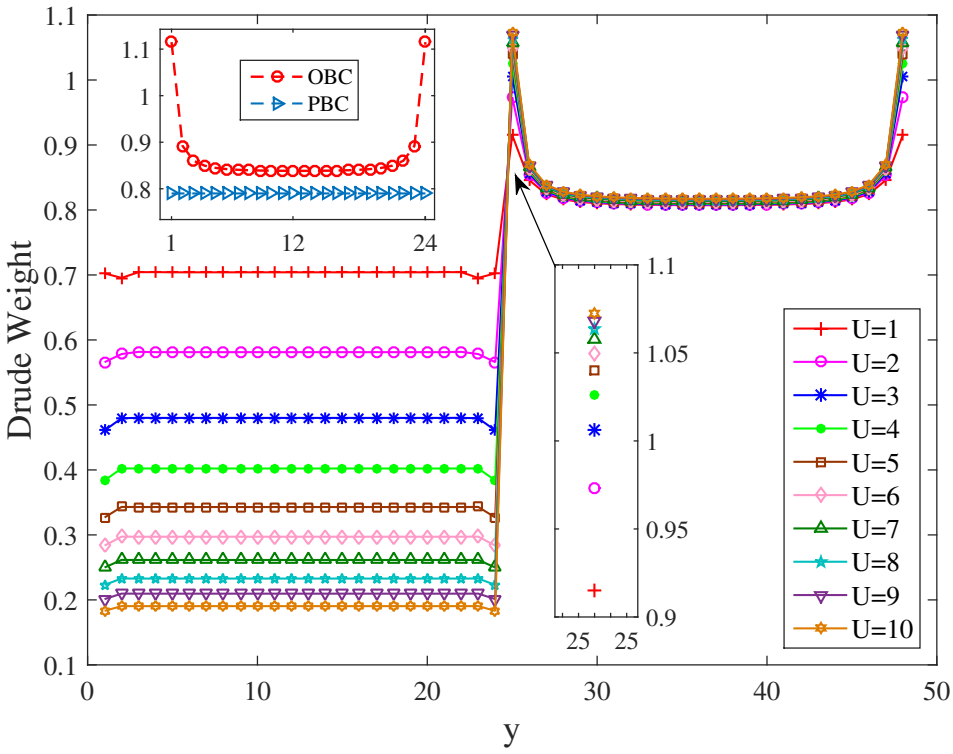

Figure 5.5: The Drude weight (resolved to bonds along the y direction) as a function of y coordinate for different values of the strength of the external potential U. The Drude weight is peaked at the interface. The left inset shows the resolved Drude weight for a tight-binding model with periodic and open boundary conditions. The right inset shows the value of the Drude weight for the interface. The Drude weight is peaked at the interface. The value at the peak increases as a function of U. The size of the systems is 48×200.

Subsequently, a Fourier transform was applied to the x variable, resulting in the functions $\Phi_i(k, y)$. From these functions the current resolved to bonds with a given value of y is given by

$$J = \sum_i \tilde{n}_i(k, y) \sin(k). \tag{5.12}$$

We apply a Peierls phase Φ and obtain the y-resolved Drude weight via a finite difference estimation for small Φ.

The y-resolved Drude weight is shown in Figure 5.5. Due to the small system size the insulating part of the system does not show truly insulating behavior

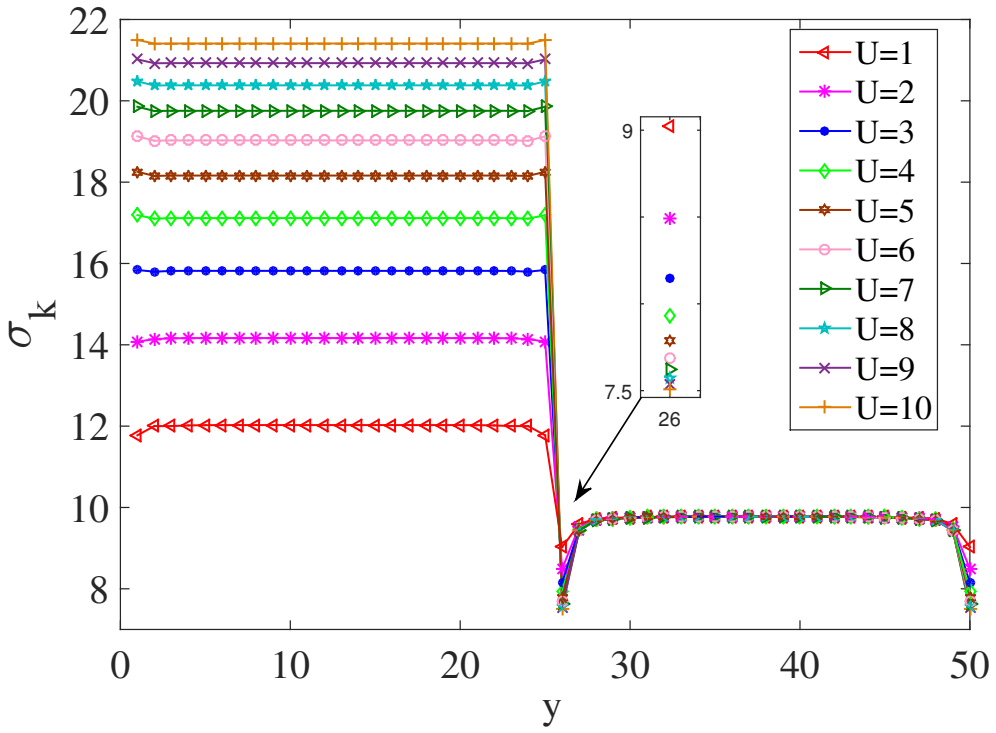

Figure 5.6: Spread in the total momentum resolved as a function of y coordinate for different values of the strength of the external potential. The spread in the total momentum is minimized at the interface. The size of the systems studied was 50×200.

($D = 0$), but as U is increased, transport is definitely suppressed. Also, the resolved Drude weight shows a peak in the conducting part. Away from the boundary a finite Drude weight is obtained in the conducting half, which is independent of the on-site potential strength (U). In the inset, it is shown that as U is increased the resolved Drude weight increases, even if slightly. It is interesting that transport is enhanced more at the boundary, when U increases, in other words, as the insulating half becomes more insulating. For comparison we include a simple conducting system with periodic boundary conditions both in the x and y direction (squares on right-half of the figure), as well as one with open boundary conditions in the y-direction. It is interesting that the peak value of the Drude weight is larger than that of the pure conducting system. The system with open boundary conditions indicates the same behavior as the model with the interface.

In Ref. [120] it was shown that the spread in momentum is also indicative of conduction. In the extreme case, if a wavefunction is an eigenstate of the total momentum, the spread of the total momentum is zero, and it exhibits a finite Drude weight. One can relate this situation to the spread in total position [37, 44] suggested as a criterion for conduction. The spread in total position is infinite for a wavefunction which is an eigenstate of the total momentum. The total momentum and its relation to transport (superfluidity) is also actively being investigated [121, 122]. The y-resolved spread in total momentum is shown in Figure 5.6. In this case the spread is maximized in the insulating side of the model, it is smaller on the conducting side, and the minima occur at the edges of the conducting half, indicating that the system is closest to an ideal conductor at the interface.

We have also calculated the properties of the interface between an Anderson localized system and a simple TB model. We have made the same calculations for this system as for the TB-CI interface. We have found the same patterns we have identified above, namely, an enhancement of transport at the interface, which increases monotonically as a function of the strength of the external potential in the insulating phase.

Chapter 6

Topological phase transition in a generalized Aubry-André-Harper system with p-wave superconductivity

With recent experimental developments and the realization of the 1D Aubry-André-Harper (AAH) model in ultracold atoms [123, 124] and photonic crystals [125, 12], dynamics of particles in 1D quasiperiodic lattices has gained attention. The important point to be emphasized in the 1D AAH model is that this model can be mapped exactly to 2D Harper-Hofstadter model [13, 14]. This link between the 2D Harper-Hofstadter and 1D Aubry-André model implies that the Aubry-André model must have topologically protected modes similar to the 2D quantum Hall system on a lattice (Hosftadter model). Recent experiment [15], realized this topological edge state. In this chapter, motivated by the recent proposals of simulating GAAH model [**?**, 126, 127, 17, 128], we focus on the incommensurate and commensurate off-diagonal GAAH model with the next-nearest-neighbor p-wave SC pairing. We extend the 1D GAAH model to an "ancestor" 2D p-wave SC model. This 2D model same as the 1D model is topologically nontrivial and equivalent. The hopping amplitude, SC pairing, and on-site potential

are modulated by different cosine functions with periodicity $1/\beta$. In our model, the modulated SC pairing term leads to a more complicated phase diagram. Here we investigate the interplay between the modulated p-wave SC pairing and other parameters which leads to a rich zero-temperature quantum phase diagram. Our phase diagram demonstrates different distinct phases: the topologically-trivial phase and the topologically-nontrivial phase. In the incommensurate lattice when β is irrational, we find that transition from the delocalized state to localized state as a function of the modulated p-wave SC pairing strength beyond some critical value close to half-filling. On the other hand, in the commensurate lattice, we investigate the Chern numbers of the main gaps during the change of the modulated p-wave SC pairing strength. We find that value of Chern numbers are changing with and without on-site potential when we tune the modulated p-wave SC pairing strength. More specifically, as the modulated p-wave SC pairing strength change, the energy spectrum alters from the triangular-lattice like Hofstadter butterfly to square-lattice like Hofstadter butterfly.

6.1 Generalized Aubry-André-Harper model

In this section, we consider the generalized one-dimensional Aubry-André-Harper model with p-wave SC pairing, described by the following Hamiltonian

$$\begin{aligned}\hat{H} = &-\sum_j \Big[(t+\tau_j)c_j^\dagger c_{j+1} + \text{H.c.})\Big] \\ &+\sum_j (\Delta+\delta_j)c_j^\dagger c_{j+1}^\dagger + \text{H.c.}) + \sum_j V_j \hat{n}_j\end{aligned} \tag{6.1}$$

where

$$\begin{cases}\tau_j = \tau\cos(2\pi\beta j + \phi_\tau), \\ \delta_j = \delta\cos(2\pi\beta j + \phi_\delta), \\ V_j = V\cos(2\pi\beta j + \phi_V).\end{cases} \tag{6.2}$$

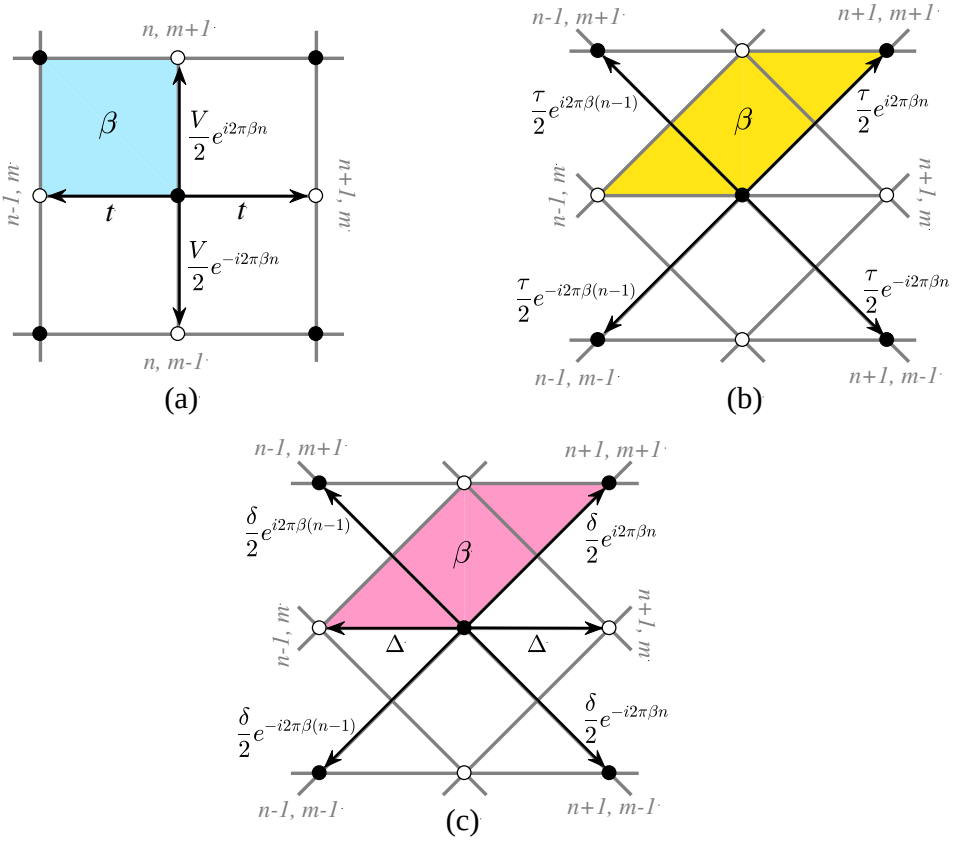

Figure 6.1: Graphical presentations of extended 1d GAAH with nearest and next-nearest hopping (SC pairing) and on-site potential to a 2D Hamiltonian. In the presence of a perpendicular magnetic field with β flux quantum per unit cell, the electrons hop on a rectangular lattice. (a) This is the 2D "ancestor" of the diagonal GAAH model which the hopping is to nearest neighbors, (b) This is the 2D "ancestor" of the off-diagonal GAAH model which the hopping is to next-nearest neighbors, and (c) This is the 2D "ancestor" of the SC pairing of GAAH model which the hopping is to nearest and next nearest neighbors. Each rectangular plaquettes which demonstrated by different color are pierced by β flux quantum.

here τ_j is commensurate (incommensurate) hopping modulations with periodicity $1/\beta$ and phase factor ϕ_τ, and V_j is the diagonal Aubry-André potential with periodicity $1/\beta$ and phase factor ϕ_V, respectively. The corresponding hopping modulation amplitude is set by τ, and V is the on-site potential strength.

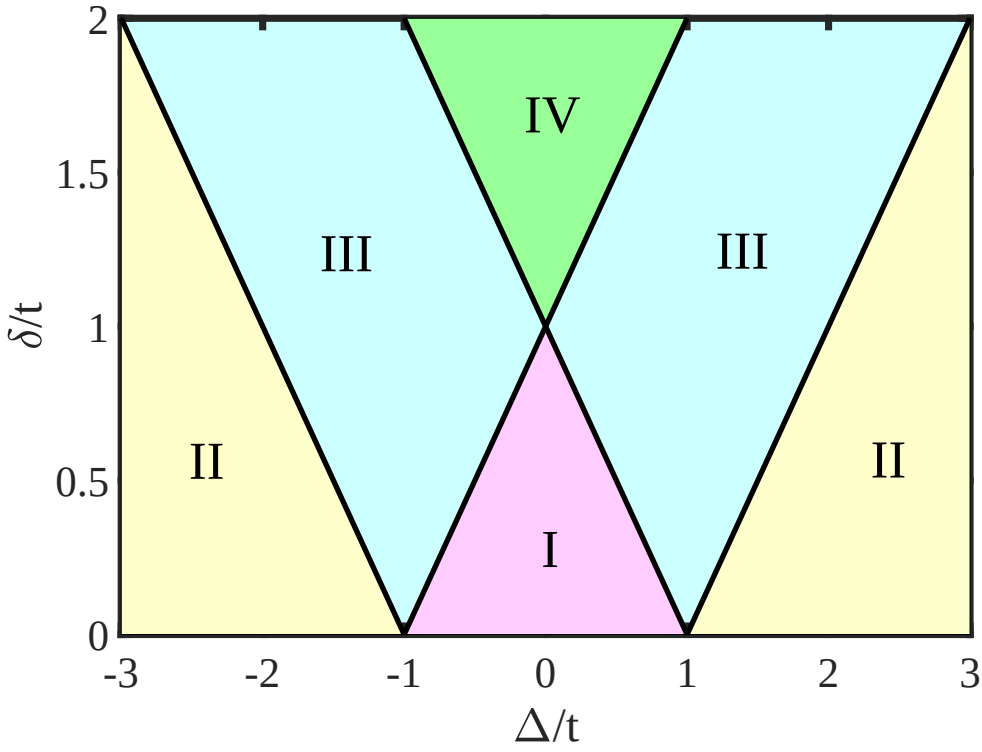

Figure 6.2: Phase diagram of the off-diagonal GAAH model with the p-wave incommensurate modulation amplitude δ and the p-wave pairing strength Δ. The hopping incommensurate modulation amplitude is set to $\tau = 0$ and the phase in the incommensurate modulation is set to $k_y = \pi/2$ and $\varphi = \beta\pi$. The phases are (I and II) extended phases, (III) the mobility-edge phase, and (IV) critical phase.

$\hat{n}_j = c_j^\dagger c_j$ are number operators, $c_j^\dagger(c_j)$ are creation (annihilation operators) at position j on the lattice, and t is the hopping (or tunneling) amplitudes to the nearest neighbors and set to be the unit of the energy ($t = 1$). Also, δ_j is a SC modulation with periodicity $1/\beta$ and phase factor ϕ_δ. Here δ and Δ are the strength of SC pairing gap which is taken to be real.

In the limit $\Delta = \delta = 0$, this model reduces to the generalized Aubry-André-Harper model introduced by Ganeshan *et al.* [129]. If $\delta = 0$ and $\phi_\tau = \phi_V$, this model reduces to the GAAH model with p-wave SC pairing introduced in Ref. [17]. If we set $\tau = \delta = 0$, then the model exhibits an Anderson localization transition when $V > 2(t + \Delta)$ [130]. On the other hand, if Δ, and δ are zero, but

τ and V are finite, and when the relation between the hopping modulation and on-site phases are fixed, for example, $\phi_V = \phi_\tau + \beta\pi$, the GAA model can be formally derived from an ancestor 2D quantum Hall system on a lattice (Hofstadter model) with diagonal (next-nearestneighbor) hopping terms [131, 132, 15]. Here we keep our notations general with $\phi_\tau = \phi_\delta = k_y$ and $\phi_V = k_y + \varphi$ as independent variables. The off-diagonal modulation has an additional phase φ.

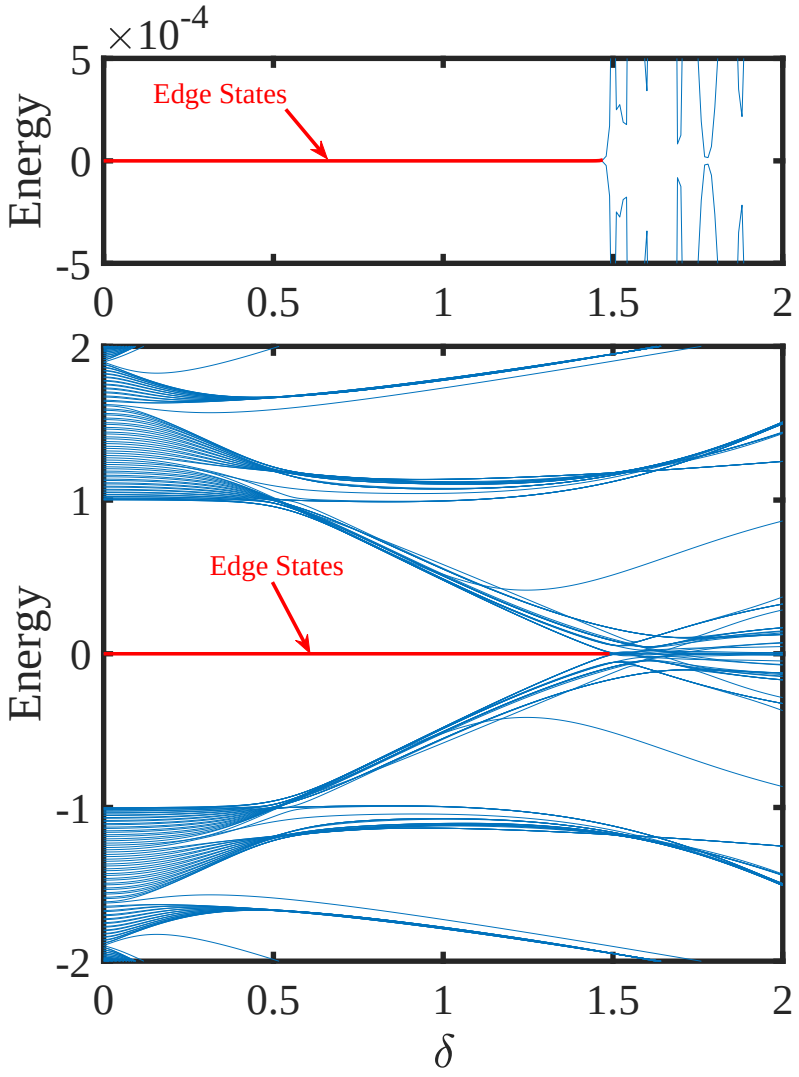

Figure 6.3: The energy spectrum of the off-diagonal GAAH model with p-wave pairing plotted as a function of δ under OBCs in the lattice dimension with 100 lattice sites. The model parameters are fixed at $\tau = 0$, $V = 0$, and $\Delta = 0.5$. Inside the regions I and II (see figure 6.2) edge states arise.

6.2 The corresponding 2D of GAAH model with p-wave SC

The Hamiltonian of the 1D GAAH model with p-wave superfluid pairing we consider in this thesis can be made to correspond to a 2D p-wave SC model. For any given k_y, the GAAH model of Eq. (6.1) can be viewed as the k_yth Fourier component of a general 2D Hamiltonian. On the other hand, k_y is the second degree of freedom, hence, we define the operator c_{n,k_y} that satisfies the following commutation relation

$$\{c_{n,k_y}, c^{\dagger}_{\acute{n},\acute{k_y}}\} = \delta_{n,\acute{n}}\delta_{k_y,\acute{k_y}} \tag{6.3}$$

Therefore the 2D Hamiltonian can be expressed in terms of $\hat{H}$ as

$$\hat{\mathcal{H}} = \frac{1}{2\pi}\int_0^{2\pi} \hat{H}(k_y)\, dk_y \tag{6.4}$$

where in the Hamiltonian of Eq. (6.1), we replaced the operators c_n with c_{n,k_y}. The corresponding Hamiltonian can be written as

$$\begin{aligned}\hat{H}(k_y) = &-\sum_n \Big[(t+\tau_n)c^{\dagger}_{n,k_y}c_{n+1,k_y} + \text{H.c.}\Big] \\ &+\sum_n \Big[(\Delta+\delta_n)c^{\dagger}_{n,k_y}c^{\dagger}_{n+1,-k_y} + \text{H.c.})\Big] \\ &+\sum_n V_n c^{\dagger}_{n,k_y}c_{n,k_y}\end{aligned} \tag{6.5}$$

Define the Fourier transform such that

$$c_{n,k_y} = \sum_m e^{-ik_y m}c_{n,m} \tag{6.6}$$

allows us to easily calculate 2D Hamiltonian as

$$\begin{aligned}\hat{\mathcal{H}} = &\sum_{n,m} -\left[tc^{\dagger}_{n,m}c_{n+1,m} + \text{H.c.}\right] \\ &-\left[\frac{\tau}{2}\left((e^{i2\pi\beta n}c^{\dagger}_{n,m}c_{n+1,m+1} + e^{-i2\pi\beta n}c^{\dagger}_{n,m}c_{n+1,m-1}\right) + \text{H.c.}\right] \\ &+\left[\frac{\delta}{2}\left(e^{i2\pi\beta n}c^{\dagger}_{n,m}c^{\dagger}_{n+1,m+1} + e^{-i2\pi\beta n}c^{\dagger}_{n,m}c^{\dagger}_{n+1,m-1}\right)\right. \\ &\left.+\Delta c_{n,m}c_{n+1,m} + \text{H.c.}\right] \\ &+\sum_{n,m}\frac{V}{2}\left[e^{i(2\pi\beta n+\varphi)}c^{\dagger}_{n,m}c_{n,m+1} + \text{H.c.}\right]\end{aligned} \tag{6.7}$$

In the limit $\varphi = 0$, the 2D system has isotropic next-nearest-neighbor hoppings and the corresponding 1D Hamiltonian has the same phase k_y in the off-diagonal and diagonal modulations. By introducing the following Majorana operators

$$c_{n,k_y} = \sum_m e^{-ik_y m}\gamma^A_{n,m} + ie^{-ik_y m}\gamma^B_{n,m} \tag{6.8}$$

which fulfill the relations $(\gamma^\alpha_i)^\dagger = \gamma^\alpha_i$ and anticommutation relations $\gamma^\alpha_i, \gamma^\beta_j = 2\delta_{ij}\delta_{\alpha\beta}$. The Hamiltonian of Eq. 6.1 can be rewritten as

$$\begin{aligned}
\hat{\mathcal{H}} = &-\sum_{n,m}\left[it\gamma^A_{n,m}\gamma^B_{n+1,m} - it\gamma^B_{n,m}\gamma^A_{n+1,m}\right] \\
&+\Big[\frac{\gamma}{2}e^{i2\pi\beta n}(\gamma^A_{n,m}\gamma^B_{n+1,m+1} - \gamma^B_{n,m}\gamma^A_{n+1,m+1}) \\
&+\frac{\gamma}{2}e^{-i2\pi\beta n}(\gamma^A_{n,m}\gamma^B_{n+1,m-1} - \gamma^B_{n,m}\gamma^A_{n+1,m-1}) \\
&+\Delta(\gamma^A_{n,m}\gamma^B_{n+1,m} + \gamma^B_{n,m}\gamma^A_{n+1,m}) \\
&+\frac{\delta}{2}\left[e^{i2\pi\gamma n}(\gamma^A_{n,m}\gamma^B_{n+1,m+1} + \gamma^B_{n,m}\gamma^A_{n+1,m+1})\right. \\
&\left.+e^{-i2\pi\gamma n}(\gamma^A_{n,m}\gamma^B_{n+1,m-1} + \gamma^B_{n,m}\gamma^A_{n+1,m-1}) + \text{H.c.}\right]\Big] \\
&+\sum_{n,m}\frac{V}{2}\left[e^{i2\pi\beta n}\gamma^A_{n,m}\gamma^B_{n,m+1} + e^{-i2\pi\beta n}\gamma^A_{n,m}\gamma^B_{n,m-1}\right]
\end{aligned} \tag{6.9}$$

This Hamiltonian describes Majorana chain on a 2D lattice in the presence of a uniform perpendicular magnetic field with β flux quantum per unit cell as shown in Fig. 6.1.

6.3 Incommensurate modulation case

When β is irrational, the lattice is incommensurate. We choose $\beta = (\sqrt{5}-1)/2$, the golden ratio, but all the conclusions can also be generalized to other incommensurate situations. In this thesis, for incommensurate modulation case, we shall study the interplay of the SC modulation pairing δ with the incommensurate hopping amplitude and potential, respectively, and then we determine the

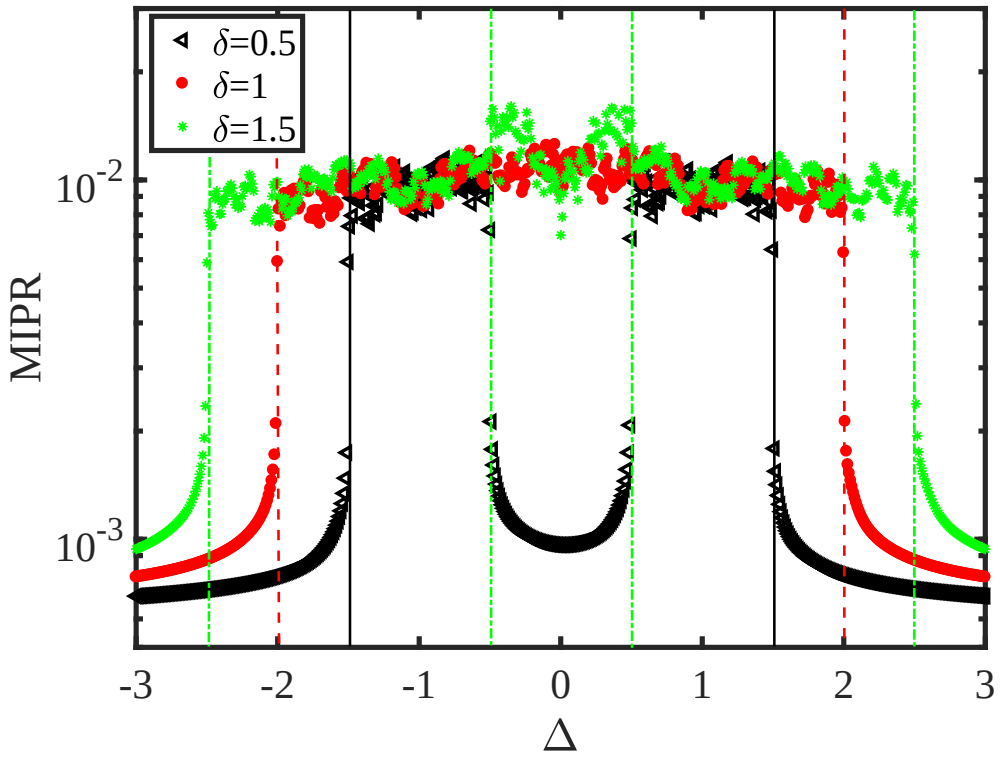

Figure 6.4: MIPR as a function of p-wave superfluid pairing Δ for the indicated values of modulation amplitude δ. The dashed lines, dot-dashed lines, and solid lines demonstrate the abrupt changes of the MIPR at phase boundaries.

phase diagram of the model. The Hamiltonian can be diagonalized by the Bogoliubov–de Gennes (BdG) transformation [133, 134]

$$\eta_n^\dagger = \sum_{j=1}^{L} [u_{n,j} c_j^\dagger + \nu_{n,j} c_j] \tag{6.10}$$

where $n = 1, \ldots L$, is the energy band index and $u_{n,j}$ and $\nu_{n,j}$ denote the two wavefunction components at the site j assumed to be real. On this basis the wave function of Hamiltonian becomes

$$|\Psi_n\rangle = \eta_n^\dagger |0\rangle = \sum_{j=1}^{L} [u_{n,j} c_j^\dagger + \nu_{n,j} c_j] |0\rangle \tag{6.11}$$

Then the Hamiltonian in Eq. (1) can be diagonalized in terms of the operators η_n and $\eta_n^\dagger$ as

$$\hat{H} = \sum_{n=1}^{L} \varepsilon_n (\eta_n^\dagger \eta_n - \frac{1}{2}) \tag{6.12}$$

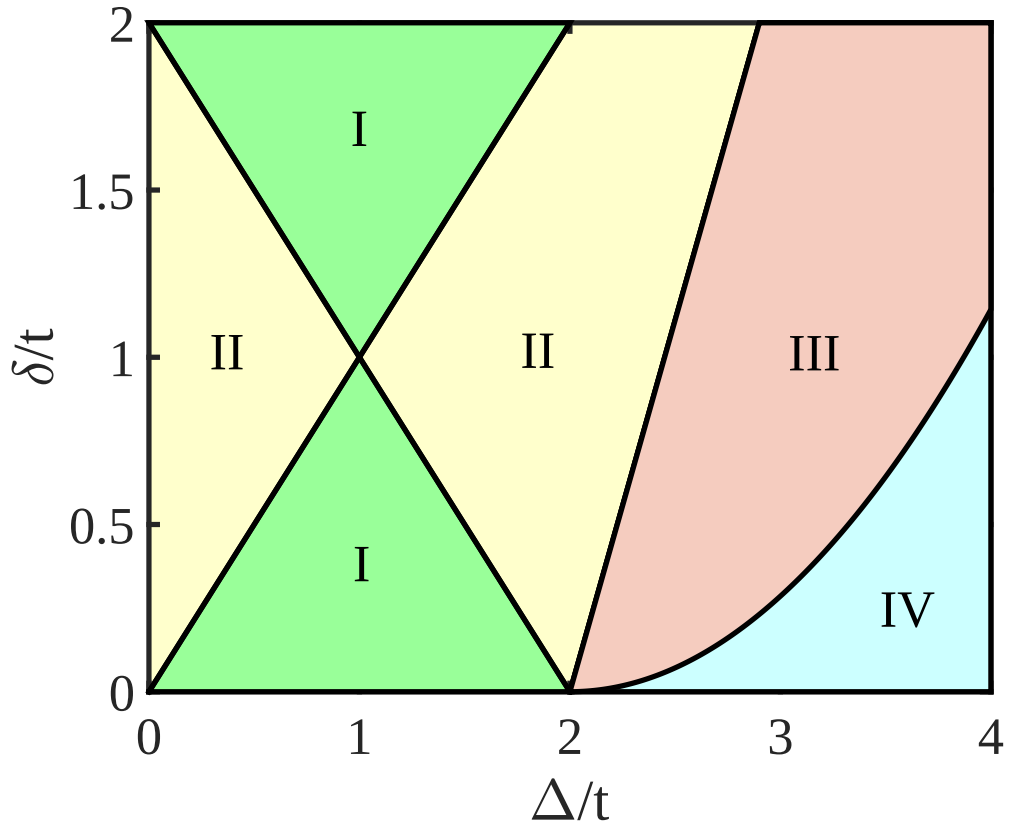

Figure 6.5: Phase diagram of the off-diagonal GAAH model with the p-wave incommensurate modulation amplitude $0 < \delta \leq 2$ and the p-wave pairing strength $0 \leq \Delta \leq 4$. The hopping incommensurate modulation amplitude is set to $\tau = 1$ and the phase in the incommensurate modulation is set to $k_y = \pi/2$ and $\varphi = \beta\pi$. The phases are (I) localized phase($|\delta - \tau|$), (II) critical localized phase, and (III) extended phases.

with ε_n being the spectrum of the single quasiparticles. The Schrödinger equation $H|\Psi_n\rangle = \varepsilon_n|\Psi_n\rangle$, can be written as

$$\begin{cases} -(t+\tau_{j-1})u_{n,j-1} + (\Delta+\delta_{j-1})\nu_{n,j-1} + V_j u_{n,j} - (t+\tau_j)u_{n,j+1} - (\Delta+\delta_j)\nu_{n,j+1} & = \varepsilon_n u_{n,j} \\ (t+\tau_{j-1})\nu_{n,j-1} - (\Delta+\delta_{j-1})u_{n,j-1} - V_j \nu_{n,j} + (t+\tau_j)\nu_{n,j+1} + (\Delta+\delta_j)u_{n,j+1} & = \varepsilon_n \nu_{n,j}. \end{cases} \tag{6.13}$$

Representing the wave function as

$$|\Psi_n\rangle = [u_{n,1}, \nu_{n,1}, u_{n,2}, \nu_{n,2}, \cdots, u_{n,L}, \nu_{n,L}]^T, \tag{6.14}$$

the H can be written as a $2L \times 2L$ matrix,

$$H_n = \begin{pmatrix} A_1 & B & 0 & \cdots & \cdots & \cdots & C \\ B^\dagger & A_2 & B & 0 & \cdots & \cdots & 0 \\ 0 & B^\dagger & A_3 & B & \cdots & \cdots & 0 \\ \vdots & \ddots & \ddots & \ddots & \ddots & \ddots & \vdots \\ 0 & \cdots & 0 & B^\dagger & A_{L-2} & B & 0 \\ 0 & \cdots & \cdots & 0 & B^\dagger & A_{L-1} & B \\ C^\dagger & \cdots & \cdots & \cdots & 0 & B^\dagger & A_L \end{pmatrix} \tag{6.15}$$

where

$$A_j = \begin{pmatrix} V_j & 0 \\ 0 & -V_j \end{pmatrix}, \tag{6.16}$$

$$B = \begin{pmatrix} -(t+\tau_j) & -(\Delta+\delta_j) \\ \Delta+\delta_j & t+\tau_j \end{pmatrix}, \tag{6.17}$$

and

$$C = \begin{pmatrix} -(t+\tau_{j+1}) & \Delta+\delta_{j+1} \\ -(\Delta+\delta_{j+1}) & t+\tau_{j+1} \end{pmatrix}, \tag{6.18}$$

Here we consider, a chain a length of L, in order to impose periodic boundary condition which implies that $c_{j+L} = c_j$. L should be a sufficiently large length because in this condition the irrational number β can be approximated by rational numbers [2]. It was argued that the for $\delta = 0$ when the lattice is made quasiperiodic by setting β to an irrational number, this model will demonstrate a phase transition from extended phases to localized phases, in our model, we may expect the same transition to show up. To characterize the phase transition of this incommensurate GAAH model with p-wave pairing, we need to calculate the mean inverse participation ratio (MIPR) which for a given normalized wave function ($\sum_{j=1}^{N}(u_{n,j}^2 + \nu_{n,j}^2) = 1$) is defined as [135, 136]

$$\text{MIPR} = \frac{1}{2N}\sum_{n=1}^{2N}\sum_{j=1}^{N}(u_{n,j}^4 + \nu_{n,j}^4) \tag{6.19}$$

where n is the index of energy levels and $u_{n,j}$ and $\nu_{n,j}$ are the solution to the BdG equations. It is well known that for an extended state, MIPR$\rightarrow \frac{1}{L}$ and the MIPR tends to zero in the thermodynamic limit (for large L), however, MIPR tends to

a finite value for a localized state even in thermodynamic limit. In the following, we will discuss different configurations of GAAH model with p-wave pairing for generic and off-diagonal cases by checking the MIPR to characterize the phase boundaries separating the localized, critical, and extended phases.

6.3.1 Off-diagonal GAAH model with p-wave pairing

The special case with $V = 0$ corresponds to the off-diagonal GAAH model with p-wave pairing. In order to demonstrate the phase transition of the off-diagonal GAAH model, we calculate the phase diagram as a function of the modulation strength of incommensurate p-wave pairing and modulation strength of incommensurate hopping. Here, we will mostly focus on the case $k_y = \pi/2$, and we choose $\varphi = \beta\pi$. This off-diagonal GAAH model in the limit $\Delta = 0$ and $\delta = 0$ exhibits nontrivial zero-energy edge modes [129, 126] and or in a large parameter space preserves the critical states [127]. Here, we find that the topological properties and localization of this system are profoundly affected by the existence of a nonzero δ. Based on MIPR, we constructed the phase diagram of the off-diagonal GAAH model with p-wave pairing (without hopping modulations and site-diagonal potential), shown in Fig. 6.2. The extended phase (regions I and II), the mobility-edge phase (region III) and critical phase (region IV) are separated by the black solid lines. For $0 < \delta < 1$, there are two regions which are in the extended phase. Regions I, II, and III hosting 2 zero-energy modes as a result of its nontrivial topology in the energy levels, hence only appearing for open boundary conditions. Also, as shown in Fig. 6.3, the region IV is topologically trivial and the edge modes (indicated in red color in the figure), in the regions I and III are found to be very robust. One should notice that edge states in this model actually happen in the case of off-diagonal disorder when $\tau = 0$ and in principle survive after the model undergo Anderson-like localization.

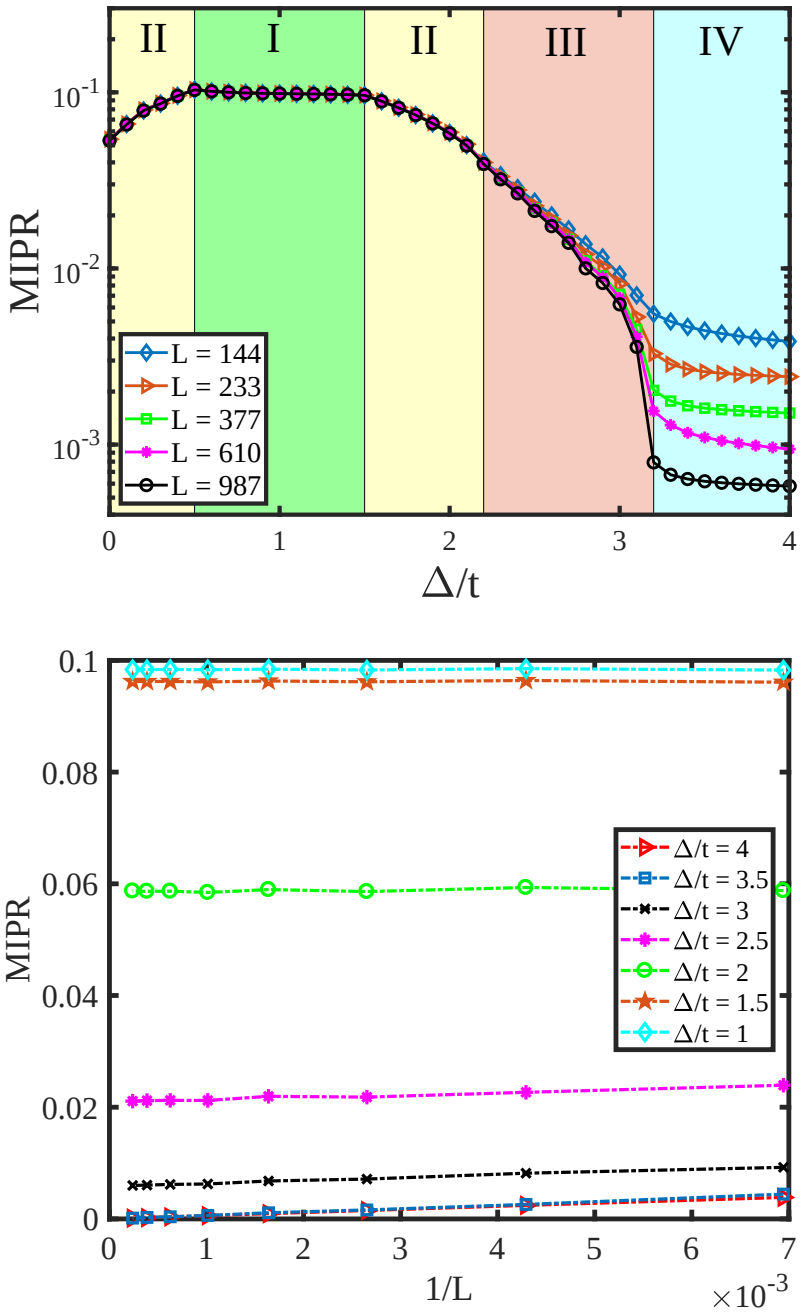

Figure 6.6: Uupper panel: MIPR (log-scale) as a function of p-wave superfluid pairing Δ/t for different chain lengths L for $\tau = 1$ and $\delta/t = 0.5$. Bottom panel: MIPR with the inverse system size $1/L$. For the extended phase, MIPR tends to zero as L increases.

Figure 6.4 demonstrates the evolution of the MIPR on a logarithmic scale at three values of $\delta = 0.5$, 1, and 1.5. We find that the MIPR changes abruptly from one phase to another phase as a function of Δ and δ. Also, there are four turning points and have found that the change of MIPR at these points becomes sharper with increasing system size L (results not shown). Thus, in the thermodynamic limit $L \to \infty$, we expected a discontinuity at the turning points, signaling a phase transition among the mobility-edge, the extended, and the critical phases.

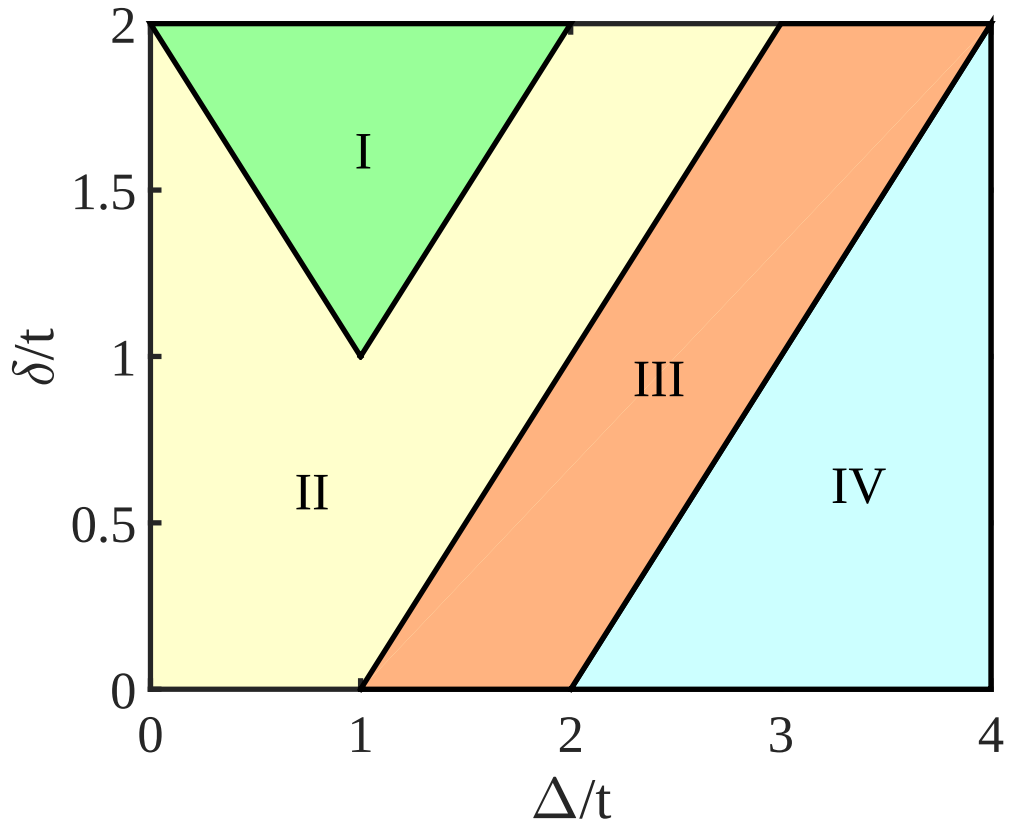

Figure 6.7: Phase diagram of the generic GAAH model with the p-wave incommensurate modulation amplitude $0 < \delta \leq 2$ and the p-wave pairing strength $0 \leq \Delta \leq 4$. The hopping incommensurate modulation amplitude is set to $\tau = 1$, the on-site potential incommensurate modulation amplitude is set to $V/t = 1$, and the phase in the incommensurate modulation is set to $k_y = \pi/2$ and $\varphi = \beta\pi$. The phases are (I) localized phase, (II) critical localized phase, (III) critical extended phases, (IV) extended phases.

We have also considered the dependence of the phase diagram on nonzero τ. By numerically calculating the MIPR, we find that the localization properties of

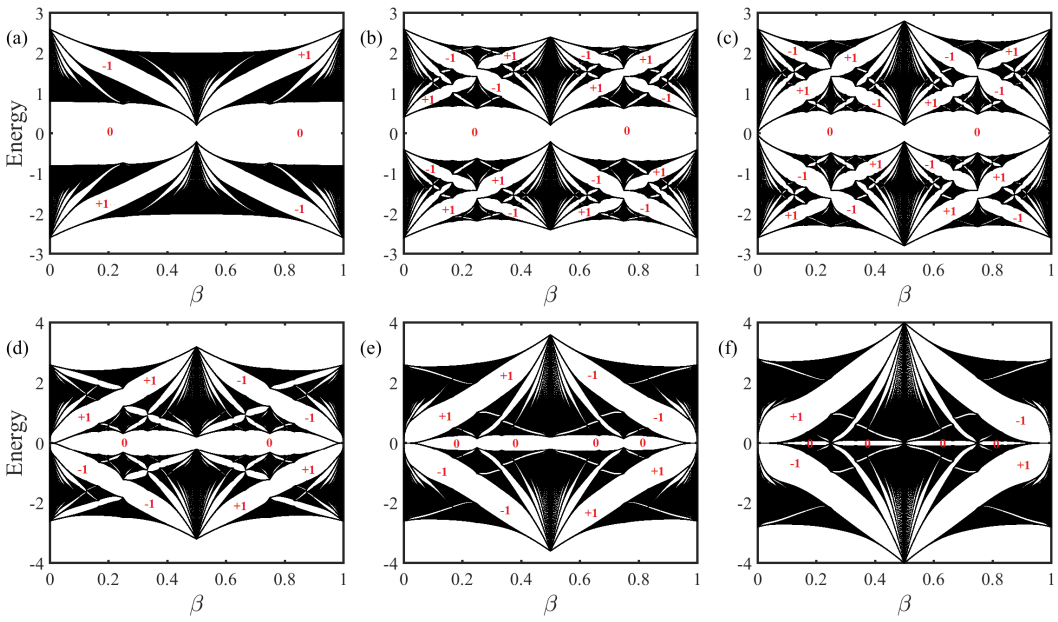

Figure 6.8: Hofstadter butterfly: energy spectrum as a function of magnetic flux per plaquette β in Aubry-André lattice with $V = 0$, $\tau = 0.3$, $\Delta = 0.4$, and (a) $\delta = 1$, (b) $\delta = 0.2$, (c) $\delta = 0.4$, (d) $\delta = 0.6$, (e) $\delta = 0.8$, (f) $\delta = 1$.

the off-diagonal of this model are profoundly affected by turning on the hopping modulation of τ. For a fixed $\tau = 1$, the results are summarized in the phase diagram shown in Fig. 6.5. There are four distinct phases, localized phase (I), critical localized phase (II), critical extended phase (III), and extended phase (IV), separated by solid black lines. In order to assert whether these regimes have different phases, we present a finite-size scaling analysis. Fig. 6.6 presents the MIPR of the model as a function of Δ with τ term at different system size. We have checked that with increasing L, the system is in the localized region (I) for $\delta - \tau + 1 < \Delta < \tau - \delta + 1$. Also, for the extended phase (III) the MIPR is finite and depend on the system size (L). In this phase, the MIPR satisfies the finite size scaling (FSS) form, MIPR $= bL^{-\eta}$, where b and η are parameters of fitting. At the $\Delta/t = 3.5$, the best fit is obtained with the exponent $\eta = 0.63$. Also, for this phase, with the increase of the L, MIPR tends to zero. The MIPR among localized, critical localized, critical extended, and extended phases satisfies

$$\text{MIPR}_E < \text{MIPR}_{CE} < \text{MIPR}_{CL} < \text{MIPR}_L \tag{6.20}$$

To verify this expression, we also checked FSS in the whole phase diagram (results

not shown).

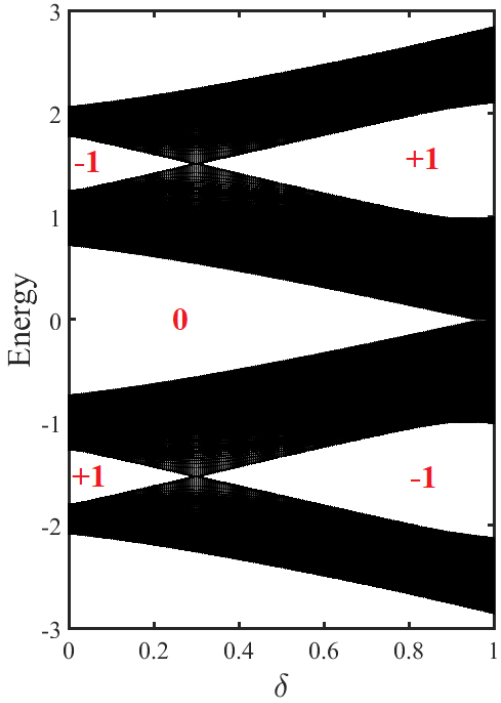

Figure 6.9: The evolution of the energy bands for $\beta = 0.25$, $V = 0$, $\tau = 0.3$, and $\Delta = 0.4$ as function of δ shown in Fig. (6.8). Gaps are labeled with their Chern numbers.

6.3.2 Generic GAAH model with p-wave pairing

We also investigate the generic p-wave pairing GAAH model with modulated on-site potentials, modulated off-diagonal hopping terms and modulated p-wave pairing terms. In this section, we explore the influence of modulated on-site potential on the phase transition of this system. It is clear that varying V changes the phase diagram. So due to the modulation in the p-wave pairing term, we find that the system is easier to be extended based on Δ/t when tuning the disordered on-site potential, V. In Fig. 6.7, the phase diagram of the generic GAAH model for the case $V/t = 1$ is shown. The phase boundary separating the localized phase, critical localized phase, critical extended phases, and extended phases vary rapidly with the SCs pairing. We also performed a similar analysis

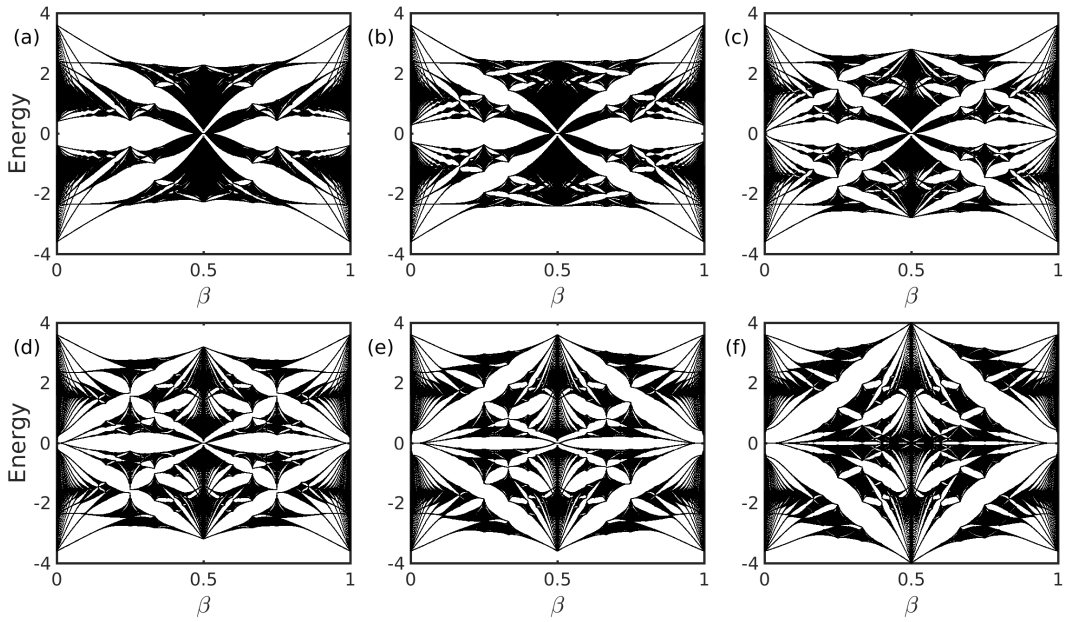

Figure 6.10: Hofstadter butterfly: energy spectrum as a function of magnetic flux per plaquette β in Aubry-André lattice with $V = 1$, $\tau = 0.3$, $\Delta = 0.4$, and (a) $\delta = 1$, (b) $\delta = 0.2$, (c) $\delta = 0.4$, (d) $\delta = 0.6$, (e) $\delta = 0.8$, (f) $\delta = 1$.

of the FSS for this phase diagram (results not shown). When $V/t = 1$, it is clear that for $\delta/t < 1$, the localized phase disappears and the critical localized phase increases sharply. So due to the modulation in the SC pairing, we find that the incommensurate generic GAAH model with p-wave pairing is easier delocalizes when tuning the disordered on-site potential for the case of $\delta < V$. We find that the topological properties of the generic GAAH model with p-wave pairing are profoundly affected by turning on the modulated on-site potential and modulated p-wave SC pairing.

6.4 Commensurate modulation

When β is rational, the lattice is commensurate. It is well known that in the commensurate case [17], the system will not undergo a localization-delocalization transition as that in the incommensurate case. When $\beta = 1/2$, both Kitaev-like and Su-Schrieffer-Heeger-like (SSH-like) models are included in this GAAH model

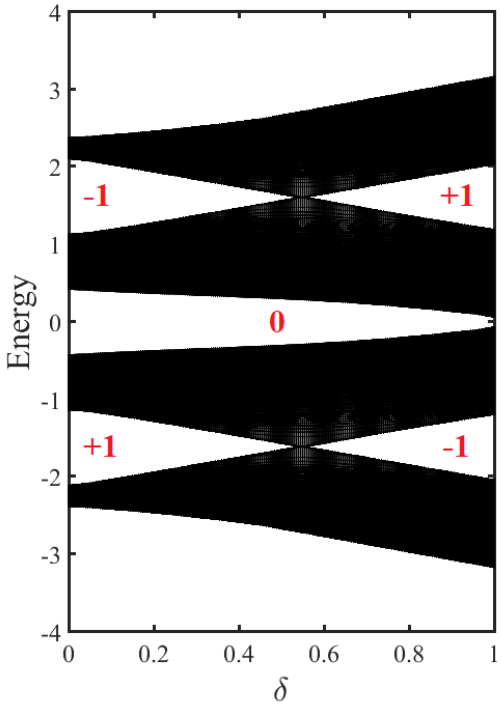

Figure 6.11: The evolution of the energy bands for $\beta = 0.25$, $V = 1$, $\tau = 0.3$, and $\Delta = 0.4$ as function of δ shown in Fig. (6.10). Gaps are labeled with their Chern numbers.

with p-wave SC pairing for commensurate modulations. The Hamiltonian of Eq. (6.1) is reduced to the SSH model for $V = \Delta = \delta = 0$ and to the Kitaev model for $\tau = \delta = 0$. In order to determine the different phase boundaries and characterize the topological phases, we need to calculate the effect of modulated SC pairing on topological properties of the system. In the following, we characterize the topological nature of the modulated SC pairing by calculating the Chern numbers for the major gaps of the spectrum.

6.4.1 Chern numbers

Chern numbers can be calculated from the density with respect to the changes in the magnetic field by using the Středa formula [115, 117, 137]. In lattice systems,

the Chern number can be written as

$$C = \frac{\partial \bar{n}(\beta)}{\partial \beta} \tag{6.21}$$

where $\bar{n}$ is the number of levels below the Fermi level and this formula is valid when the chemical potential lies in a gap [115]. Formally, the evaluation of the Chern numbers can be calculated by k-space integration of Berry curvature over the Brillouin zone. In figure 6.8 we present the Hofstadter butterfly for the case $V/t = 0$, $\lambda = 0.3$, $\Delta = 0.4$ and various values of δ. The spectrum for $\delta = 0$ is clearly formed by two triangular-lattice Hofstadter butterflies separated by a large gap. The Hofstadter butterfly separation is controlled by the SC parameter, δ (see Fig. 6.8). As illustrated in this figure, by changing the δ, the upper (lower) butterfly gets closer to the square regime and then the honeycomb regime with different topology (i.e., at the $\beta = 0.2$ for upper lattice the Chern number changes from -1 to 1). Also, we see that as δ is increased, the gaps at zero-energy are sufficiently small and have not completely closed so that the overall the butterfly shape is almost the same. It is possible to understand this surprising observation by the evolution of the energy bands at the points which major gap close and reopen. For $V/t = 0$, $\lambda = 0.3$, $\Delta = 0.4$, and $\beta = 0.25$, these evolutions are demonstrated in figure 6.9. When the energy gap close and reopen through this evolution, Chern numbers will change. For this case, we find two different regions which are sampled by different Chern numbers, ± 1. An important observation is that the Chern number is sensitively dependent on the δ parameter. As can be seen in Fig. 6.9, the whole area is covered by the triangular lattice, while the square lattice is confined to the point that gap closing, $\delta = 0.3$.

For the second case we consider $V \neq 0$, when the system has the sublattice asymmetry. In this case, we can see that when $V \neq 0$, the evolution of the energy spectrum between the triangular lattice and the square lattice remain unchanged (see Fig. 6.10). More interestingly, in this case, parts of the energy modes in the topologically nontrivial regime split into two energy modes which can be taken as two 1D Majorana chains coupled by on-site potential strength. As an example in Fig. 6.11, we display the evolution of bands from the triangular to the square and then triangular with different topology. As is shown in this figure, when V becomes nonzero and gets stronger, the critical value of the phase transition δ_c is

increased.

Chapter 7

Conclusion

Topological insulators and topological superconductors have drawn much recent interest for their potential applications in electronic devices and quantum computing. In order to incorporate these materials in technology, it is essential to have tools to manipulate their topological properties. In order to answer these questions one needs to characterize the topology. The Berry phase is usually used for this task. In this thesis it was shown that there exists a cumulant expansion associated with the Berry phase. The starting point was the Bargmann invariant, which gives rise to the discrete Berry phase. It was shown how a cumulant expansion associated with the Berry phase can be obtained from the Bargmann invariant. It was demonstrated that the cumulants are gauge invariant. It was also shown that the cumulants derived can also be related to corresponding expectation values of a particular operator. Since, in the modern theory of polarization, an expression for the second cumulant (spread or variance) is already in use, as a consistency check, equivalence between that and the spread resulting from the cumulant expansion presented here was shown. We also have shown that for localized Wannier functions they correspond to the cumulants of the Wannier centers. They are also related to the dielectric response functions of a given system. We calculated the cumulants for two models, RM and spinless SSH models. For RM model, we have also reconstructed the full probability distribution of the polarization based on the gauge-invariant cumulants and have studied how they

evolve as functions of different parameters of the Hamiltonian. In particular we calculated the evolution of the distribution around the topologically nontrivial point of the model. For spinless SSH model, we have developed a variational theory based on the Baeriswyl wave function for the SSH model with interaction, calculated the phase diagram of the model, and have studied the behavior of the polarization distribution as a function of the interaction. In our approximate scheme the transition is first order. Overall, the phase diagram is similar to the one found for another interacting topological model, the Kane–Mele–Hubbard model [46, 54]. We anticipate that detailed experimental measurements could also provide a probability distribution of the polarization for comparison with our predictions.

Secondly, we study the analogs of Haldane and Kane-Mele models in one-dimension. For Haldane-like model, it falls in the C or CI symmetry classes and exhibits topological behavior, as a result of two types of reflection symmetries present. The models can be shown to consist of two submodels. In this respect, the situation is similar to the Haldane squared model (the Kane–Mele model without the Rashba coupling) which exhibits a spin-resolved quantum spin-Hall effect. The two submodels on their own exhibit nonzero winding numbers, which are of opposite sign in the topologically nontrivial phase. For Kane-Mele-like model,we have assembled a one-dimensional ladder analog of the Kane-Mele model, step by step, first by shifting the Creutz model in the Brillouin zone, then by introducing spin and spin-orbit coupling. Our model falls in the CII symmetry class. We also derived a formula for the quantum spin Hall response and made an approximate implementation. For small values of the Rashba coupling, where our approximation is expected to be valid, we find a quantized spin Hall response in the topological phase indicating that QSH currents flowing along the legs of the ladder are a unique feature exhibited by our model.

Thirdly, We have studied the interface of several simple conductor-insulator interface systems. Across such an interface the Drude weight, and its associated topological invariant, changes abruptly. According to bulk-boundary correspondence, when this happens, topological edge states arise and unusual transport properties are expected. Our calculations show an enhanced Drude weight at

the interface of such systems, at the edge of the conducting system. The enhancement is weak if the insulating system is only weakly insulating, and grows monotonically with the strength of the insulation.

Finally, we studied the a GAAH model with the effect of introducing modulated p-wave SC-pairing in the commensurate and incommensurate case. Using the fact that dimensional extension of Aubry-André model model exactly to 2D Harper-Hofstater model reveals their topological character [10, 14], we extend the 1D GAAH model with p-wave SC to topologically equivalent and nontrivial an "ancestor" 2D p-wave SC model. This link implies that the GAAH model with p-wave superconductivity must have topologically protected modes similar to the 2D quantum Hall system with next nearest-neighbor p-wave SC-pairing on a lattice. In the incommensurate lattice when β is irrational, we find that transition from the delocalized state to localized state as a function of the modulated SC strength close to half-filling. Also, we have calculated the phase diagram of the model as a function of SC modulation amplitudes and other parameters for half filling by using the MIPR. On the other hand, for pure commensurate case (β is rational), due to the modulated SC amplitude, the resulting Hofstadter butterfly plots show a transition from the rectangular to square lattice, depending on a continuous variation of the parameter δ. We characterize that the Hofstadter butterfly spectrum of the GAAH model with p-wave SC pairing can be also determined from the commensurate off-diagonal GAAH model. The Hofstadter butterfly representation not only helps to visualize the square-rectangular lattice transition but also sheds light on the question why in a one-dimensional model such a transition is possible.

Bibliography

[1] J. E. Moore and L. Balents, "Topological invariants of time-reversal-invariant band structures," *Physical Review B*, vol. 75, no. 12, p. 121306, 2007.

[2] J. Wang, X.-J. Liu, G. Xianlong, and H. Hu, "Phase diagram of a non-abelian aubry-andré-harper model with p-wave superfluidity," *Physical Review B*, vol. 93, no. 10, p. 104504, 2016.

[3] C. Nayak, S. H. Simon, A. Stern, M. Freedman, and S. D. Sarma, "Non-abelian anyons and topological quantum computation," *Reviews of Modern Physics*, vol. 80, no. 3, p. 1083, 2008.

[4] S. R. Elliott and M. Franz, "Colloquium: Majorana fermions in nuclear, particle, and solid-state physics," *Reviews of Modern Physics*, vol. 87, no. 1, p. 137, 2015.

[5] K. v. Klitzing, G. Dorda, and M. Pepper, "New method for high-accuracy determination of the fine-structure constant based on quantized hall resistance," *Physical Review Letters*, vol. 45, no. 6, p. 494, 1980.

[6] D. C. Tsui, H. L. Stormer, and A. C. Gossard, "Two-dimensional magnetotransport in the extreme quantum limit," *Physical Review Letters*, vol. 48, no. 22, p. 1559, 1982.

[7] R. B. Laughlin, "Anomalous quantum hall effect: an incompressible quantum fluid with fractionally charged excitations," *Physical Review Letters*, vol. 50, no. 18, p. 1395, 1983.

[8] D. J. Thouless, M. Kohmoto, M. P. Nightingale, and M. den Nijs, "Quantized hall conductance in a two-dimensional periodic potential," *Physical Review Letters*, vol. 49, no. 6, p. 405, 1982.

[9] S. Aubry and G. André, "Analyticity breaking and anderson localization in incommensurate lattices," *Ann. Israel Phys. Soc*, vol. 3, no. 133, p. 18, 1980.

[10] Y. E. Kraus, Y. Lahini, Z. Ringel, M. Verbin, and O. Zilberberg, "Topological states and adiabatic pumping in quasicrystals," *Physical review letters*, vol. 109, no. 10, p. 106402, 2012.

[11] L.-J. Lang, X. Cai, and S. Chen, "Edge states and topological phases in one-dimensional optical superlattices," *Physical review letters*, vol. 108, no. 22, p. 220401, 2012.

[12] Y. Lahini, R. Pugatch, F. Pozzi, M. Sorel, R. Morandotti, N. Davidson, and Y. Silberberg, "Observation of a localization transition in quasiperiodic photonic lattices," *Physical review letters*, vol. 103, no. 1, p. 013901, 2009.

[13] P. Harper *et al.*, "Pg harper, proc. phys. soc., london, sect. a 68, 874 (1955).," in *Proc. Phys. Soc., London, Sect. A*, vol. 68, p. 874, 1955.

[14] D. R. Hofstadter, "Energy levels and wave functions of bloch electrons in rational and irrational magnetic fields," *Physical review B*, vol. 14, no. 6, p. 2239, 1976.

[15] Y. E. Kraus and O. Zilberberg, "Topological equivalence between the fibonacci quasicrystal and the harper model," *Physical review letters*, vol. 109, no. 11, p. 116404, 2012.

[16] H.-Q. Wang, M. Chen, R. W. Bomantara, J. Gong, and D. Xing, "Line nodes and surface majorana flat bands in static and kicked p-wave superconducting harper model," *Physical Review B*, vol. 95, no. 7, p. 075136, 2017.

[17] Q.-B. Zeng, S. Chen, and R. Lü, "Generalized aubry-andré-harper model with p-wave superconducting pairing," *Physical Review B*, vol. 94, no. 12, p. 125408, 2016.

[18] W. Su, J. Schrieffer, and A. J. Heeger, "Solitons in polyacetylene," *Physical Review Letters*, vol. 42, no. 25, p. 1698, 1979.

[19] R. Wakatsuki, M. Ezawa, Y. Tanaka, and N. Nagaosa, "Fermion fractionalization to majorana fermions in a dimerized kitaev superconductor," *Physical Review B*, vol. 90, no. 1, p. 014505, 2014.

[20] A. Y. Kitaev, "Unpaired majorana fermions in quantum wires," *Physics-Uspekhi*, vol. 44, no. 10S, p. 131, 2001.

[21] R. M. Lutchyn, J. D. Sau, and S. D. Sarma, "Majorana fermions and a topological phase transition in semiconductor-superconductor heterostructures," *Physical review letters*, vol. 105, no. 7, p. 077001, 2010.

[22] J. D. Sau, R. M. Lutchyn, S. Tewari, and S. D. Sarma, "Generic new platform for topological quantum computation using semiconductor heterostructures," *Physical review letters*, vol. 104, no. 4, p. 040502, 2010.

[23] J. Alicea, "Majorana fermions in a tunable semiconductor device," *Physical Review B*, vol. 81, no. 12, p. 125318, 2010.

[24] W. Chang, S. Albrecht, T. Jespersen, F. Kuemmeth, P. Krogstrup, J. Nygård, and C. M. Marcus, "Hard gap in epitaxial semiconductor–superconductor nanowires," *Nature nanotechnology*, vol. 10, no. 3, p. 232, 2015.

[25] F. D. M. Haldane, "Model for a quantum hall effect without landau levels: Condensed-matter realization of the" parity anomaly"," *Physical Review Letters*, vol. 61, no. 18, p. 2015, 1988.

[26] S. Murakami, N. Nagaosa, and S.-C. Zhang, "Spin-hall insulator," *Physical review letters*, vol. 93, no. 15, p. 156804, 2004.

[27] C. L. Kane and E. J. Mele, "Quantum spin hall effect in graphene," *Physical review letters*, vol. 95, no. 22, p. 226801, 2005.

[28] C. L. Kane and E. J. Mele, "Z 2 topological order and the quantum spin hall effect," *Physical review letters*, vol. 95, no. 14, p. 146802, 2005.

[29] B. A. Bernevig and S.-C. Zhang, "Quantum spin hall effect," *Physical review letters*, vol. 96, no. 10, p. 106802, 2006.

[30] M. König, S. Wiedmann, C. Brüne, A. Roth, H. Buhmann, L. W. Molenkamp, X.-L. Qi, and S.-C. Zhang, "Quantum spin hall insulator state in hgte quantum wells," *Science*, vol. 318, no. 5851, pp. 766–770, 2007.

[31] B. I. Halperin, "Quantized hall conductance, current-carrying edge states, and the existence of extended states in a two-dimensional disordered potential," *Physical Review B*, vol. 25, no. 4, p. 2185, 1982.

[32] B. Hetényi and M. Yahyavi, "Topological insulation in a ladder model with particle-hole and reflection symmetries," *Journal of Physics: Condensed Matter*, vol. 30, no. 10, p. 10LT01, 2018.

[33] S. Gholizadeh, M. Yahyavi, and B. Hetényi, "Extended creutz ladder with spin-orbit coupling: A one-dimensional analog of the kane-mele model," *EPL (Europhysics Letters)*, vol. 122, no. 2, p. 27001, 2018.

[34] J. Zak, "Berry's phase for energy bands in solids," *Physical review letters*, vol. 62, no. 23, p. 2747, 1989.

[35] R. King-Smith and D. Vanderbilt, "Theory of polarization of crystalline solids," *Physical Review B*, vol. 47, no. 3, p. 1651, 1993.

[36] R. Resta, "Macroscopic polarization in crystalline dielectrics: the geometric phase approach," *Reviews of modern physics*, vol. 66, no. 3, p. 899, 1994.

[37] R. Resta, "Quantum-mechanical position operator in extended systems," *Physical Review Letters*, vol. 80, no. 9, p. 1800, 1998.

[38] L. Fu and C. L. Kane, "Time reversal polarization and a z 2 adiabatic spin pump," *Physical Review B*, vol. 74, no. 19, p. 195312, 2006.

[39] B. Hetényi and M. Yahyavi, "Cumulants associated with geometric phases," *EPL (Europhysics Letters)*, vol. 105, no. 4, p. 40005, 2014.

[40] M. Yahyavi and B. Hetényi, "Reconstruction of the polarization distribution of the rice-mele model," *Physical Review A*, vol. 95, no. 6, p. 062104, 2017.

[41] B. Hetényi and M. Yahyavi, "http://yoksis.bilkent.edu.tr/pdf/files/7341.pdf," 2014.

[42] S. Patankar, L. Wu, B. Lu, M. Rai, J. D. Tran, T. Morimoto, D. E. Parker, A. G. Grushin, N. L. Nair, J. G. Analytis, J. E. Moore, J. Orenstein, and D. H. Torchinsky, "Resonance-enhanced optical nonlinearity in the weyl semimetal taas," *Phys. Rev. B*, vol. 98, p. 165113, Oct 2018.

[43] R. Kobayashi, Y. O. Nakagawa, Y. Fukusumi, and M. Oshikawa, "Scaling of the polarization amplitude in quantum many-body systems in one dimension," *Physical Review B*, vol. 97, no. 16, p. 165133, 2018.

[44] R. Resta and S. Sorella, "Electron localization in the insulating state," *Physical Review Letters*, vol. 82, no. 2, p. 370, 1999.

[45] A. Aligia and G. Ortiz, "Quantum mechanical position operator and localization in extended systems," *Physical review letters*, vol. 82, no. 12, p. 2560, 1999.

[46] S. Rachel, "Interacting topological insulators: a review," *Rep. Prog. Phys.*, vol. 81, p. 116501, 2018.

[47] V. Gurarie, "Single-particle green's functions and interacting topological insulators," *Physical Review B*, vol. 83, no. 8, p. 085426, 2011.

[48] Z. Wang, X.-L. Qi, and S.-C. Zhang, "Topological order parameters for interacting topological insulators," *Physical review letters*, vol. 105, no. 25, p. 256803, 2010.

[49] J. C. Budich, B. Trauzettel, and G. Sangiovanni, "Fluctuation-driven topological hund insulators," *Physical Review B*, vol. 87, no. 23, p. 235104, 2013.

[50] A. Altland and M. R. Zirnbauer, "Nonstandard symmetry classes in mesoscopic normal-superconducting hybrid structures," *Physical Review B*, vol. 55, no. 2, p. 1142, 1997.

[51] A. P. Schnyder, S. Ryu, A. Furusaki, and A. W. Ludwig, "Classification of topological insulators and superconductors in three spatial dimensions," *Physical Review B*, vol. 78, no. 19, p. 195125, 2008.

[52] C. N. Varney, K. Sun, M. Rigol, and V. Galitski, "Interaction effects and quantum phase transitions in topological insulators," *Physical Review B*, vol. 82, no. 11, p. 115125, 2010.

[53] G. Jotzu, M. Messer, R. Desbuquois, M. Lebrat, T. Uehlinger, D. Greif, and T. Esslinger, "Experimental realization of the topological haldane model with ultracold fermions," *Nature*, vol. 515, no. 7526, p. 237, 2014.

[54] S. Rachel and K. Le Hur, "Topological insulators and mott physics from the hubbard interaction," *Physical Review B*, vol. 82, no. 7, p. 075106, 2010.

[55] C. Griset and C. Xu, "Phase diagram of the kane-mele-hubbard model," *Physical Review B*, vol. 85, no. 4, p. 045123, 2012.

[56] I. J. Hamad, C. J. Gazza, and J. A. Riera, "Helical currents in metallic rashba strips," *Physical Review B*, vol. 93, no. 20, p. 205113, 2016.

[57] M. Hohenadler and F. F. Assaad, "Correlation effects in two-dimensional topological insulators," *Journal of Physics: Condensed Matter*, vol. 25, no. 14, p. 143201, 2013.

[58] M. Laubach, J. Reuther, R. Thomale, and S. Rachel, "Rashba spin-orbit coupling in the kane-mele-hubbard model," *Physical Review B*, vol. 90, no. 16, p. 165136, 2014.

[59] M. C. Gutzwiller, "Effect of correlation on the ferromagnetism of transition metals," *Physical Review Letters*, vol. 10, no. 5, p. 159, 1963.

[60] A. R. Bishop, D. K. Campbell, S. E. Trullinger, and P. Kumar, *Nonlinearity in Condensed Matter: Proceedings of the Sixth Annual Conference, Center for Nonlinear Studies, Los Alamos, New Mexico, 5–9 May, 1986*, vol. 69. Springer Science & Business Media, 2012.

[61] D. Baeriswyl, "Variational scheme for the mott transition," *Foundations of Physics*, vol. 30, no. 12, pp. 2033–2048, 2000.

[62] L. Reatto and G. Masserini, "Shadow wave function for many-boson systems," *Physical Review B*, vol. 38, no. 7, p. 4516, 1988.

[63] M. Schiró and M. Fabrizio, "Quantum quenches in the hubbard model: Time-dependent mean-field theory and the role of quantum fluctuations," *Physical Review B*, vol. 83, no. 16, p. 165105, 2011.

[64] M. Schiró and M. Fabrizio, "Time-dependent mean field theory for quench dynamics in correlated electron systems," *Physical review letters*, vol. 105, no. 7, p. 076401, 2010.

[65] B. Hetényi, B. Tanatar, and L. Martelo, "Variational monte carlo method for the baeriswyl wave function: Application to the one-dimensional bosonic hubbard model," *Physical Review B*, vol. 93, no. 17, p. 174518, 2016.

[66] B. Dóra, M. Haque, F. Pollmann, and B. Hetényi, "Quantum quench in two dimensions using the variational baeriswyl wave function," *Physical Review B*, vol. 93, no. 11, p. 115124, 2016.

[67] A. Altland and M. R. Zirnbauer, "Nonstandard symmetry classes in mesoscopic normal-superconducting hybrid structures," *Physical Review B*, vol. 55, no. 2, p. 1142, 1997.

[68] A. P. Schnyder, S. Ryu, A. Furusaki, and A. W. Ludwig, "Classification of topological insulators and superconductors in three spatial dimensions," *Physical Review B*, vol. 78, no. 19, p. 195125, 2008.

[69] C.-K. Chiu, H. Yao, and S. Ryu, "Classification of topological insulators and superconductors in the presence of reflection symmetry," *Physical Review B*, vol. 88, no. 7, p. 075142, 2013.

[70] C.-K. Chiu, J. C. Teo, A. P. Schnyder, and S. Ryu, "Classification of topological quantum matter with symmetries," *Reviews of Modern Physics*, vol. 88, no. 3, p. 035005, 2016.

[71] M. Creutz and I. Horvath, "Surface states and chiral symmetry on the lattice," *Physical Review D*, vol. 50, no. 3, p. 2297, 1994.

[72] M. Creutz, "End states, ladder compounds, and domain-wall fermions," *Physical review letters*, vol. 83, no. 13, p. 2636, 1999.

[73] S. Pancharatnam, "Generalized theory of interference, and its applications," in *Proc. Indian Acad. Sci. A*, vol. 44, p. 247, 1956.

[74] I. D. Nagtegaal and J. H. J. M. van Krieken, "The role of pathologists in the quality control of diagnosis and treatment of rectal canceran overview," *European Journal of Cancer*, vol. 38, no. 7, pp. 964 – 972, 2002.

[75] H. Kuratsuji and S. Iida, "Effective action for adiabatic process: Dynamical meaning of berry and simon's phase," *Progress of theoretical physics*, vol. 74, no. 3, pp. 439–445, 1985.

[76] H. Kuratsuji and S. Iida, "Dynamical meaning of quantum adiabatic phase: the case of a noncanonical system," *Physical review letters*, vol. 56, no. 10, p. 1003, 1986.

[77] M. V. Berry, "Quantal phase factors accompanying adiabatic changes," *Proc. R. Soc. Lond. A*, vol. 392, no. 1802, pp. 45–57, 1984.

[78] B. Hetényi, "Many-body position operator in lattice fermionic systems with periodic boundary conditions," *Journal of Physics A: Mathematical and Theoretical*, vol. 42, no. 41, p. 412003, 2009.

[79] F. H. Essler, H. Frahm, F. Göhmann, A. Klümper, and V. E. Korepin, *The one-dimensional Hubbard model*. Cambridge University Press, 2005.

[80] D. Vanderbilt and R. Resta, "Quantum electrostatics of insulators: polarization, wannier functions, and electric fields," *Contemporary Concepts of Condensed Matter Science*, vol. 2, pp. 139–163, 2006.

[81] N. Marzari and D. Vanderbilt, "Maximally localized generalized wannier functions for composite energy bands," *Physical review B*, vol. 56, no. 20, p. 12847, 1997.

[82] B. Hetényi, "Current response in extended systems as a geometric phase: Application to variational wavefunctions," *Journal of the Physical Society of Japan*, vol. 81, no. 12, p. 124711, 2012.

[83] I. Souza, T. Wilkens, and R. M. Martin, "Polarization and localization in insulators: Generating function approach," *Physical Review B*, vol. 62, no. 3, p. 1666, 2000.

[84] E. Kudinov, "Difference between insulating and conducting states," *arXiv preprint cond-mat/9902361*, 1999.

[85] P. Delplace, D. Ullmo, and G. Montambaux, "Zak phase and the existence of edge states in graphene," *Physical Review B*, vol. 84, no. 19, p. 195452, 2011.

[86] M. Atala, M. Aidelsburger, J. T. Barreiro, D. Abanin, T. Kitagawa, E. Demler, and I. Bloch, "Direct measurement of the zak phase in topological bloch bands," *Nature Physics*, vol. 9, no. 12, p. 795, 2013.

[87] W. Kohn, "Theory of the insulating state," *Physical Review*, vol. 133, no. 1A, p. A171, 1964.

[88] W.-P. Su, J. Schrieffer, and A. Heeger, "Soliton excitations in polyacetylene," *Physical Review B*, vol. 22, no. 4, p. 2099, 1980.

[89] M. Rice and E. Mele, "Elementary excitations of a linearly conjugated diatomic polymer," *Physical Review Letters*, vol. 49, no. 19, p. 1455, 1982.

[90] D. Vanderbilt and R. King-Smith, "Electric polarization as a bulk quantity and its relation to surface charge," *Physical Review B*, vol. 48, no. 7, p. 4442, 1993.

[91] D. Xiao, M.-C. Chang, and Q. Niu, "Berry phase effects on electronic properties," *Reviews of modern physics*, vol. 82, no. 3, p. 1959, 2010.

[92] S. Nakajima, T. Tomita, S. Taie, T. Ichinose, H. Ozawa, L. Wang, M. Troyer, and Y. Takahashi, "Topological thouless pumping of ultracold fermions," *Nature Physics*, vol. 12, no. 4, p. 296, 2016.

[93] D. Thouless, "Quantization of particle transport," *Physical Review B*, vol. 27, no. 10, p. 6083, 1983.

[94] S. R. Manmana, A. M. Essin, R. M. Noack, and V. Gurarie, "Topological invariants and interacting one-dimensional fermionic systems," *Physical Review B*, vol. 86, no. 20, p. 205119, 2012.

[95] D. Baeriswyl, "Nonlinearity in condensed matter," 1986.

[96] K. Bandyopadhyay, A. K. Bhattacharya, P. Biswas, and D. Drabold, "Maximum entropy and the problem of moments: A stable algorithm," *Physical Review E*, vol. 71, no. 5, p. 057701, 2005.

[97] R. Collins and A. Wragg, "Maximum entropy histograms," *Journal of Physics A: Mathematical and General*, vol. 10, no. 9, p. 1441, 1977.

[98] L. R. Mead and N. Papanicolaou, "Maximum entropy in the problem of moments," *Journal of Mathematical Physics*, vol. 25, no. 8, pp. 2404–2417, 1984.

[99] S. Kirkpatrick, C. D. Gelatt, and M. P. Vecchi, "Optimization by simulated annealing," *science*, vol. 220, no. 4598, pp. 671–680, 1983.

[100] H. Takayama, Y. R. Lin-Liu, and K. Maki, "Continuum model for solitons in polyacetylene," *Physical Review B*, vol. 21, no. 6, p. 2388, 1980.

[101] R. Jackiw and C. Rebbi, "Solitons with fermion number 1/2," *Physical Review D*, vol. 13, no. 12, p. 3398, 1976.

[102] A. J. Heeger, S. Kivelson, J. Schrieffer, and W.-P. Su, "Solitons in conducting polymers," *Reviews of Modern Physics*, vol. 60, no. 3, p. 781, 1988.

[103] J. Ruostekoski, G. V. Dunne, and J. Javanainen, "Particle number fractionalization of an atomic fermi-dirac gas in an optical lattice," *Physical review letters*, vol. 88, no. 18, p. 180401, 2002.

[104] L. Li, Z. Xu, and S. Chen, "Topological phases of generalized su-schrieffer-heeger models," *Physical Review B*, vol. 89, no. 8, p. 085111, 2014.

[105] H. Bethe, "Zur theorie der metalle," *Zeitschrift für Physik*, vol. 71, no. 3-4, pp. 205–226, 1931.

[106] B. Valenzuela, S. Fratini, and D. Baeriswyl, "Charge and spin order in one-dimensional electron systems with long-range coulomb interactions," *Physical Review B*, vol. 68, no. 4, p. 045112, 2003.

[107] B. Hetényi, "Approximate solution of variational wave functions for strongly correlated systems: Description of bound excitons in metals and insulators," *Physical Review B*, vol. 82, no. 11, p. 115104, 2010.

[108] M. Yahyavi, L. Saleem, and B. Hetényi, "Variational study of the interacting, spinless su–schrieffer–heeger model," *Journal of Physics: Condensed Matter*, vol. 30, no. 44, p. 445602, 2018.

[109] J. K. Asbóth, L. Oroszlány, and A. Pályi, "A short course on topological insulators," *Lecture Notes in Physics*, vol. 919, 2016.

[110] D. Sticlet, L. Seabra, F. Pollmann, and J. Cayssol, "From fractionally charged solitons to majorana bound states in a one-dimensional interacting model," *Physical Review B*, vol. 89, no. 11, p. 115430, 2014.

[111] D. Sticlet, B. Dóra, and J. Cayssol, "Persistent currents in dirac fermion rings," *Physical Review B*, vol. 88, no. 20, p. 205401, 2013.

[112] S. Ryu, A. P. Schnyder, A. Furusaki, and A. W. Ludwig, "Topological insulators and superconductors: tenfold way and dimensional hierarchy," *New Journal of Physics*, vol. 12, no. 6, p. 065010, 2010.

[113] A. Lau, J. van den Brink, and C. Ortix, "Topological mirror insulators in one dimension," *Physical Review B*, vol. 94, no. 16, p. 165164, 2016.

[114] J. C. Teo, L. Fu, and C. Kane, "Surface states and topological invariants in three-dimensional topological insulators: Application to bi 1- x sb x," *Physical Review B*, vol. 78, no. 4, p. 045426, 2008.

[115] P. Streda, "Theory of quantised hall conductivity in two dimensions," *Journal of Physics C: Solid State Physics*, vol. 15, no. 22, p. L717, 1982.

[116] A. Widom, "Thermodynamic derivation of the hall effect current," *Physics Letters A*, vol. 90, no. 9, p. 474, 1982.

[117] F. Yılmaz, F. N. Ünal, and M. Oktel, "Evolution of the hofstadter butterfly in a tunable optical lattice," *Physical Review A*, vol. 91, no. 6, p. 063628, 2015.

[118] M.-F. Yang and M.-C. Chang, "Středa-like formula in the spin hall effect," *Physical Review B*, vol. 73, no. 7, p. 073304, 2006.

[119] A. Dyrdał, V. Dugaev, and J. Barnaś, "Spin-resolved orbital magnetization in rashba two-dimensional electron gas," *Physical Review B*, vol. 94, no. 20, p. 205302, 2016.

[120] B. Hetényi, "dc conductivity as a geometric phase," *Physical Review B*, vol. 87, no. 23, p. 235123, 2013.

[121] B. Hetényi, "Drude weight, meissner weight, rotational inertia of bosonic superfluids: How are they distinguished?," *Journal of the Physical Society of Japan*, vol. 83, no. 3, p. 034711, 2014.

[122] A. Sütő, "The total momentum of quantum fluids," *Journal of Mathematical Physics*, vol. 56, no. 8, p. 081901, 2015.

[123] G. Roati, C. D'Errico, L. Fallani, M. Fattori, C. Fort, M. Zaccanti, G. Modugno, M. Modugno, and M. Inguscio, "Anderson localization of a non-interacting bose–einstein condensate," *Nature*, vol. 453, no. 7197, p. 895, 2008.

[124] J. Chabé, G. Lemarié, B. Grémaud, D. Delande, P. Szriftgiser, and J. C. Garreau, "Experimental observation of the anderson metal-insulator transition with atomic matter waves," *Physical review letters*, vol. 101, no. 25, p. 255702, 2008.

[125] L. Dal Negro, C. J. Oton, Z. Gaburro, L. Pavesi, P. Johnson, A. Lagendijk, R. Righini, M. Colocci, and D. S. Wiersma, "Light transport through the band-edge states of fibonacci quasicrystals," *Physical review letters*, vol. 90, no. 5, p. 055501, 2003.

[126] J. C. C. Cestari, A. Foerster, and M. Gusmão, "Fate of topological states in incommensurate generalized aubry-andré models," *Physical Review B*, vol. 93, no. 20, p. 205441, 2016.

[127] F. Liu, S. Ghosh, and Y. Chong, "Localization and adiabatic pumping in a generalized aubry-andré-harper model," *Physical Review B*, vol. 91, no. 1, p. 014108, 2015.

[128] T. Liu, P. Wang, S. Chen, and G. Xianlong, "Phase diagram of a generalized off-diagonal aubry–andré model with p-wave pairing," *Journal of Physics B: Atomic, Molecular and Optical Physics*, vol. 51, no. 2, p. 025301, 2017.

[129] S. Ganeshan and K. Sun, "S. ganeshan, k. sun, and s. das sarma, phys. rev. lett. 110, 180403 (2013).," *Phys. Rev. Lett.*, vol. 110, p. 180403, 2013.

[130] X. Cai, L.-J. Lang, S. Chen, and Y. Wang, "Topological superconductor to anderson localization transition in one-dimensional incommensurate lattices," *Physical review letters*, vol. 110, no. 17, p. 176403, 2013.

[131] H. Hiramoto and M. Kohmoto, "Scaling analysis of quasiperiodic systems: generalized harper model," *Physical Review B*, vol. 40, no. 12, p. 8225, 1989.

[132] J. Han, D. Thouless, H. Hiramoto, and M. Kohmoto, "Critical and bicritical properties of harper's equation with next-nearest-neighbor coupling," *Physical Review B*, vol. 50, no. 16, p. 11365, 1994.

[133] E. Lieb, T. Schultz, and D. Mattis, "Two soluble models of an antiferromagnetic chain," *Annals of Physics*, vol. 16, no. 3, pp. 407–466, 1961.

[134] P. De Gennes, "Superconducting of metals and alloys," 1966.

[135] D. Thouless, "A relation between the density of states and range of localization for one dimensional random systems," *Journal of Physics C: Solid State Physics*, vol. 5, no. 1, p. 77, 1972.

[136] M. Kohmoto, "Metal-insulator transition and scaling for incommensurate systems," *Physical review letters*, vol. 51, no. 13, p. 1198, 1983.

[137] R. Umucalılar, H. Zhai, and M. Oktel, "Trapped fermi gases in rotating optical lattices: Realization and detection of the topological hofstadter insulator," *Physical review letters*, vol. 100, no. 7, p. 070402, 2008.

Appendix A

Numerical minimization of χ^2

In Table A.1 values of the negative base ten logarithm of χ^2 rounded down to the first digit (defined in Eq. (3.5)) is shown for the reconstructed probabilities in Figs. 3.6 and 3.10. In all cases χ^2 decreased at least eight orders of magnitude from its initial value during the simulated annealing calculation.

In Table A.2 the values of the parameters according to the parametrization used in Figs. 3.2-3.10 are shown. Also shown are values of the negative base ten logarithm of χ^2 rounded down to the first digit for probability distributions corresponding to the points in Figs. 3.11 and 3.12.

Fig. 3.6	Δ/J	$-\log_{10}(\chi^2)$	Δ/J	$-\log_{10}(\chi^2)$
$J'/J = 0$	-2	8	-1	7
$J'/J = 0$	-0.5	8	-0.4	6
$J'/J = 0$	-0.3	7	-0.2	6
$J'/J = 0$	-0.1	7	0	6
Fig. 3.7	Δ/J	$-\log_{10}(\chi^2)$	Δ/J	$-\log_{10}(\chi^2)$
$J'/J = 0.3$	-2	6	-1	5
$J'/J = 0.3$	-0.5	6	-0.4	4
$J'/J = 0.3$	-0.3	5	-0.2	4
$J'/J = 0.3$	-0.1	5	0	4
Fig. 3.8	Δ/J	$-\log_{10}(\chi^2)$	Δ/J	$-\log_{10}(\chi^2)$
$J'/J = 0.5$	-2	5	-1	4
$J'/J = 0.5$	-0.5	5	-0.4	4
$J'/J = 0.5$	-0.3	5	-0.2	4
$J'/J = 0.5$	-0.1	5	0	4
Fig. 3.9	Δ/J	$-\log_{10}(\chi^2)$	Δ/J	$-\log_{10}(\chi^2)$
$J'/J = 0.7$	-2	5	-1	4
$J'/J = 0.7$	-0.5	5	-0.4	4
$J'/J = 0.7$	-0.3	4	-0.2	4
$J'/J = 0.7$	-0.1	4	0	4
Fig. 3.10	Δ/J	$-\log_{10}(\chi^2)$	Δ/J	$-\log_{10}(\chi^2)$
$J'/J = 1.0$	-1	8	-0.6	7
$J'/J = 1.0$	-0.9	8	-0.5	7
$J'/J = 1.0$	-0.8	7	-0.4	7
$J'/J = 1.0$	-0.7	7		

Table A.1: $-\log_{10}\chi^2$ rounded to the first digit shown for the reconstructed probabilities in Figs. 3.6 and 3.10.

	Fig. 3.11			Fig. 3.12		
	Δ/J	J'/J	$-\log_{10}(\chi^2)$	Δ/J	J'/J	$-\log_{10}(\chi^2)$
A^*	-1.9875	0.9875	8	$-.3995$	.9975	6
B	-1.154	.333	7	$-.3149$	.8181	6
C	$-.5359$	.072	7	$-.1705$	.7047	6
D	0	0	6	0	.6666	6
E	.5359	.072	8	.1705	.7047	6
F	1.154	.333	7	.3149	.8181	6
G	2	1	7	.4	1	6
H	3.4641	3	6	.3849	1.2222	6
I	7.4641	13.928	8	.2419	1.4189	6
J	0	∞ (1/0)	7	0	1.5	6
K	-7.4641	13.928	7	$-.2419$	1.4189	6
L	-3.4641	3	6	$-.3849$	1.2222	6

Table A.2: Values of the parameters according to the parametrization used in Figs. 3.2-3.10 are shown. Also shown are values of $-\log_{10}\chi^2$ rounded to the first digit for probability distributions corresponding to the points in Figs. 3.11 and 3.12.

Appendix B

Publications in SCI journals

[1] M. Yahyavi, L. Saleem, and B. Hetényi, *Variational study of the interacting Su-Schrieffer-Heeger model*, J. Phys.: Condens. Matter **30**, 445602 (2018).

[2] S. Gholizadeh, M. Yahyavi, B. Hetényi, *Extended Creutz ladder with spin-orbit coupling: The one-dimensional analog of the Kane-Mele model*, EPL(Europhysics Letters) **122**, 27001 (2018).

[3] B. Hetényi, M. Yahyavi, *Topological insulation in a ladder model with particle-hole and reflection symmetries*, J. Phys.: Condens. Matter **30**, 10LT01 (2018).

[4] M. Yahyavi and B. Hetényi, *Reconstruction of the polarization distribution of the Rice-Mele model*, Phys. Rev. A **95**, 062104 (2017).

[5] B. Hetényi,, M. Yahyavi, *Cumulants associated with geometric phases*, EPL (Europhysics Letters) **105.4**, 40005 (2014).

[6] M. Yahyavi and B. Hetényi, *Topological phase transition in a generalized Aubry-André-Harper system with p-wave superconductivity*, "In Preparing".

[7] M. Yahyavi and B. Hetényi, *Enhanced charge transport at the ideal*

conductor-insulator interface, "In Preparing".